UNIVERSITY OF CALIFORNIA,
IRVINE

Concentrated Solar Integrated Solid Oxide Cell Systems and Cement Plants for Zero-Carbon Hydrogen and Low-Carbon Cement Production

THESIS

submitted in partial satisfaction of the requirements
for the degree of

MASTER OF SCIENCE

in Mechanical and Aerospace Engineering

by

Jun Yong Kim

Thesis Committee:
Professor Jacob Brouwer, Chair
Professor Vince McDonell
Professor Yoonjin Won

2021

DEDICATION

To my parents who have supported and believed in me throughout the years. This is only the end of the beginning.

TABLE OF CONTENTS

LIST OF FIGURES

LIST OF TABLES

ACKNOWLEDGEMENTS

I would like to express my deepest appreciation to my advisor, Professor Jacob Brouwer, who has guided me throughout this work with his expertise and leadership. Without his guidance and persistent help, this thesis would not have been possible. He has been a major role model and inspiration.

I would like to thank my committee members, Professor Vince McDonell and Professor Yoonjin Won.

I would also like to thank Dr. Saeedmanesh and Dr. Mastropasqua for their support and guidance in this work. They, too, have been my role models.

ABSTRACT OF THE THESIS

Concentrated Solar Integrated Solid Oxide Cell System and Cement Plant for Zero-Carbon Hydrogen and Low-Carbon Cement Production

by

Jun Yong Kim

Master of Science in Mechanical and Aerospace Engineering

University of California, Irvine, 2021

Professor Jacob Brouwer, Chair

Economic sectors such as transportation, electricity, industrial, commercial, residential, and agriculture depend on a reliable and consistent supply of energy. However, a vast majority of these sectors draw most of their energy from fossil fuels which emit pollutants and greenhouse gases (GHG) when combusted or processed. The emissions, as a result, are the largest contributing factors to recent climate change and environmental challenges. To reduce the emissions using sustainable and renewable energy sources (RES) in the power generating and cement manufacturing sectors, design and integration of a concentrated solar power (CSP) plant with a solid oxide electrolysis cell (SOEC) system for hydrogen production and with a coal-fired cement plant for producing cement are analyzed.

To analyze the dynamic behavior, such as temperature variations for thermal management, and system performance characteristics, a dynamic CSP-integrated SOEC system model is developed, aiming to achieve high hydrogen production efficiency and to

minimize the balance of plant power consumption. The results show that the electrical efficiency of the integrated hydrogen production system is greater than 90% throughout the majority of the operating time. Particularly, the electrical efficiency between 10 AM and 1 PM is nearly 100%. Such high efficiency is achieved as a result of the SOEC stack operating in endothermic conditions while taking thermal energy provided by the CSP plant.

A CSP-integrated cement plant is modeled to assess the percent solarization, reduction in carbon dioxide (CO_2) emissions, and costs of CO_2 avoided. Five locations have been selected across the United States providing a wide range of Direct Normal Irradiance (DNI) potentials. The results show that the plant located in Southern California (SoCal) has the best performance characteristics with the highest percent solarization and reduction of CO_2 emissions, utilizing solar thermal energy more than 70% of the operating time and reducing the CO_2 emissions by 15%. Economically, the western region of the United States, especially the states of California, Arizona, Nevada, and New Mexico, is found to be the best region for integrating a conventional cement plant with a CSP plant where the annual DNI exceeds 2000 kWh/m^2. The costs of CO_2 avoided in the region range from 70 to 100 USD per ton of CO_2 which makes such integration as competitive as integration with competing carbon capture technologies.

1. Background

1.1 The Role of Energy in the World and Its Environmental Impacts

Energy plays an essential role in economic sectors such as transportation, electricity, industrial, commercial, residential, and agriculture which depend on a reliable and consistent supply of energy. However, a vast majority of these sectors draw most of their energy from fossil fuels—a nonrenewable and unsustainable source that emits pollutants and greenhouse gases (GHG) when combusted—to generate the power needed [1]. The transportation and electricity production sectors together generate 57% of the total GHG emissions in the United States [2]. Much of the emissions come from power production and energy conversion which are the largest contributors to the environmental challenges that societies face today [3]. Due to the adverse effect of using fossil fuels as primary energy sources, significant efforts have been made to reduce GHG emissions. With greater scientific and public awareness of the adverse effect of fossil fuels, stricter regulations have already been imposed to enhance the efficiency of engines and power plants, subsequently reducing the emissions. However, without the complete elimination of fossil fuels in the sectors, GHG emissions will always instigate environmental challenges.

1.2 Efforts to Mitigate GHG Emissions

To accomplish zero GHG emissions in the near future, Jerry Brown, the former Governor of California signed Senate Bill 100, which mandates the state of California to meet its power demand with only renewable energy and zero-carbon sources by 2045 [4]. Several scientists and researchers have investigated California's power demand and supply

to model and simulate the power system behavior and its viability to reach the goal of decarbonization by 2045. The conclusion drawn from the investigations yields that implementation of energy storage is essential due to the intermittent nature of renewable energy sources (RES) such as solar and wind [5]–[7].

1.3 Challenges of Introducing Renewable Energy Sources

As of 2018, the state of California is meeting 34% of the power demand with RES [8]. As a result of utilizing RES for power generation, GHG emissions in California are significantly lower than the U.S. average emissions. In fact, the average CO_2 emission rate of the U.S. grid in 2015 was 5.16E-01 kg/kWh, whereas the rate of the CA grid was 2.95E-01 kg/kWh [9]. The primary cause of lower CO_2 emission rate in California is due to the high use of RES, such as solar and wind power systems. During a typical daytime period in summer, solar and wind account for 45% of the total power production, producing nearly 13,000 MW from the data provided by the California Independent System Operator (CAISO) [10]. Although both solar and wind sources remain at the forefront of the state's goal to meet the demand, power generation from either is intermittent due to their dependence on weather conditions and time of day. As shown for example in Figure 1, solar power is only generated during the day-time from 7 AM to 7 PM, with a short period of mostly steady power generation from 9 AM to 4 PM. Similarly, wind power generation experiences intermittency on certain wind-stagnant days, where wind power generation can be negligible.

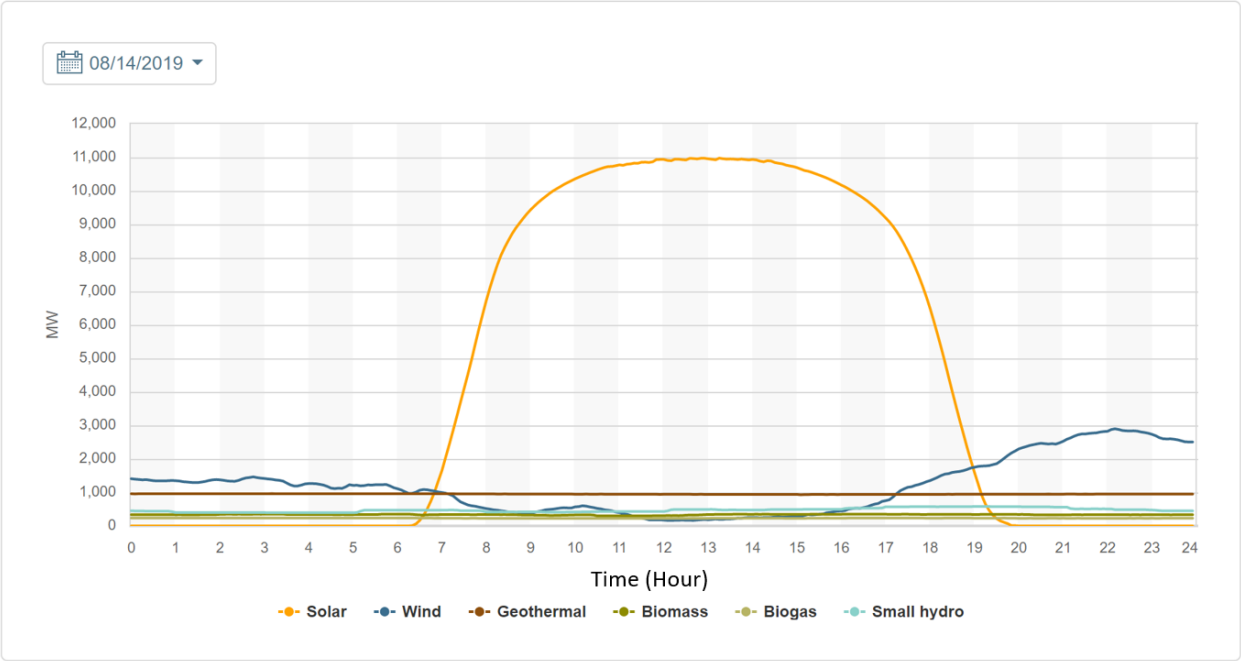

Figure 1: Renewable Energy Supply vs. Time on August 14, 2019

Source: Adapted from [10]

Another issue with generating power with RES is energy curtailments resulting from the oversupply of renewable power. Although RES capacity increases year after year to meet the goal of decarbonization, the demand on the customer-end does not increase and is not sufficiently shifted to match renewable supply dynamics, creating an oversupply or overgeneration of power at certain times. The oversupply results in a fluctuation of electricity cost, establishing challenges for integrating even more sun and wind power [11], [12]. To reduce this oversupply risk, CAISO has been curtailing the oversupply of renewable energy, which wastes the resource, but it is the most cost effective means of managing grid reliability. Figure 2 shows the “Duck Curve”, a plot showing the net demand over time on a typical day in Spring. As shown in Figure 3, as solar capacity increases yearly starting from 2013, the risk of overgeneration continues to increase which results in

increasing energy curtailment from RES. Figure *3* shows the amount of curtailed energy from 2014 to 2021 due to the oversupply. Specifically, in March 2021, 341,959 MWh of energy was curtailed, which resulted in the highest energy curtailment in California's history. The challenge with the curtailment, however, could be resolved by coupling RES with energy storage. As newer and better energy storage technologies are introduced, the intermittent nature of RES and overgeneration issues from wind and solar sources can be mitigated and managed [13].

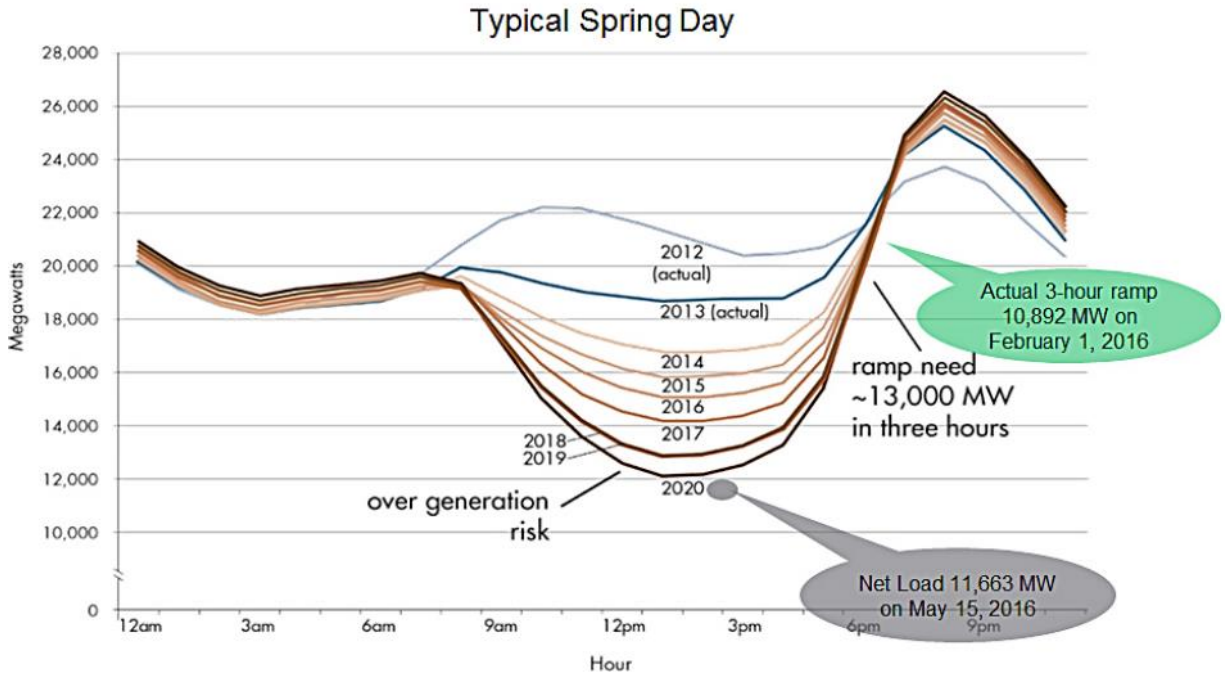

Figure 2: Net Demand Profile Showing Over-Generation Risk

Source: Adapted from [14]

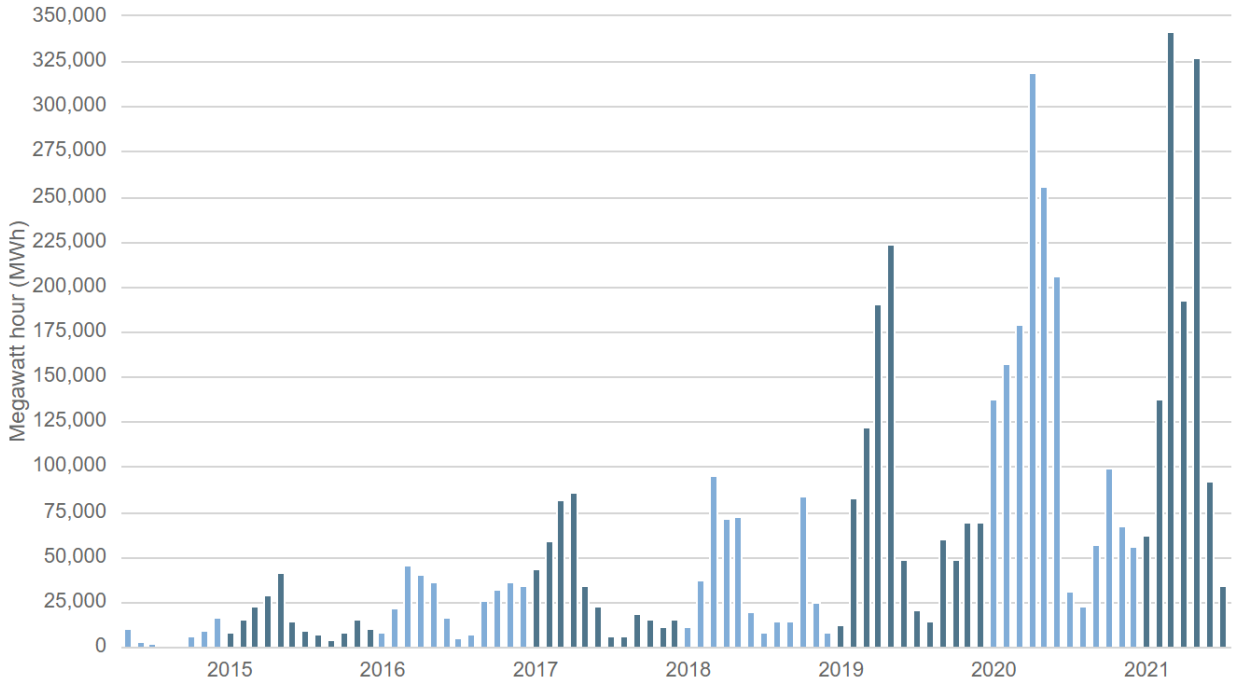

Figure 3: Renewable Energy Curtailments Totals by Month in CAISO

Source: Adapted from [15]

1.4 Solutions to the Challenges of Introducing Renewable Energy Sources

According to Colbertaldo et al. [5], in order to avoid energy curtailments and to complement the intermittent nature of RES, implementation of energy storage technologies, such as pumped hydroelectric, battery energy storage systems (BESS), compressed air, and compressed hydrogen storage technologies, is necessary. Pumped hydroelectric energy storage uses a large elevation gradient providing gravitational potential energy storage between upper and lower lakes. Pumped hydroelectric energy storage is the most mature technology among the other storage technologies, and is currently the most widely adopted, accounting for over 99% of grid-scale energy storage worldwide [16]. Compressed air energy storage does not require a large elevation gradient

due to its reliance on a pressure gradient to store energy. Often times, compressed air energy storage is coupled with gas turbines that also convert fuel to produce electricity. Compressed hydrogen energy storage works together with electrolyzers, which produce hydrogen by splitting water, and fuel cells to generate power using hydrogen. In addition, hydrogen can be deployed in the market as fuel to power fuel cell vehicles [13]. BESS store energy as chemical potential energy. With recent battery cost reduction and high round-trip efficiency of up to 87%, BESS is becoming the most popular grid-scale storage technology in energy industries around the world [5].

The Colbertaldo et al. study [5] modeled and simulated the power system in California based on data provided by CAISO, and identified 12 possible combinations with wind capacity ranging from 10 to 120 GW and the respective solar or photovoltaic (PV) capacity to meet the goal of decarbonization, as shown in Figure 4. Hydrogen storage and fuel cell system are coupled with renewable power generators due to low investment cost and technical feasibility. Pumped hydroelectric storage cannot compensate for a large amount of curtailed energy simply due to the lack of water in California. Compressed air energy storage stores energy as pressure, not as chemical potential energy, making its energy density orders of magnitude lower than that of BESS and compressed hydrogen storage. Only BESS and hydrogen storage, according to the investigation, are capable of storing all the otherwise curtailed energy with 100% use of solar and wind energy to meet the power demand. However, the cost estimate to store the curtailed energy differs significantly between BESS and hydrogen storage because the energy density of hydrogen is 200 times greater than that of a lithium-ion battery. The study found that in the BESS-

only case, the estimated investment cost for the storage system is 4046.2 billion dollars, whereas in the hydrogen-only case, the estimated investment cost is 73.3 billion dollars [5]. This results from the separate power and energy scaling that is possible with the hydrogen case (and not available to the BESS case) coupled with the massive magnitude of stored energy required to achieve 100% renewable energy. Since the cost for BESS is orders of magnitude higher than that of hydrogen, hydrogen storage yields more favorable outcomes when complete decarbonization is realized by coupling RES and energy storage systems.

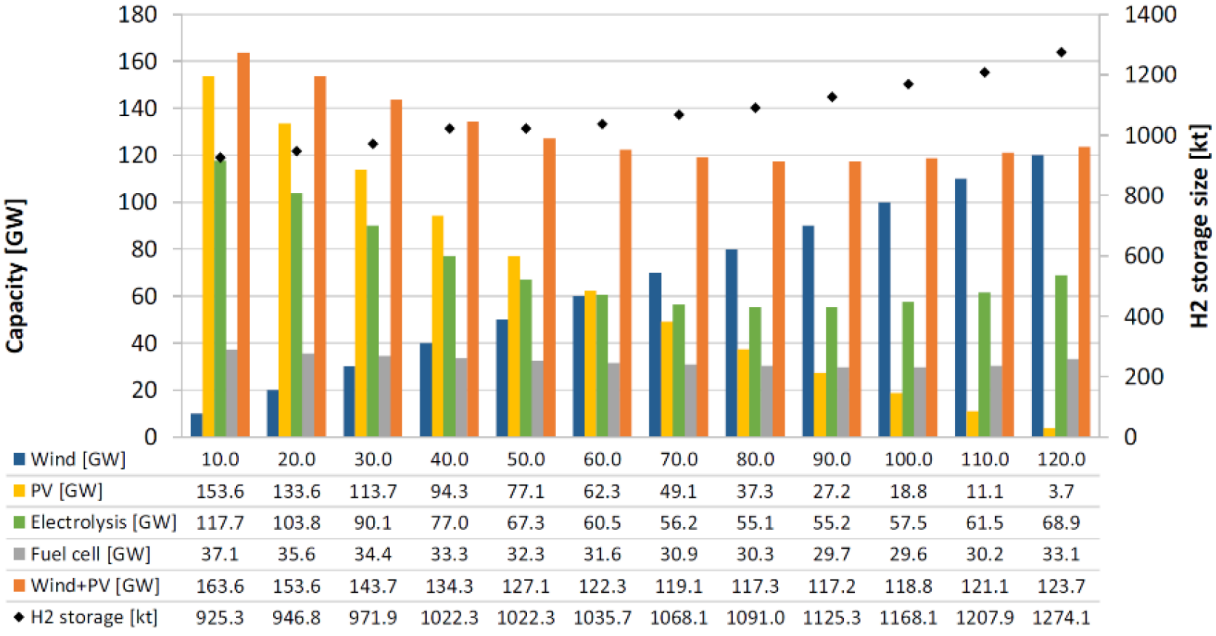

Wind [GW]	10.0	20.0	30.0	40.0	50.0	60.0	70.0	80.0	90.0	100.0	110.0	120.0
PV [GW]	153.6	133.6	113.7	94.3	77.1	62.3	49.1	37.3	27.2	18.8	11.1	3.7
Electrolysis [GW]	117.7	103.8	90.1	77.0	67.3	60.5	56.2	55.1	55.2	57.5	61.5	68.9
Fuel cell [GW]	37.1	35.6	34.4	33.3	32.3	31.6	30.9	30.3	29.7	29.6	30.2	33.1
Wind+PV [GW]	163.6	153.6	143.7	134.3	127.1	122.3	119.1	117.3	117.2	118.8	121.1	123.7
H2 storage [kt]	925.3	946.8	971.9	1022.3	1022.3	1035.7	1068.1	1091.0	1125.3	1168.1	1207.9	1274.1

Figure 4: Set of Combinations of Generation and Storage Capacities

Source: Adapted from [5]

1.5 Current Status of Hydrogen Production

Currently, 95% of the hydrogen produced in the United States is obtained by reforming natural gas in large steam methane reforming (SMR) plants [17]. Reforming natural gas to hydrogen is the leading technology in hydrogen production due to its low cost of production and technology maturity. However, producing hydrogen with natural gas emits GHG into the atmosphere. Besides hydrogen, carbon dioxide and carbon monoxide and water are produced as a result of the reforming process requiring separation and purification equipment downstream from the SMR process. To fully produce hydrogen renewably and sustainably, one must start with renewable primary energy inputs, which include biomass and biogas, which can be converted in thermochemical processes of gasification and SMR, respectively. In the end, due to the much more widespread availability of solar and wind power (compared to biomass and biogas resources) as renewable primary energy, most renewable hydrogen must be produced by water electrolysis with electricity generated by RES [18]. Unfortunately, water electrolysis is a minor contributor to the production of hydrogen today, only producing 4% of the global hydrogen production [19].

Water electrolysis is considered as a promising pathway for the production of sustainable hydrogen to be used as an energy carrier [20]. And the costs of both the primary energy itself (e.g., solar and wind power) and the energy conversion equipment (i.e., electrolyzers and fuel cells) are dropping rapidly in recent years. Among the existing water electrolysis technologies, high temperature or steam electrolysis offers additional advantages compared to low-temperature electrolysis [21]. High temperatures lead to

significantly lower electrokinetic losses (activation losses) and the Gibbs' free energy change (dg – i.e., electric input) of water electrochemical reduction reactions decreases with increasing temperature at constant pressure. These both contribute to potentially higher electrochemical conversion efficiency for high temperature electrolysis. On the other hand, the total enthalpy required for the thermodynamic process to occur (dh) slightly increases at higher temperatures. Therefore, using the fundamental laws of thermodynamics, it is clear that an increasing amount of thermal energy ($\delta q = Tds$) can be used, instead of electricity, to advance the reaction at higher temperatures [22] as follows.

$$dg = dh - Tds = dh - \delta q \tag{1}$$

$$\left(\frac{\partial g}{\partial T}\right)\Big|_p = -s(T,p) \tag{2}$$

$$\left(\frac{\partial (Ts)}{\partial T}\right)\Big|_p = s(T,p) + Tds(T,p) \tag{3}$$

In particular, the thermal energy has to more than compensate for the reduction in Gibbs' free energy at higher temperatures, as noticed from Eqs. (1) to (3).

1.6 CSP-Integrated Solid Oxide Fuel Cell and Control Strategies

High-temperature electrolysis can be performed with a solid oxide electrolysis cell (SOEC), and the total energy required for high-temperature electrolysis can be completely obtained from the sun. To assess the techno-economic performance of solar-integrated SOEC systems, Lin and Haussener analyzed three separate integration schemes that incorporated 1) concentrated solar technology, 2) PV technology, and 3) the combination

of both. The results showed that integrating concentrated solar plants with PV panels yielded the highest techno-economic performance [23]. Likewise, Boudries stated that a concentrated solar-integrated SOEC system achieves a lower cost of hydrogen production compared to a conventional PV-electrolysis system [24]. By coupling an SOEC system with a CSP plant, the electrical power demand is reduced due to the direct use of solar-thermal energy to preheat water as well as heating the SOEC to maintain the operating temperature [25]. Monnerie et al. simulated a high-temperature SOEC with a CSP plant that produces 400 kg of hydrogen per day. The work suggests that CSP plants can provide heat and electricity at the MW-scale to electrolyzers with molten salt as the working fluid [26].

CSP technologies are one of the forefront sources of renewable energy because of their dispatchability and built-in potential for energy storage. Energy is collected in the form of concentrated solar irradiation then used to power plants or perform other processes. Due to the intermittent nature of concentrated solar power, energy storage mediums are essential, as energy storage allows energy collection to be decoupled from electricity generation. Currently, parabolic trough, linear Fresnel, dish/engine, and central receiver technologies are deployed in typical CSP plants [27]. According to Mastropasqua et al., parabolic trough and linear Fresnel technologies are least suitable to integrate with high-temperature electrolyzers because, with such technologies, the salt cannot reach the typical inlet species temperature of high-temperature electrolyzers [28]. Houaijia et al. stated that to sufficiently raise the inlet species temperature without an external electric heater, a solar tower or solar dish receiver must be implemented [29]. Therefore, the system efficiency of solar-integrated electrolyzers using solar tower or dish receiver is

much higher than the electrolyzers using parabolic trough or linear Fresnel technology [30], [31].

Alzahrani et al. [32] integrated CSP and thermal energy storage (TES) with a steam turbine and an SOEC to produce hydrogen continuously even at times when solar energy is not available. The work of Alzahrani et al. suggests that solar-to-hydrogen conversion efficiency is found to be 12.7% while charging TES when solar energy is available, and 39.5% while discharging the working fluid from TES when solar energy is not available. The study concluded that the conversion efficiency of the integrated system is competitive with other renewable hydrogen production technologies, and may have more potential with a larger-scale application.

Saeedmanesh et al. [33] investigated the dynamic behavior of an SOEC system using transient energy generated by PV panels throughout the day. The study demonstrated a 300 kW SOEC system that is able to operate dynamically on both sunny and cloudy days with electricity generated by PV panels. During the dynamic operation, the average Positive Electrode-Electrolyte-Negative Electrode (PEN) temperature decreased in the early morning since the system operates endothermically with lower energy coming from solar. After sunrise, the average PEN temperature began to increase and reached the maximum as the system operates highly exothermically near the noon hour. Despite the highly dynamic operations on both sunny and cloudy days, the model demonstrated that the controlled system was able to maintain stack temperature within the safe operating range. However, the study suggests that due to the dynamic operation of the SOEC, the temperature

distribution and dynamics of temperature gradient could increase degradation of the stack which will negatively impact the performance of the system over time.

In addition, Saeedmanesh et al. [34] proposed two control strategies to control the operating temperature of the stack while producing hydrogen dynamically. In the first control strategy, the temperature of the stack is maintained by varying blower power—varying the amount of air through the stack. In the second control strategy, both the temperature and amount of air are varied. The two control strategies were able to maintain the localized PEN temperature gradient temperature while the system operated dynamically. Although both strategies were able to control the system within the safe limit, the first control strategy yielded higher system efficiency than the second control strategy because, in the second control strategy, power is additionally consumed by the electric heater.

Based on the studies investigated, producing hydrogen with high-temperature SOEC systems is a promising approach for California to attain the goal of 2045: meeting the power demand with only renewable energy and zero-carbon sources. With an exponential increase in solar energy capacity over the years [35], energy curtailment will likewise continue to increase due to non-coincidence with demand. However, with SOEC systems, the excess electricity from PV panels can be utilized to produce hydrogen, serving as both short- and long-duration energy storage with high energy density. Several researchers have already investigated the enhancement in the hydrogen production efficiency of SOEC systems integrated with CSP plants. However, more research is necessary to further

conceptualize the design of the integrated system, and investigate the dynamic performance characteristics and novel control strategies throughout the operation range.

1.7 The Role of Cement and Its Environmental Impacts

Cement is one of the most essential construction materials that is used in the production of structures such as buildings, bridges, harbors, runways, and roads. Because cement production and use are closely linked to infrastructure development, the production and consumption are broadly related to the general economic activity and prosperity. Since cement is essential for economic development, cement is produced in nearly every jurisdiction around the world. Cement production is an energy-intensive process where energy consumption by the cement industry is about 2% of the total global energy consumption which is about 5% of the world's total industrial energy consumption [36]. Cement production is also one of the highest carbon dioxide (CO_2) emitting manufacturing processes mainly due to the consumption of large quantities of fossil fuels together with the CO_2 emissions from calcination [37], [38].

Globally, the cement industry accounts for 8% of total anthropogenic CO_2 emissions [39]. In addition to the CO_2 emissions from burning fossil fuels for the process, CO_2 is also emitted from the raw material during calcination. For Portland cement production, Worrell et al. [40] estimated that roughly half of the CO_2 emissions come from combustion of fossil fuels and the other half of the CO_2 emissions comes from the chemical conversion of the raw material. The most relevant chemical reaction that takes place during calcination is shown below:

$$CaCO_3(s) \rightarrow CaO(s) + CO_2(g), \Delta H_{rnx} = 3180 \frac{kJ}{kg} CaO \text{ @ } 25°C \quad (4)$$

Clinker is a solid material that is used as the binder in cement production. The CO_2 emissions from clinker production amount to about 0.5kg/kg of clinker. However, the CO_2 emissions from calcination ultimately depend on the ratio of clinker to cement which normally varies from 0.5 to 0.95. Besides the CO_2 emissions from calcination, CO_2 is additionally emitted in the kiln where fuel is also used for pyro-processing. The emissions are specifically determined by the type of fuel used in the kiln. Typical types of fuel used are coal, fuel oil, natural gas, petroleum coke, and alternative fuels. CO_2 is also emitted from the consumption of electricity in cement plants, but the amount of emissions is significantly lower compared to the emissions coming from the manufacturing process.

Worrell et al. [40] stated that key cement-producing countries are China, India, the United States, Japan, and South Korea. The CO_2 emissions from these key countries alone account for 63% of the world's carbon emissions from cement production. Therefore, these key countries must lead the effort to reduce and even eliminate CO_2 emissions from cement production. The United States should lead the world in achieving carbon neutrality with technological advances that could realize carbon neutrality in the cement industry.

1.8 Solutions to Mitigate CO_2 Emissions from Cement Plants

Under the Biden administration, a goal is proposed to achieve a net-zero emissions economy by no later than 2050 [41]. As a matter of fact, the California Nevada Cement Association (CNCA) has recently announced a plan for the industry to achieve net-zero

carbon emissions by 2045 [42]. Several options have been investigated to reduce the carbon emissions using alternative fuels [43], [44], coupling carbon capture technologies [45]–[48], and integrating a CSP plant with a concentrated solar reactor replacing a conventional coal-fired calciner [49]–[52].

Tomatis et al. [53] separately analyzed alternative fuels, solar thermal energy, and carbon capture and storage (CCS) to be employed in a conventional cement plant to mitigate climate change and other environmental impacts from cement production. Based on the life cycle analysis, the study concluded that integration of solar thermal energy to a conventional cement plant, specifically replacing a conventional calciner with a concentrated solar calciner, and CCS resulted in the most environmentally sustainable option. Using alternative fuels such as municipal solid waste, waste oil, waste solvents, and tire-derived fuel was found to be less favorable due to much higher human toxicity and ecotoxicity compared to the conventional fuels used. Coupling CCS without solar thermal energy integration decreased the climate change impact by 63% while coupling CCS with solar thermal energy decreased the climate change impact by 81%. Therefore, Tomatis et al. suggested that to achieve decarbonization in the cement industry, thorough performance and economic assessments are needed for solar thermal and CCS integration in conventional cement plants.

Meier et al. [49] were some of the earlier researchers that studied a solar-integrated lime plant that has a production capacity of 50 tons of lime per day. Although the study used constant direct normal irradiance (DNI) and without thermal storage, as one of the pioneering studies on solar thermal lime production, the economic assessment of solar-

integrated lime production showed a promising outlook. The assessment showed that the cost of lime per ton is reduced as the capacity of the solar-integrated lime plant gets larger. Although the cost of solar-produced lime is higher than that of the actual market price, a much lower cost of solar-produced lime can be expected from the economy of scale in the future. The paper strongly suggested that adequate government subsidies and higher carbon tax should be implemented to urge such industries to adopt solar-integrated lime production, ultimately reducing the greenhouse gas emissions released by fossil fuels.

Gonzalez and Flamant [52] successfully proved the feasibility of a solar-integrated cement plant using concentrated solar thermal technology (CST) with thermal storage. The considered capacity of the plant was 3000 ton of clinker per day. Fuel substitution of the solar calciner in the range of 40-100% is evaluated with the annual DNI of 2550 kWh/m^2. The raw meal is calcined at 900°C in the solar calciner. The calcined meal is then fed to the kiln for sintering. The study found that the most suitable way of applying CST in conventional cement plants is using a solar tower where a solar calciner is placed at the top of the tower. Such implementation does not radically change the conventional process and substantially reduce the carbon emissions from burning fossil fuels. Economically, the solar-integrated cement plant is also found to be feasible. The payback times obtained are much lower than that of conventional CSP plants.

Moumin et al. [51] further investigated the techno-economic potential of solar-assisted cement plants. The conceptualized solar-integrated cement plant is located in Almeria, Spain, with a fixed DNI potential of 2207 kWh/m^2. The capacity of the cement plant investigated is 3000 ton of clinker per day which is identical to the study done by

Gonzalez and Flamant. To evaluate the conceptualized solar-integrated cement plant, a sensitivity analysis is conducted. The reactor efficiency, DNI, solar multiple, and combinations of these are varied. The study found that the maximum CO_2 avoidance rate is 20% in comparison to the overall cement plant emissions. The lowest clinker cost, 71 EUR/t, is achieved when a solar multiple of 2.5 and higher reactor efficiency are applied. However, the highest reduction in the CO_2 emissions, 17%, is achieved with the highest solar multiple applied in the study which is 3.5.

As stated earlier, CO_2 emissions occur from the combustion of fossil fuels and the conversion of raw materials. To effectively reduce the CO_2 emissions from cement production, Gardarsdottir et al. and Voldsund et al. [54], [55] stated that implementation of CCS was found to have the largest CO_2 emissions reduction potential. The study done by Voldsund et al. [55] presented the performance characteristics of CCS technologies retrofitted in a Best-Available-Technologies (BAT) cement plant. The study investigated monoethanolamine (MEA)-based absorption, chilled ammonia process (CAP), membrane-assisted CO_2 liquefaction (MAL), oxyfuel technology, a tail-end and integrated calcium looping technology (CAL). The estimated costs of clinker using the listed CCS technologies are calculated with the capital costs, fuel costs, raw material costs, electricity costs, and operating and maintenance costs. The CO_2 avoidance costs are also estimated for each CCS technology which is based on the costs of clinker and the equivalent specific emissions of the cement plant with and without CCS.

The cost analysis from Gardarsdottir et al. [54] showed that the costs of clinker for calcium looping (both tail-end and integrated), CAP, and MEA technologies range from 105

– 110 Euro per ton of clinker. The lowest cost of clinker is achieved with oxyfuel technology while the highest cost of clinker is achieved with MAL technology. As far as CO_2 avoidance cost is concerned, the lowest CO_2 avoidance cost, 42 Euro per ton of clinker, is again achieved with oxyfuel technology. Although MEA technology has the lowest CAPEX, the CO_2 avoidance cost is doubled compared to that of oxyfuel technology mainly due to higher OPEX and the lowest CO_2 capture potential. Therefore, the CAPEX, OPEX, and amount of captured CO_2, all contribute to determining the CO_2 avoidance costs. The detail of the analysis is shown in Table 1.

Table 1: Summary of Cost Analysis [54]

	Ref. Cement Plant	MEA	Oxyfuel	CAP	MAL	CaL-Tail-End	CaL-Integrated
TPC, cement plant + CO_2 capture plant (M€)	204	280	332	353	450	406	424
TPC, CO_2 capture plant (M€)	-	76	128	149	247	202	220
Annual OPEX (M€)	41	76	58	66	71	59	61
Cost of clinker (€/t_{clk})	62.6	107.4	93.0	104.9	120.0	105.8	110.3
Cost of CO_2 avoided (€/t_{CO2})	N/A	80.2	42.4	66.2	83.5	52.4	58.6

Several options have been investigated to reduce the carbon emissions from cement plants using alternative fuels, coupling CCS technologies, and integrating with CSP plants. Although several studies have investigated CSP-integrated cement plants, these studies have not yet considered the dynamics of solar calciner as well as thermal storage for storing calcined clinker. Also, these studies have not analyzed regions where actual cement plants are located in the United States and compared the advantages of integrating CSP with cement plants over other existing CCS technologies.

2. Goal and Objectives

2.1 Goal

The goal of this work is to design and evaluate the dynamic performance characteristics of a concentrated solar integrated solid oxide cell system, while managing temperature and temperature gradients in the system, and to assess techno-economics of a concentrated solar integrated cement plant.

2.2 Objectives

1. **Conduct a thorough literature review on CSP plants, SOEC systems, cement plants, and carbon capture technologies**

   A literature review will be conducted to obtain background knowledge of CSP plants, SOEC systems, cement plants, electricity curtailments from RES in California, energy storage systems, CCS technologies, and modeling in MATLAB. Solar thermal power plants will be reviewed to gather information on different components of the plant as well as typical working fluids. Data on the direct normal irradiance profile with high resolution will be gathered from various regional jurisdictions. Literature review on energy storage systems, SOEC, cement plants, and CCS technologies will continue throughout the work.

2. **Conceptualize the design of the integrated CSP+SOEC system that would meet the dynamic and thermal management requirements.**

Different types of CSP plants will be reviewed to conceptualize the design of the integrated system. Based on the selected type of concentrated solar technology used for the system, the locations of pertinent components will be determined to satisfy thermal management requirements and various dynamic loads and demands. After the integrated system is conceptualized, a model will be developed to simulate and evaluate the dynamic performance characteristics of the system.

3. **Develop a dynamic model of CSP-integrated plants using MATLAB.**

   Using the data obtained from the literature review, a dynamic model of CSP+SOEC system will be developed in MATLAB. Modeling the CSP portion of the integrated system will be the main focus of Task 3. Once the CSP portion of the modeling is completed, collaborate with researchers to integrate the CSP with an SOEC system. Once the model is validated, sets of parameters will be defined to vary the operating conditions. The model will be used to evaluate different operating strategies under different conditions and determine the viability of the system.

4. **Evaluate performance characteristics of the CSP-integrated SOEC system.**

   A dynamic model of CSP+SOEC system will be used to evaluate the dynamic behavior and performance characteristics, aiming to achieve high hydrogen production efficiency and to minimize the balance of plant power consumption. To minimize the SOEC stack degradation, the average stack temperature will be

controlled with PI controllers. Daily hydrogen production with the integrated system operating on solar energy will be analyzed.

5. **Evaluate performance characteristics of CSP-integrated cement plants in regions with different DNI potentials.**

   Five different cement plants across the United States will be chosen where each location has different DNI potentials. Each cement plant will be integrated with a CSP plant. Solar thermal energy will be used in a calciner instead of fossil fuels. The dynamics of solar calciner, thermal storage, amount of fossil fuel saved from utilizing solar thermal energy, and reduction in the CO_2 emissions will be investigated at each location.

6. **Evaluate the economics of CSP-integrated cement plants in the selected regions.**

   The capital and operating expenditures will be estimated for each CSP-integrated cement plant studied. Based on the expenditures and the CO_2 emissions associated with each location, the economics of CSP-integrated cement plants will be evaluated. The CO_2 avoided costs from the integrated plants will be compared to that of cement plants integrated with existing carbon capture technologies. Lastly, based on the CO_2 avoided costs, the threshold DNI potential that makes the CSP integration economically competitive will be determined.

3. Methodology

A dynamic concentrated solar-integrated SOEC system model has been developed to evaluate the performance characteristics of the integrated system while managing temperature and temperature gradients in the system, and the system schematic is shown in Figure 5. An SOEC system model without an external heat source was previously developed at the National Fuel Cell Research Center (NFCRC) investigating system performance characteristics while following transient PV generated power as an input to produce renewable hydrogen to be injected into the natural gas grid [34], [56]. The previously developed model is modified to be integrated into a CSP plant. A CSP plant model comprised of a heliostat field, solar tower receiver, thermal energy storage, and heat exchangers to harvest thermal energy to be supplied to the SOEC system is developed. Using the integrated model, the dynamic performance characteristics of the integrated system are investigated. It should be noted that in this study, a case without thermal storage is analyzed, to determine whether thermal management is possible when the steam produced by the salt follows the DNI profile during the day. Table 2 presents the integrated system parameters.

Table 2: Integrated System Parameters

CSP parameter	**Value**
Area of Heliostats	144.375 m^2
Diameter of the Solar Receiver	5.11 m
Diameter of the Tubes	32 mm
Height of the Panel	3.51 m
Height of the Solar Tower	50.8 m
Location of the CSP Plant	Imperial, California, USA
Nominal Direct Normal Irradiance	950 W/m^2
Nominal Thermal Power	20 MW_{th}
Number of Heliostats	370
Number of Panels	20
Thickness of the Tubes	1.25 mm
SOEC System Parameter	**Value**
Area Specific Resistance	0.6 $\Omega.cm^2$
Nominal Blower Power	52 W
Nominal Cell Current Density	0.436 A/cm^2
Nominal Cell Voltage	1.25 V
Nominal Electric Heater Power	19 kW
Nominal Stack Power	54.6 MW
Number of Cells	999810
Operating Temperature	1023 K
Steam Utilization	85%

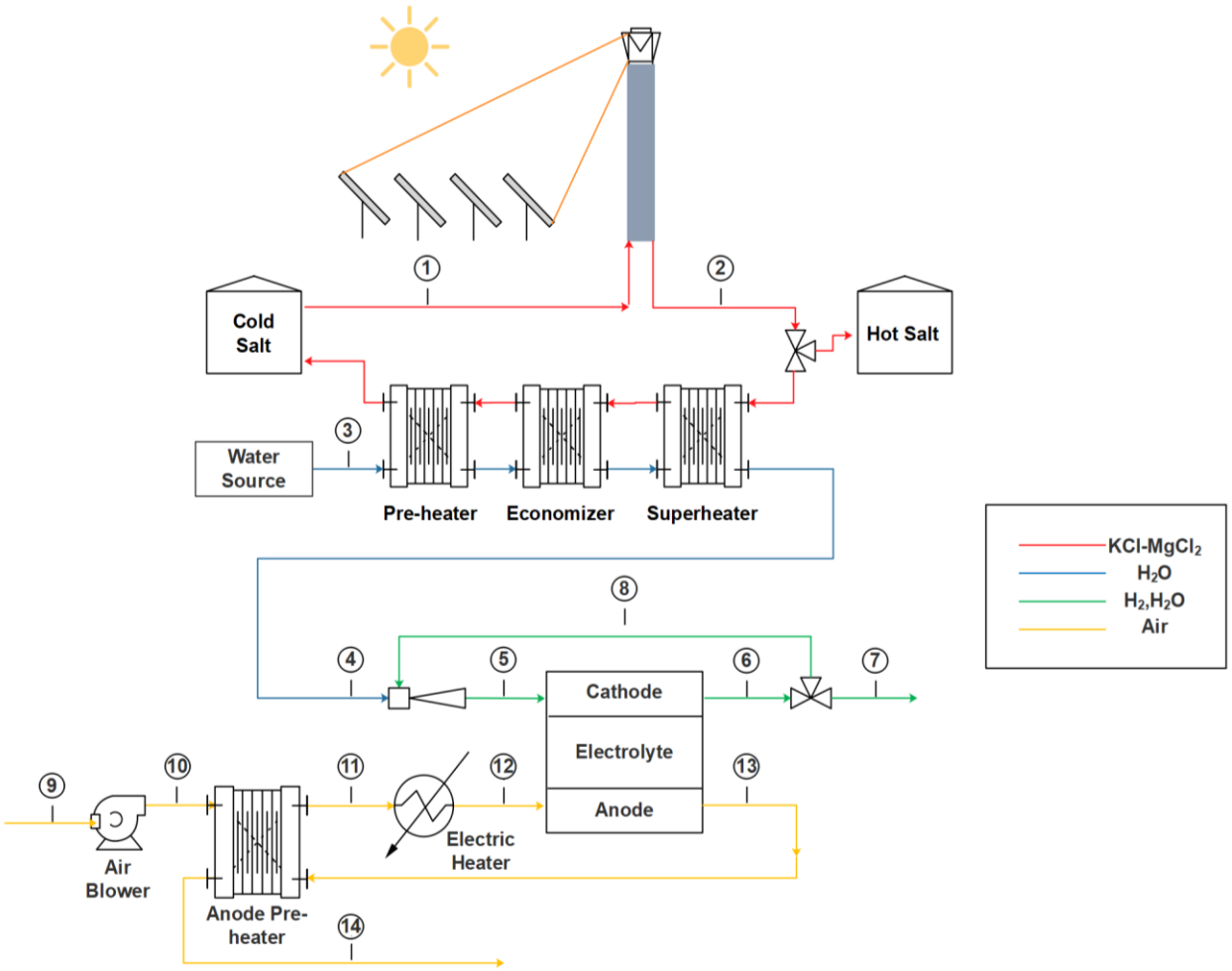

Figure 5: Concentrated Solar-integrated SOEC System Layout

3.1 CSP Plant Model Development

The first location selected for simulation of the CSP plant is Imperial, California. The site is chosen due to the location's high DNI profile. For the default design, hot salt is not stored for later use during the day. Instead, the entire hot salt stream is fed to the heat exchangers for steam production. As a result, both the salt and steam flow rates are proportional to the DNI profile. The CSP plant is simulated with the data measured during a

typical sunny day in winter collected from System Advisor Model (SAM) [57]. The plant is designed to output 20 MW_{th} of thermal power at the nominal condition. A magnesium chloride-potassium chloride (KCl-$MgCl_2$) molten salt solution (molar composition: 68-32%) is used to produce high-temperature steam. The salt enters the solar receiver (stream #1) at 700 K where it is heated up to 1200 K as the salt exits the receiver (stream #2). The hot salt then goes through the heat exchangers to generate high-temperature steam to be utilized in the SOEC stack. The mass flow rate of the salt into the solar receiver is controlled to keep the outlet temperature (stream #2) at 1200 K. The properties of KCl-$MgCl_2$ are experimentally measured by Xu et al. which are shown in Table 3.

Table 3: Properties of KCl-MgCl2 (mole: 68%-32%) [58]

Parameter	**Value or functions of temperature, T(°C)**
Boiling point (°C)	1418
Density (kg/m^3)	$\rho = 1903.7 - 0.552 \times T$
Heat Capacity (J/g.K)	$Cp = 0.9896 + 1.046 \times 10^{-4} \times (T - 430)$
Melting Point (°C)	427
Thermal Conductivity (W/m.K)	$\kappa = 0.5047 - 0.0001 \times T$
Viscosity (cP)	$\mu = 14.965 - 0.0291 \times T + 1.784 \times 10^{-5} \times T^2$

As shown in Figure 6, the concentrated solar receiver that is modeled in this study is a cylindrical solar tower receiver that is comprised of rectangular panels connected in series along the circumference, and the salt enters from the south-most panel and loops through the receiver. Each panel has vertical tubes for the salt to travel through and absorb

thermal energy garnered from the heliostats. Within the panel, tube-to-tube conduction and radiation exchange are neglected. Regarding the heat flux distribution on the panels, Wagner investigated the effect of reducing the number of computational nodes on the cylindrical solar receiver and concluded that there is a negligible effect in the temperature of the fluid leaving the system as the number of nodes is reduced to one per panel [59]. Therefore, in this study, a one-dimensional model of the heat flux distribution across the panels was simulated, where each panel experiences one flux data point.

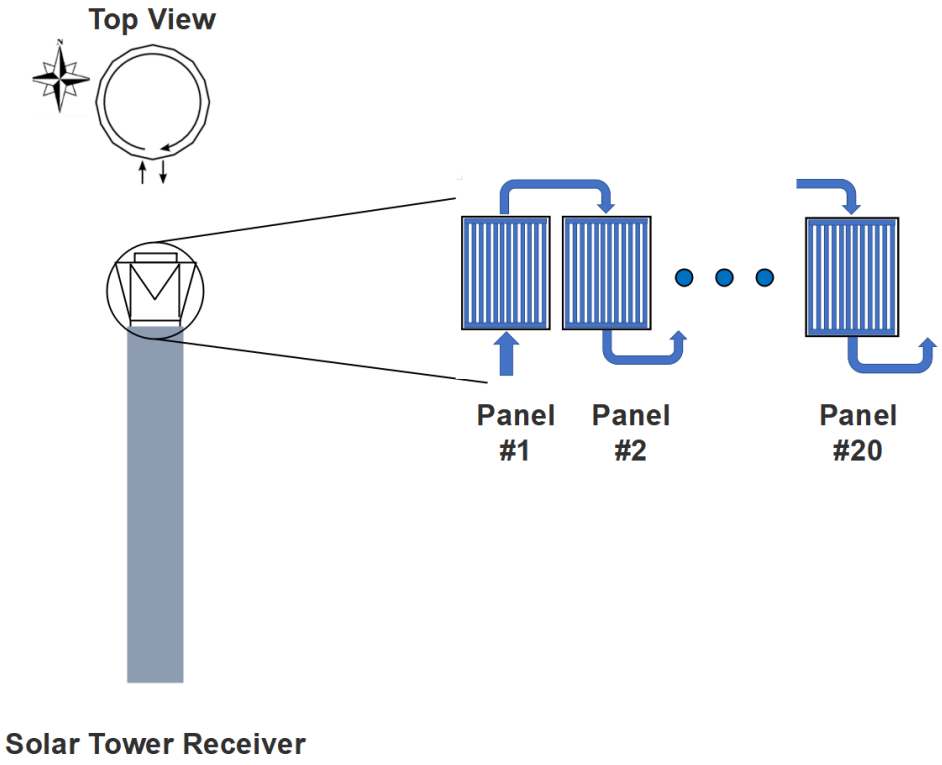

Figure 6: Solar Tower Receiver Physical Layout Modeled

Using SAM, the optimal locations and angles of the heliostats were determined based on the designed thermal power of the receiver [57]. Based on the optimization, the incident thermal power with an hourly resolution is obtained based on the heat flux data,

direct normal irradiance, and field optical efficiency. With the given incident thermal input, the salt temperature dynamics are computed in MATLAB by accounting for thermal losses along and within the receiver panels. The governing equation for the solar tower receiver is shown below

$$\rho V C_p \frac{\partial T_{salt}}{\partial t} = \dot{Q}_{in} - \dot{Q}_{rad} - \dot{Q}_{conv} + \dot{H}_{in} - \dot{H}_{out} \quad (5)$$

where $\dot{H}_{in}$ and $\dot{H}_{out}$ are the enthalpy terms at the inlet and outlet at each node, ρ, V, C_p, and T_{salt} are density, volume, specific heat, and temperature of the salt, respectively. The thermal energy balance for the panel and tower is not accounted for the dynamic simulation due to large thermal mass of the salt.

3.1.1 Thermal Losses

The temperature of the salt is determined by the incident thermal power to the receiver, radiation from the receiver surface, and convection to the surrounding air. Because of the high surface temperature, radiative heat transfer plays a dominant role in the calculations. To evaluate the radiation loss, the ambient air temperature and the effective sky temperature are considered with the corresponding view factors [59]. The view factor between the ground and the receiver, and the sky and the receiver are 0.5 for both. Eqs. (6) – (8) show how the radiation loss is calculated [59]

$$\dot{Q}_{rad,loss} = h_{rad,amb} \times A_s(T_s - T_{amb}) + h_{rad,sky} \times A_s\left(T_s - T_{sky}\right) \quad (6)$$

$$h_{rad,amb} = \sigma \times \varepsilon \times F_{s,amb} \times (T_s^2 + T_{amb}^2) \times (T_s + T_{amb}) \quad (7)$$

$$h_{rad,sky} = \sigma \times \varepsilon \times F_{s,sky} \times \left(T_s^2 + T_{sky}^2\right) \times \left(T_s + T_{sky}\right) \quad (8)$$

where h is the heat transfer coefficient, A_s is the surface area of the panel, ε is the surface emissivity, σ is the Stefan-Boltzmann constant, and T_s, T_{sky}, and T_{amb} is the surface, sky, and ambient temperature, respectively.

To determine the surface temperature, the thermal resistance network of conduction and internal convection between the surface and the fluid is considered. The conduction resistance is determined by the geometry of the tube within the receiver panel. The inner convection resistance is determined by convection correlations for flow in a circular tube. For convective heat transfer, both natural convention and force convection losses are considered. For natural convection calculation, a vertical flat-plate correlation is used for the panels. Particularly, the Siebers and Kraabel correlation is used. Forced convection losses are calculated based on the range of Reynolds number and surface roughness. To get the total convection loss, the mixed convection relationship is used where the value *m* indicates the degree of dominance of the larger convection coefficient over the smaller. The value of *m* is set to be 3.2. Relevant equations used for the convection losses are listed below [59], [60]

$$\dot{Q}_{conv} = h_{mixed} \times A \times (T_s - T_f) \quad (9)$$

$$Gr = 9.81 \times \frac{1}{T_f} \times (T_s - T_{amb}) \times \left(\frac{H_{rec}^3}{\nu_{amb}^2}\right) \quad (10)$$

$$Nu_{natural} = 0.098 \times Gr^{\frac{1}{3}} \times \left(\frac{T_s}{T_{amb}}\right)^{-0.14} (Siebers\ and\ Kraabel) \quad (11)$$

$$Nu_{forced} = \begin{cases} 0.3 + 0.488 \times Re^{0.5}\left(1 + \left(\frac{Re}{282000}\right)^{0.625}\right)^{0.8}, Re \leq 1.8 \times 10^5 \\ 0.0135 \times Re^{0.89}, \ 1.8 \times 10^5 < Re < 4.0 \times 10^6 \\ 0.0455 \times Re^{0.81}, \ Re \geq 4.0 \times 10^6 \end{cases} \quad (12)$$

$$h_{mixed} = \left(h_{natural}^m + h_{forced}^m\right)^{1/m} \quad (13)$$

whereh_{mixed}, $h_{natural}$, h_{forced} is the mixed, natural, and forced convective heat transfer coefficient, respectively. H_{rec} is the height of the receiver, ν_{amb} is the kinematic viscosity of the ambient, Re is the Reynolds number, T_f is the film temperature, Gr is the Grashof number, and $Nu_{natural}$ and Nu_{forced} is the Nusselt number for natural and forced convection, respectively

To determine the surface temperature, conduction heat transfer between the surface and the fluid must be considered. Figure 7 shows the resistance network for the tubes within the receiver panel.

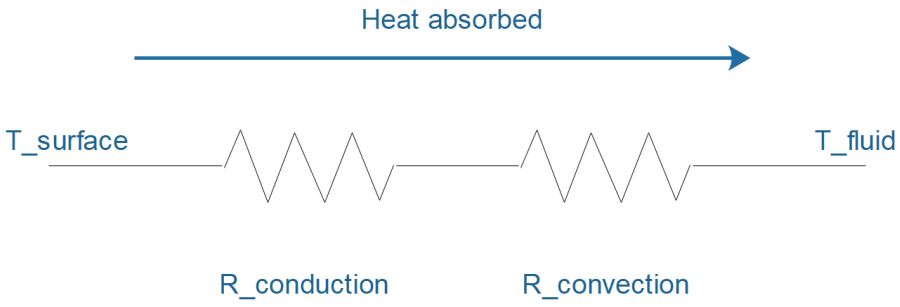

Figure 7: Resistance Network for the Tubes in each Panel

Knowing the equivalent thermal resistance, the temperature of the thermal fluid, and the heat absorbed, the surface temperature can be found which plays a critical role in the radiative heat transfer for the receiver. The surface temperature is calculated as follows:

$$T_s = T_{salt,ave} + \dot{Q}_{net} \times (R_{inner} + R_{cond}) \tag{14}$$

The inner convection resistance is determined by the Nusselt number of the salt in the tube which depends on the Prandtl and Reynolds numbers. Depending on the range of the Prandtl and Reynolds numbers, a specific Nusselt formula must be applied accordingly. For the calculation of the inner thermal resistance, only half of the surface area is considered because the backside of the tube is assumed to be adiabatic. The conduction resistance, on the other hand, simply depends on the geometry of the tube. The equations used to calculate the thermal resistances are shown below:

$$Nu_{inner} = 0.023 * Re^{\frac{4}{5}} \times Pr^{0.4}\,, 0.6 \leq Pr \leq 160, Re_D \geq 10{,}000 \tag{15}$$

$$Nu_{inner} = \frac{\left(\frac{f}{8}\right)(Re_D - 1000)Pr}{1 + 12.7\left(\frac{f}{8}\right)^{\frac{1}{2}}(Pr^{\frac{2}{3}} - 1)}, 0.5 \leq Pr \leq 2000, 3000 \leq Re_D \leq 5 * 10^6 \tag{16}$$

$$\frac{1}{\sqrt{f}} = -2.0\log\left(\frac{\frac{e}{D}}{3.7} + \frac{2.51}{Re_D\sqrt{f}}\right) \tag{17}$$

$$R_{inner} = \frac{1}{h_{inner} * \frac{\pi}{2} * D_{inner} * n_{tubes} * H_{rec}} \tag{18}$$

$$R_{cond} = \frac{\ln \frac{r_{outer}}{r_{inner}}}{k_{tube} \times 2 \times \pi \times H_{rec} \times n_{tubes}} \quad (19)$$

where Nu_{inner} is the Nusselt number for internal convection, Pr is the Prandtl number, f is the friction factor, e is the surface roughness, D is the diameter, n_{tubes} is the number of tubes, R_{inner} is the internal thermal resistance, R_{cond} is the conduction thermal resistance, k_{tube} is the thermal conductivity of the tube, and r_{outer} and r_{inner} is the outer and inner radius of the tubes, respectively.

3.1.2 Heat Exchanger

A pre-heater, boiler, and super-heater are used to generate steam for high-temperature electrolysis. However, only the super-heater is modeled dynamically. The mass flow rate of water is determined by considering the energy balance of the three heat exchangers. With the outlet temperature of the superheater, the heat of vaporization of water, and the inlet temperature of water at the economizer, the corresponding mass flow rate of water is determined such that the energy balance of the three heat exchangers holds true. Then, the super-heater is simulated dynamically based upon the geometry and physics of the heat exchange with flow rate values found from the previous heat exchanger energy balances. On the other hand, the economizer and evaporator are simulated in off-design as a consecutive and instantaneous succession of steady-state points.

The superheater is modeled as a one-dimensional counter flow plate heat exchanger where the heat exchanger wall separates the cold and hot streams. The wall and the

streams are discretized into small control volumes where the mass and energy balances are computed. The following equations show relevant mass and energy balances

$$\frac{\partial \rho A_{cr}}{\partial t} + \frac{\partial \dot{m}}{\partial x} = 0 \tag{20}$$

$$(\rho V)_{cv} \frac{dh_{cv}}{dt} = \dot{Q}_{cv} + \dot{H}_{in} - \dot{H}_{out} \tag{21}$$

$$\dot{Q}_{cv} = A * U * (T_{wall} - T_F) \tag{22}$$

$$\rho_{wall} V_{wall} C_{p,wall} \frac{dT_{wall}}{dt} = \dot{Q}_{HF} - \dot{Q}_{CF} \tag{23}$$

where A_{cr} is the cross-sectional area, $\dot{m}$ is the mass flowrate, h_{cv} is the specific enthalpy of the control volume, $\dot{H}_{in}$ is the inlet enthalpy, $\dot{H}_{out}$ is the outlet enthalpy, U is the overall heat transfer coefficient, T_{wall} is the temperature of the wall which separate the cold and hot fluid, T_F is the fluid temperature, and $\dot{Q}_{cv}, \dot{Q}_{HF}, and\ \dot{Q}_{CF}$ is the heat transfer rate of the control volume, hot fluid, and cold fluid, respectively. Equation (22 can be used to calculate the heat transfer rate of both hot and cold fluid inside the heat exchanger.

3.2 SOEC System

A thermo-physical dynamic SOEC system model (both stack-level and system-level) is deployed to evaluate the dynamic behavior of the SOEC system. The stack model resolves a single repeat unit cell that is scaled to describe the response of the whole stack. Each unit cell is a cathode-supported (fuel electrode-supported) planar square-geometry cell with an active surface area of 100 cm^2. The deployed model considers 5 different layers for each individual cell: cathode stream, anode stream, PEN, fuel side (cathode) interconnect plate and air side (anode) interconnect plate. Each of the mentioned layers of the planar SOEC

cell is spatially and temporally resolved in a 10×10 resolution domain. The governing equations including electrochemical model, mass balance, and energy balance are locally solved in each control volume using the finite volume method [56].

The electrochemical model is shown in Eq (24). A temperature-dependent Area Specific Resistance (ASR) is used to integrate all the irreversible losses

$$V_{cell} = -\frac{\Delta G_f}{2 \times F} + \frac{R \times T_{pen}}{2 \times F} \times \ln\left(\sqrt{p_A} \times \frac{\chi_{H_2} \times \sqrt{\chi_{O_2}}}{\chi_{H_2O}} + ASR_{cell}(T_{pen})\right) \times j \tag{24}$$

where ΔG_f is the molar change in Gibbs free energy of formation of water conversion to hydrogen and oxygen at the PEN noddal tempreature T_{pen}, F is the Faraday constant, p_A is anode stream pressure, R is the universal gas constant, χ_i is the molar fraction of species i, and j is the current density.

The governing equations used for the mass balance are shown below from Eqs. (25) – (28):

$$\frac{p_C \times V_C}{R \times T_C} \times \frac{d\chi_{H_2O}}{dt} = \left(\dot{n}_C \times \chi_{H_2O}\right)_{in} - \left(\dot{n}_C \times \chi_{H_2O}\right)_{out} + \frac{I}{2 \times F} \tag{25}$$

$$\frac{p_C \times V_C}{R \times T_C} \times \frac{d\chi_{H_2}}{dt} = \left(\dot{n}_C \times \chi_{H_2}\right)_{in} - \left(\dot{n}_C \times \chi_{H_2}\right)_{out} - \frac{I}{2 \times F} \tag{26}$$

$$\frac{p_A \times V_A}{R \times T_A} \times \frac{d\chi_{O_2}}{dt} = \left(\dot{n}_A \times \chi_{O_2}\right)_{in} - \left(\dot{n}_A \times \chi_{O_2}\right)_{out} - \frac{I}{4 \times F} \tag{27}$$

$$\frac{p_A \times V_A}{R \times T_A} \times \frac{d\chi_{N_2}}{dt} = \left(\dot{n}_A \times \chi_{N_2}\right)_{in} - \left(\dot{n}_A \times \chi_{N_2}\right)_{out} \tag{28}$$

where $\dot{n}$ is the molar flowrate in the cathode or anode channel, I is current which is defined to be negative, and p, V, and T are the pressure, volume, and temperature of the respective channel node.

The governing equations for the energy balance are shown in Eqs. (29) – (32). Each control volume of the cathode channels, PEN layer, anode channels, and interconnet plates are analyzed

$$\rho_C \times c_{pC} \times V_C \times \frac{dT_C}{dt} = \dot{Q}_{cond} + \dot{Q}_{conv} + \dot{H}_{in} - \dot{H}_{out} - \frac{I}{2 \times F}(h_{H2} - h_{H_2O}) \tag{29}$$

$$\begin{aligned} &\rho_{PEN} \times c_{PEN} \times V_{PEN} \times \frac{dT_{PEN}}{dt} \\ &\qquad = \dot{Q}_{cond} + \dot{Q}_{conv} + \frac{I}{2 \times F}\left(h_{H2} + \frac{1}{2}h_{O_2} - h_{H_2O}\right) - V_{cell} \times I \end{aligned} \tag{30}$$

$$\rho_A \times c_{pA} \times V_A \times \frac{dT_A}{dt} = \dot{Q}_{cond} + \dot{Q}_{conv} + \dot{H}_{in} - \dot{H}_{out} - \frac{I}{4 \times F} \times h_{O_2} \tag{31}$$

$$\rho_{IC} \times c_{IC} \times V_{IC} \times \frac{dT_{IC}}{dt} = \dot{Q}_{cond} + \dot{Q}_{conv} \tag{32}$$

where $\dot{H}_{in}$ and $\dot{H}_{out}$ are the total enthapy at the inlet and outlet of the gaseous nodes, respectively. ρ is the density, V is the volume, and c and c_p are the specific heat capacity of the solid material and gas mixture, respectively. More details of the SOEC dynamic model are presented by Saeedmanesh et al. in [56].

The SOEC system configuration is developed to realize a concentrated solar-integrated SOEC system where the energy inputs are thermal energy, in the form of

superheated steam, and electrical energy. Referring to Figure 5, two inlet streams are present: superheated steam (stream #4) and ambient air (stream #9). The superheated steam coming from CSP plant is introduced to the cathode side of the system with dynamic flow rate. In the ejector, the steam flow is mixed with a partially recirculated cathode outlet flow to obtain 10% molar fraction of hydrogen at the cathode inlet (stream #5) to prevent oxidation of stack materials at high operating temperature. The steam-rich steam/hydrogen mixture goes to the electrolyzer stack where the electrochemical reactions take place, resulting in a hydrogen-rich mixture at the stack outlet (stream #6). A proportional-integral (PI) feedback controller is developed to control the recirculation valve that splits a portion of the outlet flow to have the desired hydrogen concentration at the cathode inlet. Air on the other side is introduced to the anode side of the SOEC system by a variable-speed blower, which provides both the required mass flow rate and pressure head. The supplied air is preheated in a counter-flow plate heat exchanger and heated to the desired temperature by an electric heater to reach the desired temperature before the anode inlet (stream #12). The anode outlet flow (stream #13), which is enriched by the oxygen generated as a byproduct of the electrochemical reaction, passes through a counter-flow heat exchanger for heat recovery purposes.

3.2.1 Thermal Control Strategy

The primary objective of the control strategy is to thermally manage the system within safe operating conditions to minimize degradation and maximize system efficiency. As the stack operates dynamically in different operating conditions the stack may require additional cooling or heating depending upon the operating voltage. To thermally manage

the SOEC stack during the dynamic operation, air flow rate and anode inlet temperature are adjusted to keep the temperature difference along the anode side of the stack and anode outlet temperature (which represents the stack temperature) at desired values. The temperature difference along the anode side should be controlled to prevent a high-temperature gradient along the solid structure and the consequent thermo-mechanical stress. On the other hand, the stack average temperature should be maintained almost constant to prevent voltage degradation due to the temporal temperature variation and to allow for continuous operation. The spatial temperature gradient is controlled by manipulating the blower power, while the stack average temperature is controlled by manipulating the electric heater power in two independent PI feedback controllers. In the developed controller, the anode inlet temperature setpoint (stream #12 of Figure *5*) is 1123 K and the anode stream spatial temperature gradient is 100 K. The control scheme of all the PI feedback controllers that are used in the SOEC system is shown in Figure 8.

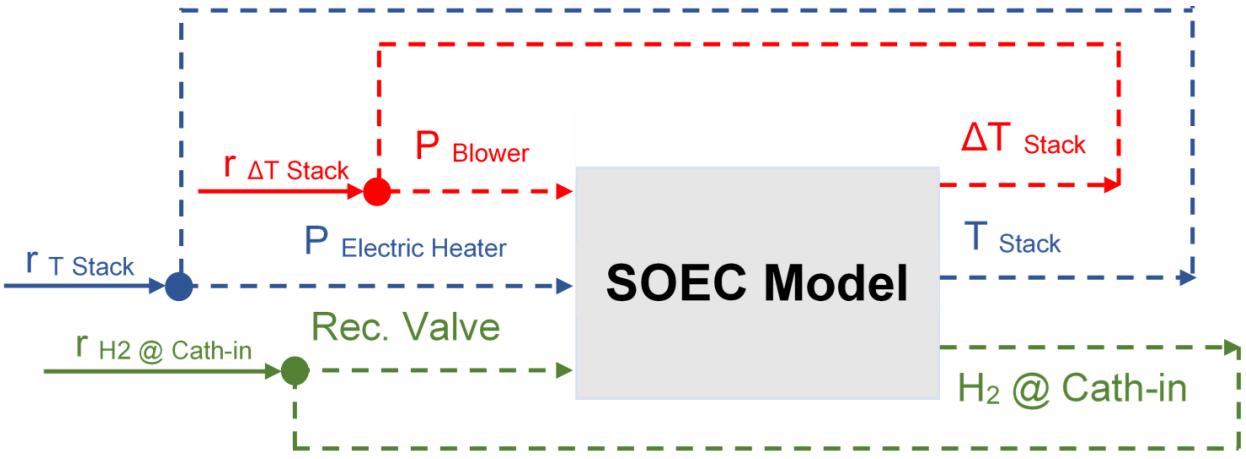

Figure 8: SOEC System Control Scheme [56]

At nominal design conditions (i.e., slightly endothermic operation with V_{cell}=1.25 V), the system is designed to maintain the stack average temperature with a small thermal energy input coming from the anode enthalpy flux. However, when solar irradiation is insufficient to provide the heat required, the stack operates substantially endothermically. Therefore, an electric heater is used to provide the required heat whenever required (e.g., at the beginning and end of daily operation on solar energy) to provide the required thermal energy for self-sustained operation [56].

3.3 CSP-Integrated SOEC System Performance Parameters

With the SOEC operating at constant steam utilization of 85%, the power consumed by the stack is varied in proportion to the steam flow rate. The required thermal energy for endothermic electrochemical reaction comes from the CSP plant, while the required electrical power for electrochemical reaction is supplied by electricity produced from a PV solar farm. High-temperature steam is produced by exchanging heat with the hot salt that absorbs solar thermal energy in the solar tower receiver.

SOEC stack and system electrical efficiencies are defined based upon the ratio of a lower heating value (LHV) of the produced hydrogen to the power consumed by the stack, and by the system, respectively, as shown below

$$\eta_i = \frac{\dot{n}_{H_2} \times LHV_{H_2}}{P_i} \qquad i = Stack, System \tag{33}$$

where, $\dot{n}_{H_2}$ is the molar flow rate of hydrogen, LHV_{H_2} is the lower heating value of hydrogen, and P is the power consumed. The thermodynamic 1st law mixed efficiency of

the integrated systems is defined as (34) to assess the efficiency of the integrated system by including the thermal power produced from the CSP plant

$$\eta_{mixed} = \frac{\dot{n}_{H_2} \times LHV_{H_2}}{P_{system} + P_{thermal}} \tag{34}$$

where $P_{system}, and\ P_{thermal}$ is the power consumed by system and power produced from the CSP plant, respectively.

3.4 CSP-Integrated Cement Plant

The CSP plant is integrated with a cement plant by placing a solar reactor on top of a solar tower where heat is supplied by concentrated solar energy. Figure 9 shows the CSP-integrated cement plant that is conceptualized which is based on the study done by Moumin et al. [51] and is further developed in this work. The integrated plant operates in hybrid mode, operating both as a conventional and solar-integrated cement plant depending on solar availability. When the plant operates as a conventional, coal-fired cement plant, the raw meal enters the preheater then is fed to the calciner. The calcined meal goes to the rotary kiln where it gets sintered. When the plant operates as a solar-thermal cement plant, the preheated raw meal is fed to the solar calciner which is located at the top of the solar tower. The required heat for calcination is provided by concentrated solar energy. If the absorbed solar thermal energy is greater than that of the design thermal energy, the calcined meal is fed to both the rotary kiln for sintering and to the thermal storage tank. If the solar calciner cannot provide sufficient calcined meal for continuous rotary kiln operation, the calcined meal is additionally supplied from the thermal storage.

In the case of depleted thermal storage, additional calcined meal is supplied by the coal-fired calciner.

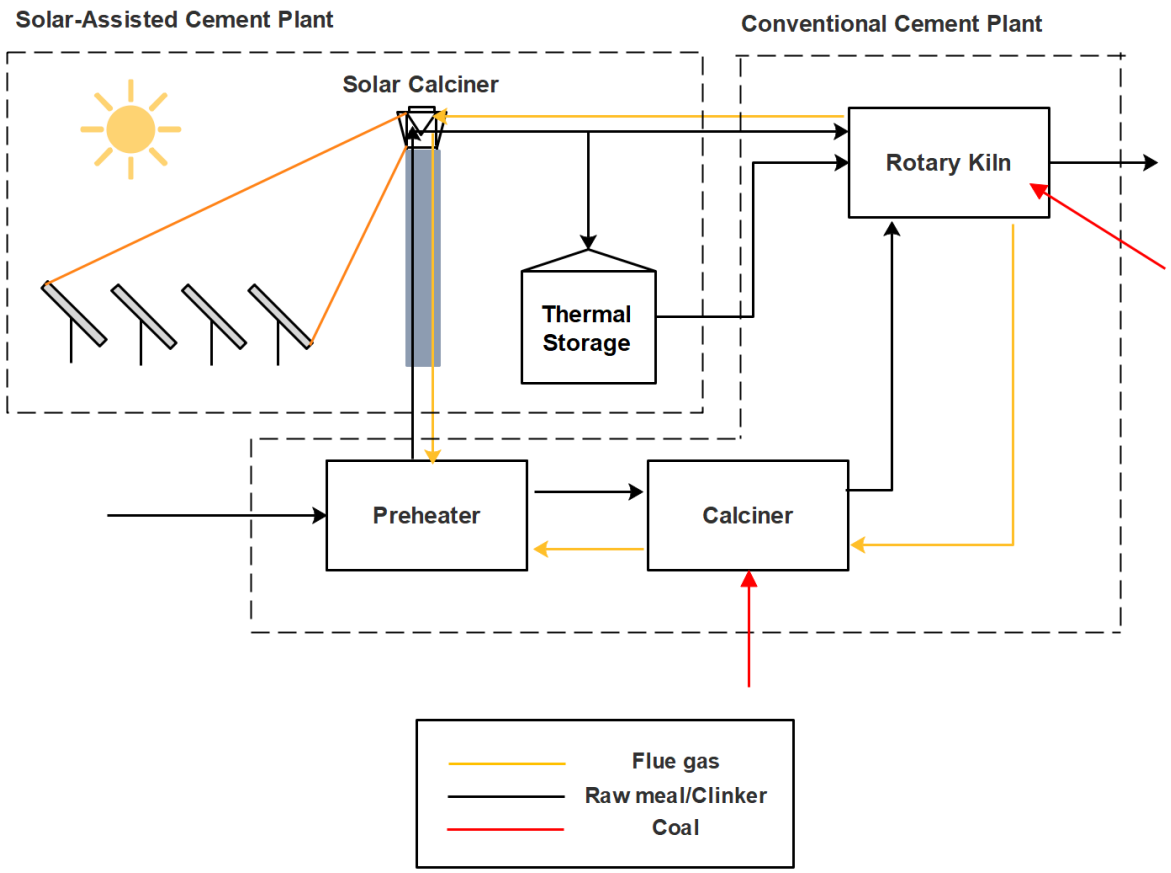

Figure 9: CSP-integrated Cement Plant Layout (design after [51])

The study relies on the Best Available Technique (BAT) standard as defined in the European BREF-Document (Best Available Technique Reference) for manufacturing cement [61]. The reference plant consists of a preheater, calciner, rotary kiln, and grate cooler. The schematic of the reference plant is shown in Figure 10. SINTEF Energy Research (SINTEF-ER), an independent research organization based in Europe, together with the Polytechnic University of Milan (PoliMi), developed a model of the reference

cement kiln [62], [63]. The details of the model are shown in Table 4. Based on the inputs and outputs provided by the work of SINTEF-ER and PoliMi, the energy balance pertinent to this study is applied for the solar calciner.

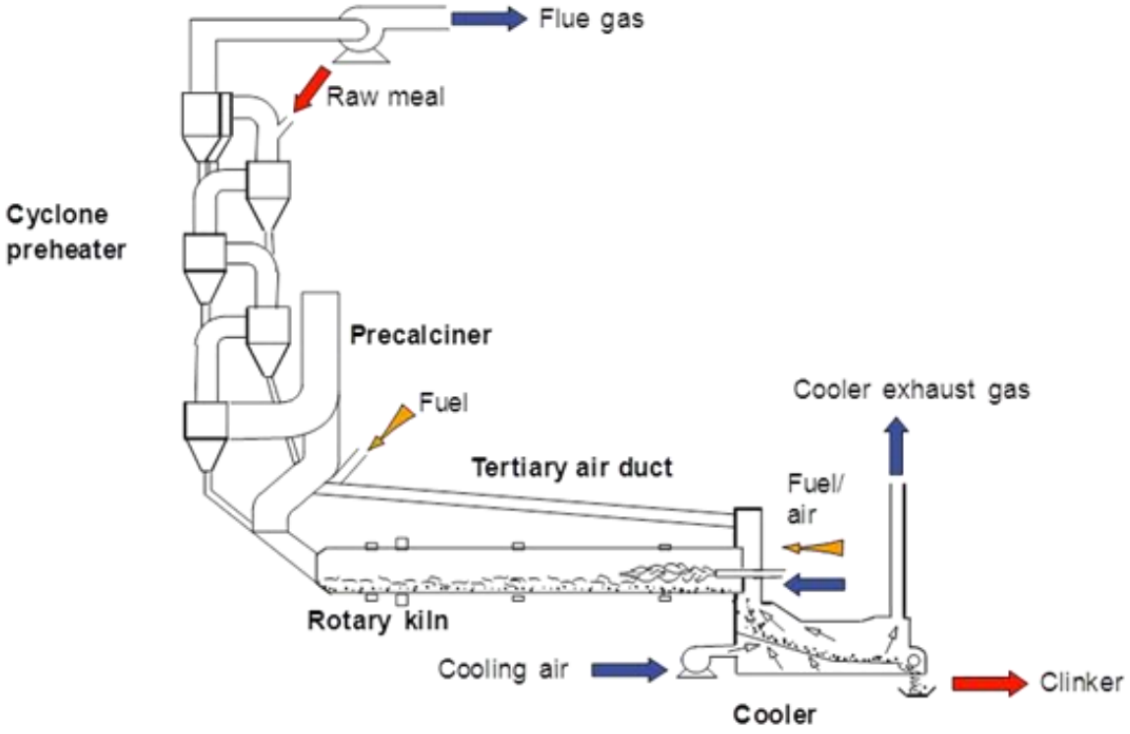

Figure 10: Reference Cement Plant Schematic

Source: Adapted from [62]

Table 4: Reference Cement Plant Details [62], [63]

Parameter	Description	Value	Unit
$\dot{m}_{KG}$	Kiln gas mass flow	17.1	kg/s
$\dot{m}_{TA}$	Tertiary air flow	26.2	kg/s
$\dot{m}_{clinker}$	Clinker mass flow	34.72	kg/s
$\dot{m}_{coal,calcin}$	Coal mass flow into calciner	2.4	kg/s
$\dot{m}_{coal,klin}$	Coal mass flow into clinkering kiln	1.469	kg/s
$\dot{m}_{rm}/\dot{m}_{clinker}$	Raw-meal-to-clinker ratio	1.6	-
T_{calcin}	Calcination temperature	900	°C
$T_{in,KG}$	Kiln gas temperature at inlet	1078	°C
$T_{in,TA}$	Temperature of tertiary air at inlet	1050	°C
$T_{in,rm}$	Raw meal temperature at inlet	759	°C
$T_{out,g}$	Gas temperature at caciner exit	871	°C
X_{in}^{dc}	Degree of calcination at calciner inlet	0.18	-
X_{out}^{dc}	Degree of calcination at calciner exit	0.95	-
Y_{rm,CO_2}	Mass fraction of CO_2 in the raw meal	0.3474	-
$Y_{rm,CaO}$	Mass fraction of CaO in raw meal	0.4322	-
c_{CO_2}	Specific CO_2 emission for coal	9.465×10^{-5}	kg/kJ
ΔH_{CaO}^{calcin}	Calcination enthalpy at 900°C, 1 atm	3182	kJ/kg
LHV_{coal}	Low heating value of coal	27150	kJ/kg

3.5 Mass and Heat Balance of the Solar Calciner

To determine the amount of CO_2 reduced by using the solar calciner, mass and heat balances must be analyzed. Figure 11 shows a detailed mass and energy balance of the solar calciner where the configuration is derived from the reference cement plant described in the prior section. To obtain the heat absorbed for the solar calciner, SAM is utilized to get a specific DNI profile, heliostat field layout, and field efficiency for the locations investigated. The optimization tool embedded in SAM generated the optimal number and layout of the heliostats as well as the height and radius of the solar tower. Unlike the study done by Moumin et al. [51] where the solar thermal efficiency is a set parameter, this work obtained the efficiency based upon the dynamic mass and energy balances that included heat losses as described in section **Error! Reference source not found.**

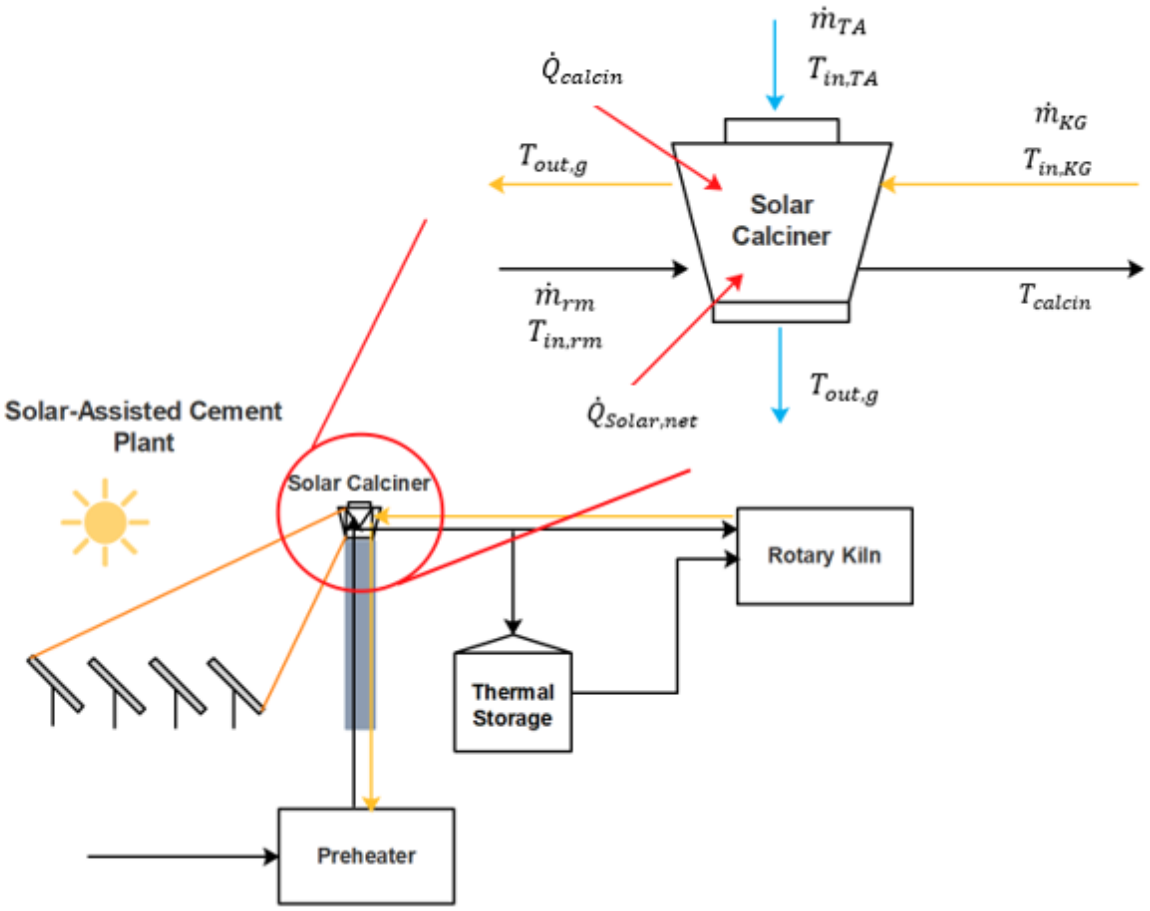

Figure 11: Mass and Heat Balance of the Solar Calciner Concept

The overall heat balance for the solar calciner is described in the following equation. The equations are adapted from the work of Moumin et al. [51]

$$\dot{Q}_{Solar,net} = \dot{Q}_{rm} + \dot{Q}_{calcin} + \dot{Q}_{TA} + \dot{Q}_{KG} \quad (35)$$

$$\dot{Q}_{rm} = \dot{m}_{rm} C_{p,rm} (T_{calcin} - T_{in,rm}) \quad (36)$$

$$\dot{Q}_{TA} = \dot{m}_{TA} C_{p,TA} (T_{out,g} - T_{in,TA}) \quad (37)$$

$$\dot{Q}_{KG} = \dot{m}_{KG} C_{p,KG} (T_{out,g} - T_{in,KG}) \quad (38)$$

$$\dot{Q}_{calcin} = \dot{m}_{rm} Y_{rm,CaO} \left(X_{out}^{dc} - X_{in}^{dc}\right) \times \Delta H_{CaO}^{calcin} \quad (39)$$

where $\dot{Q}_{TA}$, and $\dot{Q}_{KG}$ are the heat input by the tertiary air (TA) and kiln gas (KG), respectively. $\dot{Q}_{Solar,net}$, is the net heat absorbed in the solar calciner, $\dot{Q}_{rm}$ is the heat required for heating up the raw meal (rm) from the raw meal inlet temperature, $T_{in,rm}$, to calcination temperature, T_{calcin}. $\dot{Q}_{calcin}$ is the heat required for the calcination. $Y_{rm,CaO}$ is the relative calcium oxide content, ΔH_{CaO}^{calcin} is the specific calcination energy, and X_{out}^{dc} and X_{in}^{dc} are the degree of calcination at the inlet and outlet of the solar calciner, respectively. $\dot{m}$ and C_p are the mass flowrate and specific heat, respectively.

Inserting the parametric data provided in Table 4 into the equations above, the net heat absorbed by the solar calciner is found. From the energy balances, it is found that $\dot{Q}_{calcin} \approx \dot{Q}_{Solar,net}$. In the previous study, with a solar multiple of three, the nominal thermal power of the solar calciner was three times greater than that of the reference plant. In the current work, the condition of $\dot{Q}_{calcin} \approx \dot{Q}_{Solar,net}$ is assumed to be consistent for the solar calciner regardless of its operating conditions and capacity. The net solar thermal energy is used in SAM as cycle thermal power for designing CSP plant components as such the solar tower and heliostat field to be integrated to the reference cement plant.

3.6 Reduction of CO_2 Emissions from the Solar-Thermal Cement Plant

The maximum CO_2 emissions reduction derivation from Moumin et al. [51] is used to estimate potential CO_2 emissions reduction at each site investigated in the current work. The maximum CO_2 emissions reduction can be estimated by calculating the emissions

produced by the solar calciner and the emissions coming from the conventional calciner. The CO_2 emissions coming from the solar calciner, $\dot{m}_{CO_2,sol}$, are calculated by accounting for the emissions coming from the raw meal during calcination in addition to pyro-processing of coal in the rotary kiln

$$\dot{m}_{CO_2,sol} = Y_{rm,CO_2}\dot{m}_{rm} + \dot{m}_{coal,kiln}LHV_{coal}c_{CO_2} \tag{40}$$

where is Y_{rm,CO_2} is the CO_2 content in the raw meal, c_{CO_2} is the specific CO_2 emission factor per unit of heat content of the fuel, and $\dot{m}_{rm}$ and $\dot{m}_{coal,kiln}$ are the mass flowrate of the raw meal and coal used in the kiln, respectively.

The emissions from the conventional calciner, $\dot{m}_{CO_2,conv}$, are determined similar to how the emissions are determined for the solar calciner but adding the emissions produced from burning coal during calcination

$$\dot{m}_{CO_2,conv} = Y_{rm,CO_2}\dot{m}_{rm} + \dot{m}_{coal,kiln}LHV_{coal}c_{CO_2} + \dot{m}_{coal,calcin}LHV_{coal}c_{CO_2} \tag{41}$$

where $\dot{m}_{coal,calcin}$ is the mass flowrate of coal needed for the calciner operation.

Therefore, assuming that all of the chemical energy from the coal used in the calciner is replaced by solar thermal energy or a solarization rate of 100%, the maximum reduction in the emissions, $\dot{m}_{CO_2,max,redux}$, is found below.

$$\dot{m}_{CO_2,max,redux} = \dot{m}_{CO_2,conv} - \dot{m}_{CO_2,sol} \tag{42}$$

$$\dot{m}_{CO_2,max,redux} = \dot{m}_{coal,calcin} LHV_{coal} c_{CO_2} \quad (43)$$

Using the equations and the data from Table 4, $\dot{m}_{CO_2,sol}$, $\dot{m}_{CO_2,conv}$, and $\dot{m}_{CO_2,max,redux}$ are found which are 23.07 kg/s, 29.24 kg/s, and 6.167 kg/s, respectively. Therefore, in the case of 100% solarization rate, integrating the solar calciner into the conventional cement plant could reduce the CO_2 emissions by approximately 21%.

3.7 Cement Thermal Storage

Cement thermal storage is modeled to be integrated with the solar calciner and the conventional coal-fired cement plant. As depicted in Figure 9, all of the calcined meal is fed to the kiln for sintering if the solar multiple is set as one. However, if the solar multiple is chosen to be greater than one, the solar calciner generates excess meal which is stored in the storage for later use when the deficit between the produced calcined meal and the design point occurs or when solar is not available. Setting a solar multiple greater one and implementing thermal storage significantly increases the solarization rate which ultimately reduces the CO_2 emissions. The logic of the storage model is described from Eqs. (44) – (52). Referencing the reference plant described previously, every component of the conventional cement plant is assumed to be operating at a steady-state with thermal power of 58MW. Therefore, the design point is set at 58MW.

Case 1: The stored amount of clinker is greater than the design point for continuous operation.

In this case, the required amount of clinker is sent to the kiln from the storage for continuous operation of the plant. If the storage does not reach its maximum capacity, the production of clinker is not curtailed

$$dm_{stored} = (\dot{m}_{calcin} - \dot{m}_{design\ point})dt \tag{44}$$

$$m_{curtail} = 0 \tag{45}$$

where m_{stored} is the amount of stored clinker, $\dot{m}_{calcin}$ is mass flowrate of calcined clinker coming from the solar calciner, $\dot{m}_{design\ point}$ is the required mass flowrate of calcined clinker for continuous operation of the kiln, and $m_{curtail}$ is the amount of curtailed clinker.

If the amount of calcined meal sent to the storage is greater than the available capacity, then the storage reaches its full capacity, and the excess meal is curtailed. m_{cap} is the maximum amount of clinker stored when the storage reaches its full capacity.

$$m_{stored} = m_{cap} \tag{46}$$

$$m_{curtail} = \dot{m}_{calcin}dt - (m_{cap} - m_{stored,prev}) \tag{47}$$

Case 2: The stored amount of clinker is less than the design point for continuous operation.

In such a scenario, a coal-fired calciner is used to supply the required amount of clinker where m_{peaker} is the amount of clinker coming from the coal-fired calciner.

$$m_{peaker} = \dot{m}_{design\ point}dt \tag{48}$$

Same as Case 1, if the amount of calcined meal sent to the storage is greater than the available capacity, then the storage reaches its full capacity, and the excess clinker is curtailed.

$$m_{stored} = m_{cap} \tag{49}$$

$$m_{curtail} = \dot{m}_{calcin} dt - (m_{cap} - m_{stored,prev}) \tag{50}$$

If the amount of calcined meal sent to the storage is less than the available capacity, then all calcined meal from the solar calciner goes to the storage because the required amount of clinker is fed from a coal-fired calciner. Again, none of the clinker is curtailed.

$$dm_{stored} = \dot{m}_{calcin} dt \tag{51}$$

$$m_{curtail} = 0 \tag{52}$$

To model the thermal losses associated with the storage, the heat transfer between the storage tank and ambient is considered. To simplify the model calculation, only free convection is considered in this work, and the heat flux is considered one directional. The most important dimensionless parameter for estimating heat losses from free convection is the Rayleigh number, Ra_L, which is shown below:

$$Ra_L = \frac{g\beta(T_s - T_{amb})L^3}{\nu_{air}\alpha_{air}} \tag{53}$$

where g is the gravitational acceleration and L is the length. The kinematic viscosity, ν_{air}, and thermal diffusivity of air, α_{air}, is evaluated at the film temperature T_f [60], [64]:

$$T_f = \frac{T_s + T_{amb}}{2} \tag{54}$$

The thermal expansion coefficient, β, can be approximated by the following.

$$\beta = \frac{1}{T_f} \tag{55}$$

Another dimensionless parameter used is the Nusselt number, and Churchill and Chu correlation is used specifically for vertical plate configuration which is applicable for the storage tank which is cylindrical.

$$\overline{Nu}_{lateral} = \frac{\overline{h}L}{k_f} = \{0.825 + \frac{0.387 \times Ra_L^{\frac{1}{6}}}{\left[1 + \left(\frac{0.492}{Pr}\right)^{\frac{9}{16}}\right]^{\frac{8}{27}}}\}^2 \tag{56}$$

The correlation can be applied to vertical cylinders if the boundary layer thickness is much less than the diameter of the cylinder [60]. Such condition is satisfied by the following:

$$\frac{D}{L} \geq \frac{35}{Gr_L^{\frac{1}{4}}} \tag{57}$$

where D and L are the diameter and length of the cylinder, and Gr is the Grashof number.

To find the Nusselt number for the upper horizontal plate, $\overline{Nu}_{top}$, the following correlation is used.

$$\overline{Nu_{top}} = 0.54 \times Ra_L^{\frac{1}{4}} \tag{58}$$

The average heat transfer coefficient, h_{ave}, is defined as:

$$\overline{h}_{ave} = \frac{A_{s,lateral} \times \overline{h}_{lateral} + A_{s,top} \times \overline{h}_{top}}{A_{s,lateral} + A_{s,top}} \tag{59}$$

The overall heat transfer coefficient, U, between the calcined meal and ambient air can be evaluated with the following:

$$UA = (R_{cond} + R_{conv})^{-1} \tag{60}$$

$$R_{cond} = \frac{\ln\left(\frac{r_2}{r_1}\right)}{2\pi L k_w} \tag{61}$$

$$R_{conv} = \frac{1}{\overline{h}_{ave} A_{ext}} \tag{62}$$

where r_2 and r_1 are the outer and inner radius of the storage tank, k_w is the thermal conductivity of the insulating wall, and A_{ext} is the external area.

Consequently, the heat loss is defined as:

$$\dot{Q}_{loss} = UA \times (T_{clk} - T_{amb}) \tag{63}$$

The temperature of stored clinker, T_{clk}, is calculated with the following equation:

$$\rho_{clk} C_{p,clk} V_{clk} \frac{dT_{clk}}{dt} = \dot{H}_{clk,in} - \dot{H}_{clk,out} - \dot{Q}_{loss} \quad (64)$$

where ρ_{clk}, $C_{p,clk}$, and V_{clk} are the density, heat capacity, and volume of clinker, respectively. $\dot{H}_{clk,in}$ and $\dot{H}_{clk,out}$ are the clinker inlet and outlet enthalpy, respectively.

The detail of the storage is shown in the table below:

Table 5: Cement Storage Parameters

Parameter	**Description**	**Value**	**Unit**
$C_{p,clk}$	Heat Capacity of Clinker [51]	$0.8 + 0.000297 \times (T - 273)$	kJ/kg-K
T_{amb}	Ambient Temperature	20	°C
T_{calcin}	Calcined Meal Temperature	900	°C
T_{surf}	Surface Temperature	40	°C
k_w	Thermal Conductivity of the Wall [65]	0.04	W/m-K
ρ_{clk}	Density of Clinker	1415	kg/m^2
H	Height	7.5	m
r	Radius	7.5	m
V	Volume	1325	m^3

3.8 CSP-Integrated Cement Plant Performance Parameter

A conventional coal-fired cement plant operates continuously to produce clinker at a constant rate. The CSP-Integrated cement plant is also assumed to be operating continuously with a constant clinker production rate. Unlike the conventional plant, the integrated plant has an option to utilize solar thermal energy for calcination. When insufficient solar thermal energy is present, the integrated plant is assumed to be operating like the conventional plant to maintain a constant rate of production. Therefore, to evaluate the degree of solarization, percent solarization, P_{Sol}, at each location is calculated which is derived below [51]:

$$P_{Sol} = \frac{8760 - \frac{\sum(\dot{Q}_{conv} + \dot{Q}_{elec})}{\dot{Q}_{ref,full}}}{8760} \times 100 \tag{65}$$

$$\dot{Q}_{ref,full} = 62.5\ MW \tag{66}$$

$\dot{Q}_{ref,full}$ is the amount of thermal power used in the coal-fired calciner for the reference cement plant. Percent solarization of 100% means that the integrated plant garnered sufficient solar thermal energy for the plant to operate without utilizing coal. Percent solarization is further used to estimate the CO_2 reduction and the saved amount of coal, $m_{coal,save}$, from the integration which are shown through Eqs (67)-(69)

$$P_{CO_2,redux} = 0.21 \times P_{Sol} \tag{67}$$

$$Q_{saved} = \dot{Q}_{ref,full} \times P_{Sol} \times (\frac{8670}{100}) \tag{68}$$

$$m_{coal,save} = \frac{Q_{saved} \times 10^3}{LHV_{coal}} * 3600 \quad (69)$$

where $P_{CO_2,redux}$ is the percent reduction of the total CO_2 emissions. As mentioned previously, in the case of 100% solarization rate, integrating the solar calciner into the conventional cement plant could reduce the CO_2 emissions by approximately 21%. Therefore, 0.21 is multiplied by P_{Sol} in Eq (67) to calculate $P_{CO_2,redux}$.

3.9 Cost Analysis of CSP-Integrated Cement Plant

The cost estimation is performed which consists of two main parts: 1) the capital expenditure (CAPEX) and 2) operating expenditure (OPEX). The costs of heliostats, solar tower, solar calciner, thermal storage, contingency, and other indirect costs are estimated based on the assumptions which are summarized in where COC and COC_{ref} are the costs of clinker and the costs of clinker for the reference plant, respectively. $\left(\frac{t_{CO_2}}{t_{clk}}\right)_{clk,eq,ref}$ and $\left(\frac{t_{CO_2}}{t_{clk}}\right)_{clk,eq}$ are the specific equivalent emissions from the reference cement plant and the specific equivalent emissions from the cement plant with capture, respectively.

Table *6*. To calculate the CO_2 avoided costs, the costs of clinker and equivalent specific CO_2 emissions with and without carbon capture technology are considered. The costs of clinker with carbon capture are estimated based on the annualized CAPEX and OPEX and the annual production of clinker. The costs of clinker without carbon capture (the reference cement plant) are given from the work of Gardarsdottir et al. [54]. The CO_2 avoided costs (CAC) are evaluated with the following equation

$$CAC = \frac{COC - COC_{ref}}{\left(\frac{t_{CO_2}}{t_{clk}}\right)_{clk,eq,ref} - \left(\frac{t_{CO_2}}{t_{clk}}\right)_{clk,eq}} \quad (70)$$

where COC and COC_{ref} are the costs of clinker and the costs of clinker for the reference plant, respectively. $\left(\frac{t_{CO_2}}{t_{clk}}\right)_{clk,eq,ref}$ and $\left(\frac{t_{CO_2}}{t_{clk}}\right)_{clk,eq}$ are the specific equivalent emissions from the reference cement plant and the specific equivalent emissions from the cement plant with capture, respectively.

Table 6: CAPEX and OPEX Assumptions

Paameter	**Assumption**	**Source**
Direct Capital Costs		
Site Improvement Costs	16 USD/m^2	[57]
Heliostat Field Costs	140 USD/m^2	[57]
Fixed Tower Costs	3,000,000 USD	[57]
Tower Cost Scaling Exponent	0.0113	[57]
Solar Calciner Costs	$450{,}288 \times \left(\frac{\dot{Q}_{solar,net}}{293{,}000}\right)^{0.48}$ USD	[51]
Thermal Storage Costs	9.9 USD/kWh	[51]
Contingency Costs	7% of subtotal of the above	[57]
Indirect Capital Costs		
Total Land Costs	10,000 USD/Acre	[57]
EPC and Owner Costs	13% of direct capital cost	[57]
Sales Tax Basis	80% of direct capital cost	[57]
Sales Tax Rate	0.05%	[57]
Operating Costs		
Operation and Maintaince Costs	2% of CAPEX	[51]
Fuel Savings	$m_{coal,save} \times Coal\ Costs$	[51]
Coal Costs	65 USD/t_{coal}	[66]

4 Results

4.1 Design Operating Conditions

Table 7 presents the steady-state operating conditions of the integrated system (nominal design conditions) as presented in Figure *5*. The SOEC system is nominally designed at slightly endothermic operating mode (operating voltage is slightly smaller than thermoneutral voltage) to have stack efficiency greater than 100% while the electric heater consumes negligible amount of electricity compared to the required electricity for electrochemical reaction in the SOEC stack. The CSP plant has the nominal thermal output of 20 MW_{th}.

Table 7: Integrated System Nominal Operating Conditions (Design Conditions)

Stream	Temperature (K)	Flow Rate (kg/s)	Composition
1	700	39.9	KCl-$MgCl_2$
2	1200	39.9	KCl-$MgCl_2$
3	298	4.78	100% H_2O
4	1150	4.78	100% H_2O
5	1139	4.94	90% H_2O-10% H_2
6	1024	1.32	85% H_2-15% H_2O
7	1024	1.17	85% H_2-15% H_2O
8	1024	0.15	85% H_2-15% H_2O
9 & 10	298	8.12	79% N_2-21% O_2
11	1009	8.12	79% N_2-21% O_2
12	1123	8.12	79% N_2-21% O_2
13	1023	11.7	55% N_2-45% O_2
14	525	11.7	55% N_2-45% O_2

4.2 CSP Plant Dynamic Operation

The thermal power collected from the CSP plant for a typical sunny day in winter between 8 AM and 3 PM is directly and entirely given to the SOEC stack for renewable hydrogen production. As shown in Figure 12, the salt mass flow rate is directly proportional to the DNI profile. The flow rate varies between 15–40 kg s^{-1} and reaches the

maximum around 11:30 AM as the DNI reaches its maximum at 11 AM. The salt temperature at the outlet of the solar receiver is actively controlled at 1200 K.

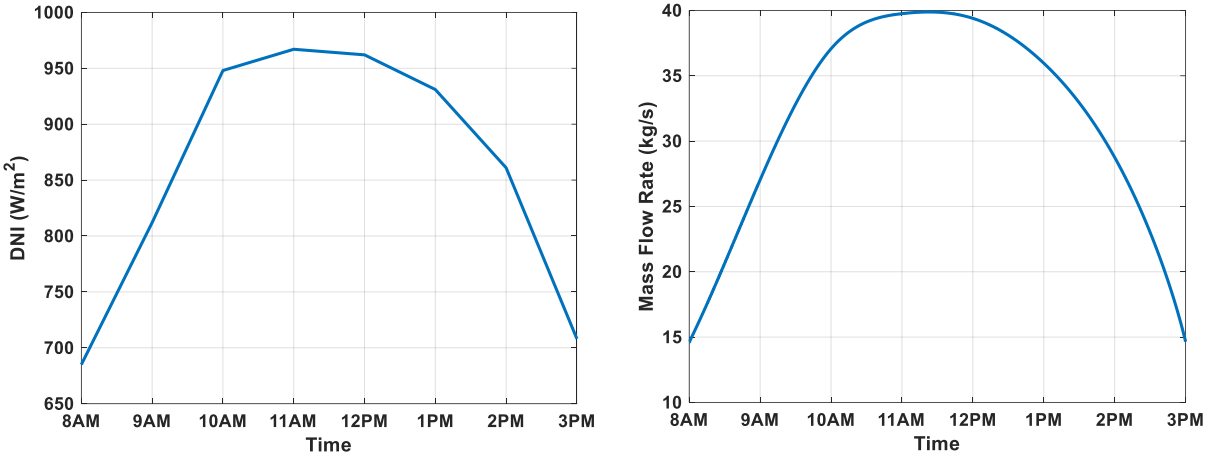

Figure 12: (left) DNI Profile of a Typical Sunny Day in Winter, (right) Salt Mass Flow Rate to the Solar Receiver

Since the hot salt does not get stored during the operation in the default design the steam generation is also proportional to the DNI profile. The hot salt is completely utilized to produce high-temperature steam to be fed to the SOEC system. Figure 13 shows the steam flow rate and the temperature variation during operation. The steam flow rate varies from 1.8 kg s^{-1} to 4.78 kg s^{-1} where the maximum steam flow rate occurs at 11:30 AM.

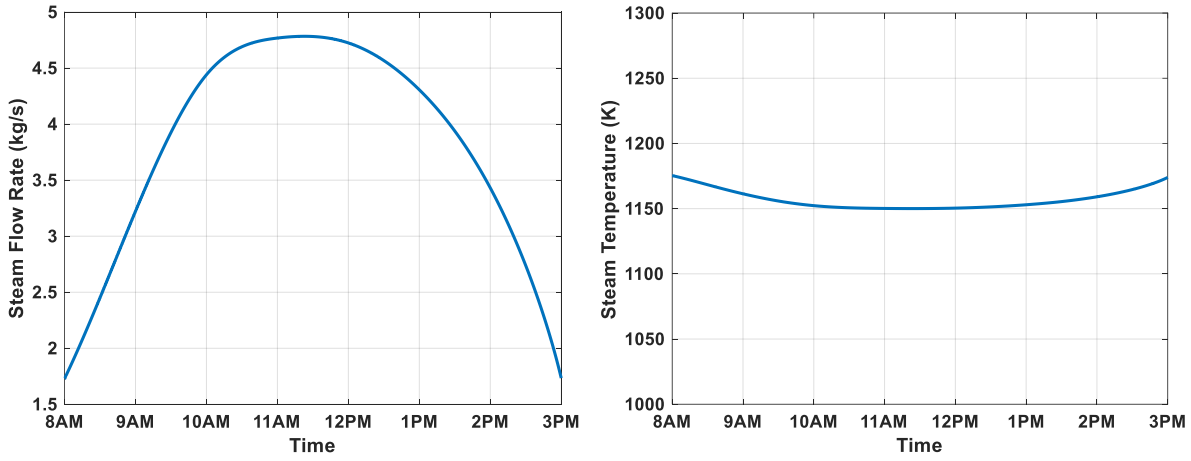

Figure 13: (left) Steam flow rate to the SOEC system, (right) Steam temperature during the operation

4.3 SOEC System Dynamic Operation

Figure 14 and Figure 15 show the mass flow rates and temperatures of the cathode streams, respectively. High-temperature steam produced from the CSP plant is mixed with the partially recirculated cathode outlet before entering the stack to obtain 10% molar fraction of hydrogen to prevent cathode material degradation. As a result of the mixing, the cathode inlet (stream #5) mass flow rate is slightly higher than the steam mass flow rate provided by the CSP plant. The cathode inlet temperature is reduced after mixing with the recirculated flow because of the lower cathode outlet temperature. The cathode outlet (stream #6) mass flow rate is substantially lower than that of the inlet as 85% of the steam is utilized to produce hydrogen. The cathode outlet temperature is maintained approximately at 1023 K during operation, to minimize the stack's temperature fluctuation, which ultimately prevents stack degradation. This constant cathode outlet temperature

results from controlling both the anode inlet temperature and anode stream spatial temperature gradient.

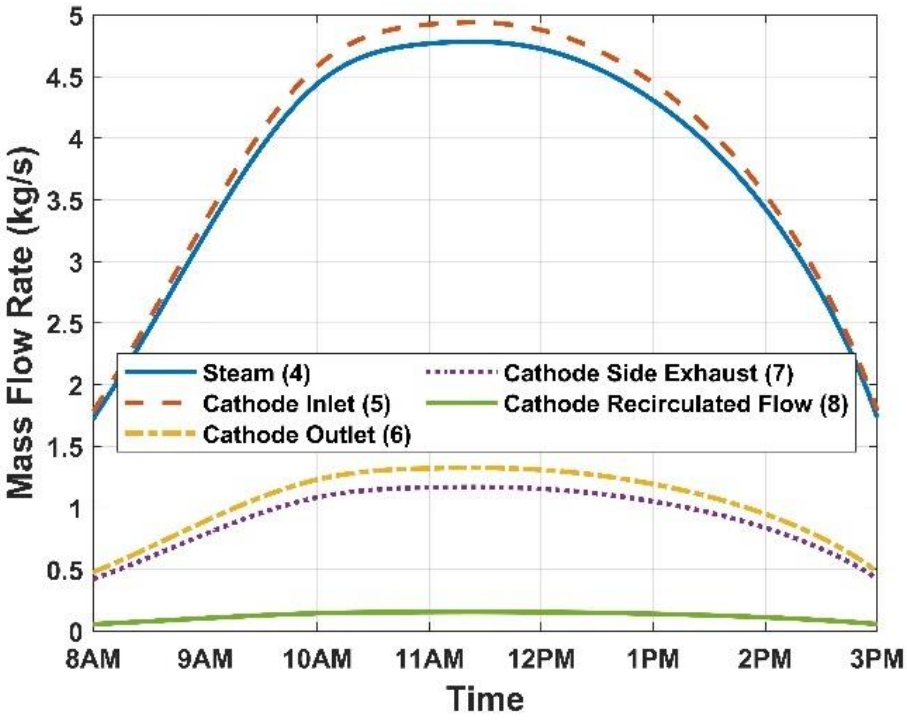

Figure 14: Mass Flow Rates of Cathode Side Streams

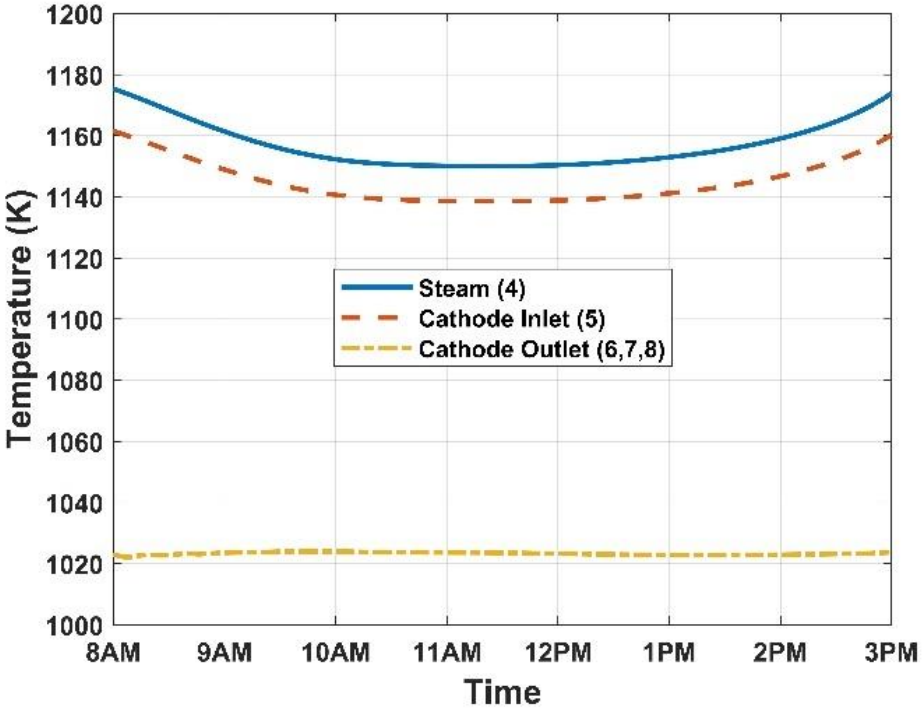

Figure 15: Temperatures of Cathode Side Streams

Figure 16 and Figure 17 depict the mass flow rates and temperatures of the anode stream, respectively. As shown in Figure *16*, the anode mass flow rate increases at the beginning of the operating window because the stack operates in a highly endothermic condition. With the electric heater additionally heating the air at 1123 K (setpoint), higher mass flow of air is necessary to provide sufficient thermal energy to the stack. The flow rate then decreases until 11:30 AM as the stack operates closer to the thermoneutral condition. Figure *17* shows the temperature variations of the anode stream. The anode outlet temperature (stream #13) is maintained at 1023 K, which again implies minimal fluctuation of the stack temperature. This proves the performance of the developed controller in keeping the anode inlet temperature (stream #12) at 1123 K and anode stream temperature difference at 100 K for the whole period of operation. For the

operating points close to the thermoneutral point (slightly endothermic), the heat exchanger cold outlet temperature reaches its maximum as lower air is required to thermally manage the stack. As a result, the balance of plant (BoP) power consumption, including blower electric power and electric heater electric power, is reduced from 11 AM to 12 PM.

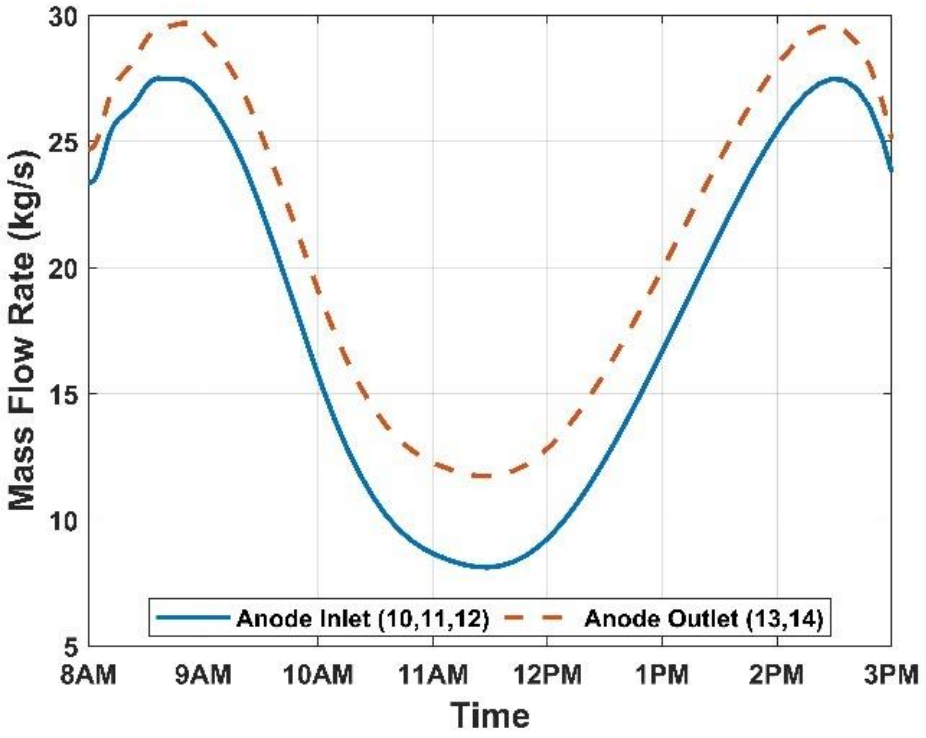

Figure 16: Mass Flow Rates of Anode Side Streams

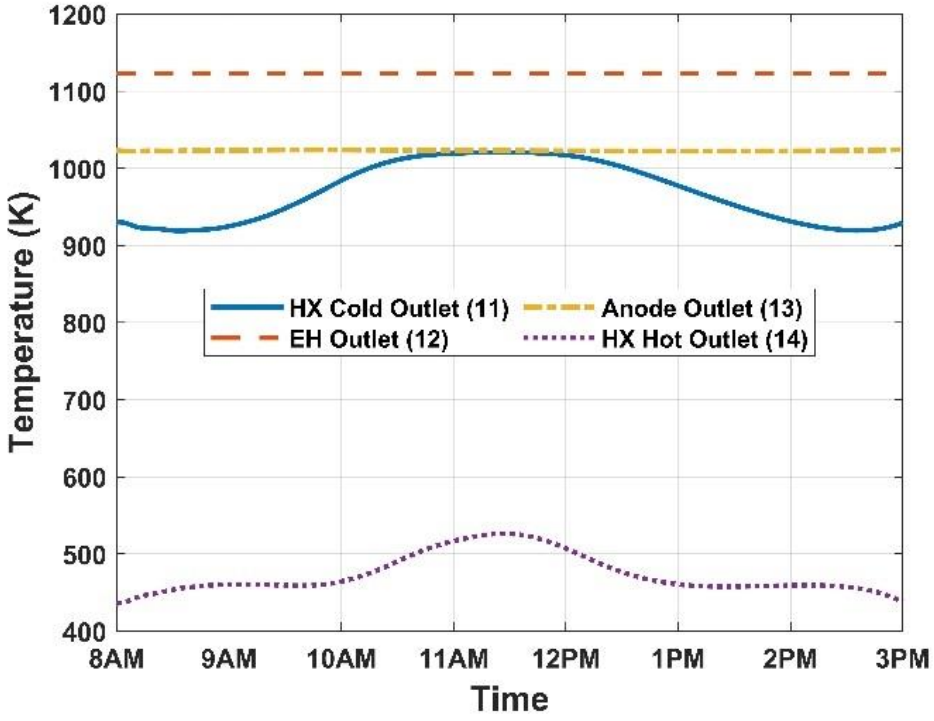

Figure 17: Temperatures of Anode Side Streams

Figure 18 highlights the performance of the system using previously defined performance parameters. The stack electrical efficiency, the system electrical efficiency and the thermodynamic 1st law mixed efficiency at nominal design conditions are 102.6%, 99.5%, and 72.6% respectively. The electrical efficiency of the integrated system is greater than 90% throughout the majority of the operating time. Such high electrical efficiency is achieved as a result of utilizing the thermal power from the CSP plant for high-temperature steam and reduced blower and heater electric power consumption. In particular, the electrical efficiency between 10 AM and 1 PM is nearly 100%. During this period, the stack operates slightly endothermically with the stack electrical efficiency greater than 100%. With the stack operating slightly endothermically, less heat is required for the electrolysis

which results in lower power consumption from the electric heater. As the stack operates highly endothermically or with high stack electrical efficiency more thermal energy is required for the electrolysis. Therefore, with a fixed steam utilization, higher blower and heater electric power consumption are necessary for thermal management of the system. The thermodynamic 1st law mixed efficiency is lower than the system electrical efficiency because the net thermal power collected by the solar receiver is considered in addition to the total electrical power consumed by the system. The mixed efficiency ranges between 66-72%, which is quite good, but which can be improved by further utilizing the waste heat coming out from the anode and cathode off-gas streams in a bottoming thermodynamic cycle.

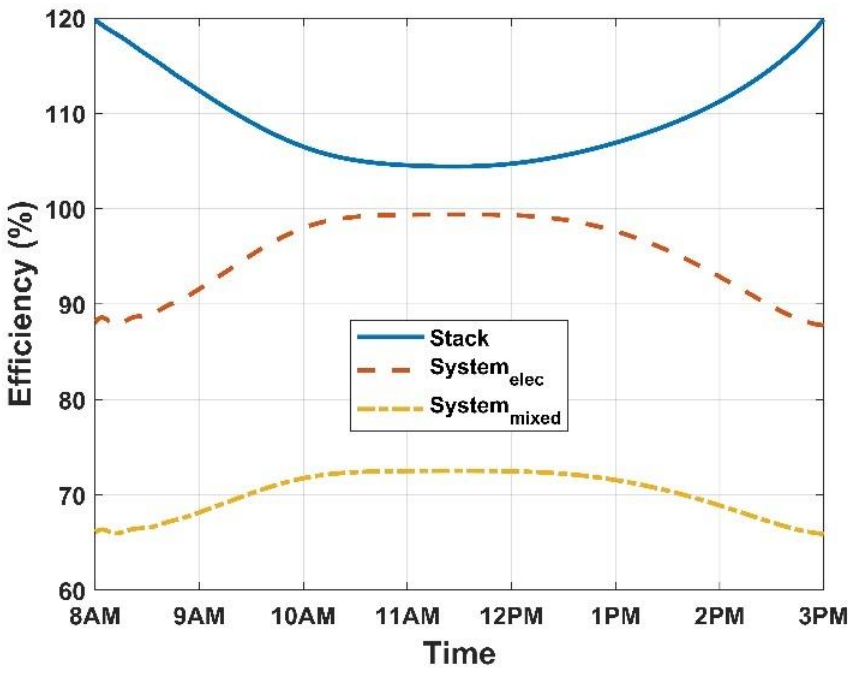

Figure 18: Stack Electrical Efficiency, System Electrical Efficiency, and Thermodynamic 1st Law System Mixed Efficiency

Figure 19 and Figure 20 show how the current density and hydrogen production vary throughout the day of operation, respectively. Both the current density and hydrogen production rate are proportional to the DNI profile (and steam flow rate profile) where the highest hydrogen production occurs around 11:30 AM with the highest system performance characteristics. Figure 20 shows the variations of the stack and CSP thermal power. The stack power is derived from the current density and operating voltage, and the CSP thermal power is derived from the net amount of thermal power harvested by the solar receiver. Throughout the operation time, 8 – 20 MW_{th} of thermal power is supplied to the SOEC system to produce high-temperature steam and to aid thermal management of the stack. With fixed steam utilization, the operating voltage varies in proportion to the current density. The operating voltage is always lower than the thermoneutral voltage resulting in stack efficiency higher than 100% for the whole period of operation.

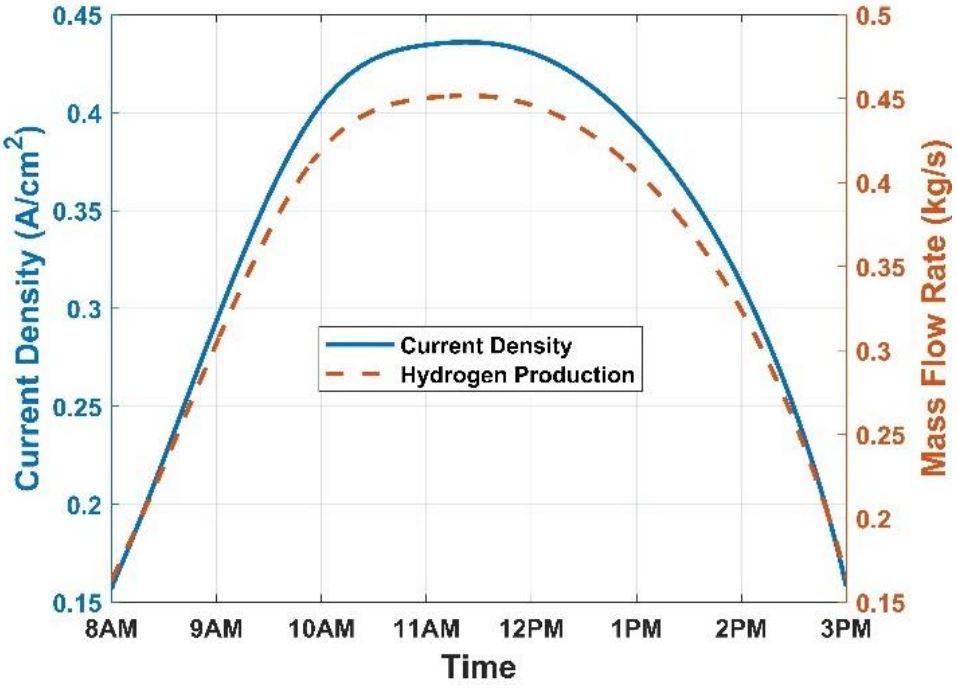

Figure 19: Current Density and Hydrogen Production Rate

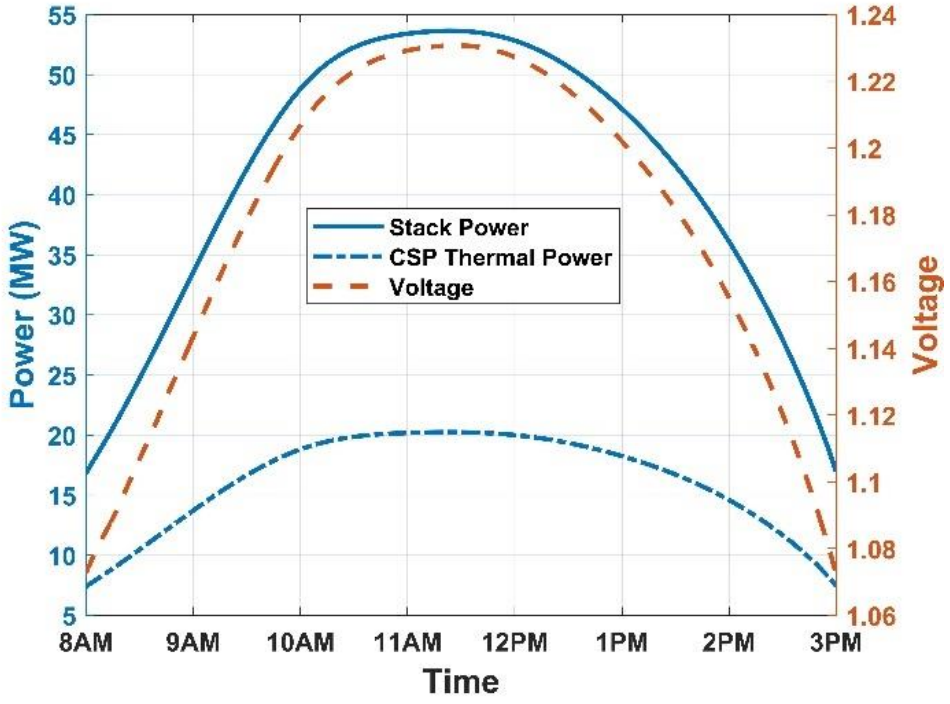

Figure 20: Stack Electric Power Consumption, CSP Thermal Power and Operating Voltage

4.4 Selected CSP-Integrated Cement Plant Locations

To evaluate the performance characteristics of CSP-integrated cement plant, five regions with distinct DNI potentials are selected across the United States, covering regions of low, medium, and high DNI potentials. A CSP-integrated cement plant is conceptualized at the selected regions, specifically where actual coal-fired cement plants are located. The current study looked at two sites in California, and one site each in Texas, Alabama, and Pennsylvania. As shown in Figure 21, the five sites have a wide range of DNI potentials, ranging from 8 kWh/m^2/day (2900 kWh/ m^2/ year) to 4.5 kWh/m^2/day (1600 kWh/ m^2/ year) which covers the range of DNI potential across the United States. Two sites in California have the highest and the second-highest DNI potential while the site in

Pennsylvania has the lowest DNI potential. Studying the performance characteristics of CSP-integrated cement plants in these locations should provide a full spectrum of techno-economic assessment of CSP-integrated cement plants across the United States.

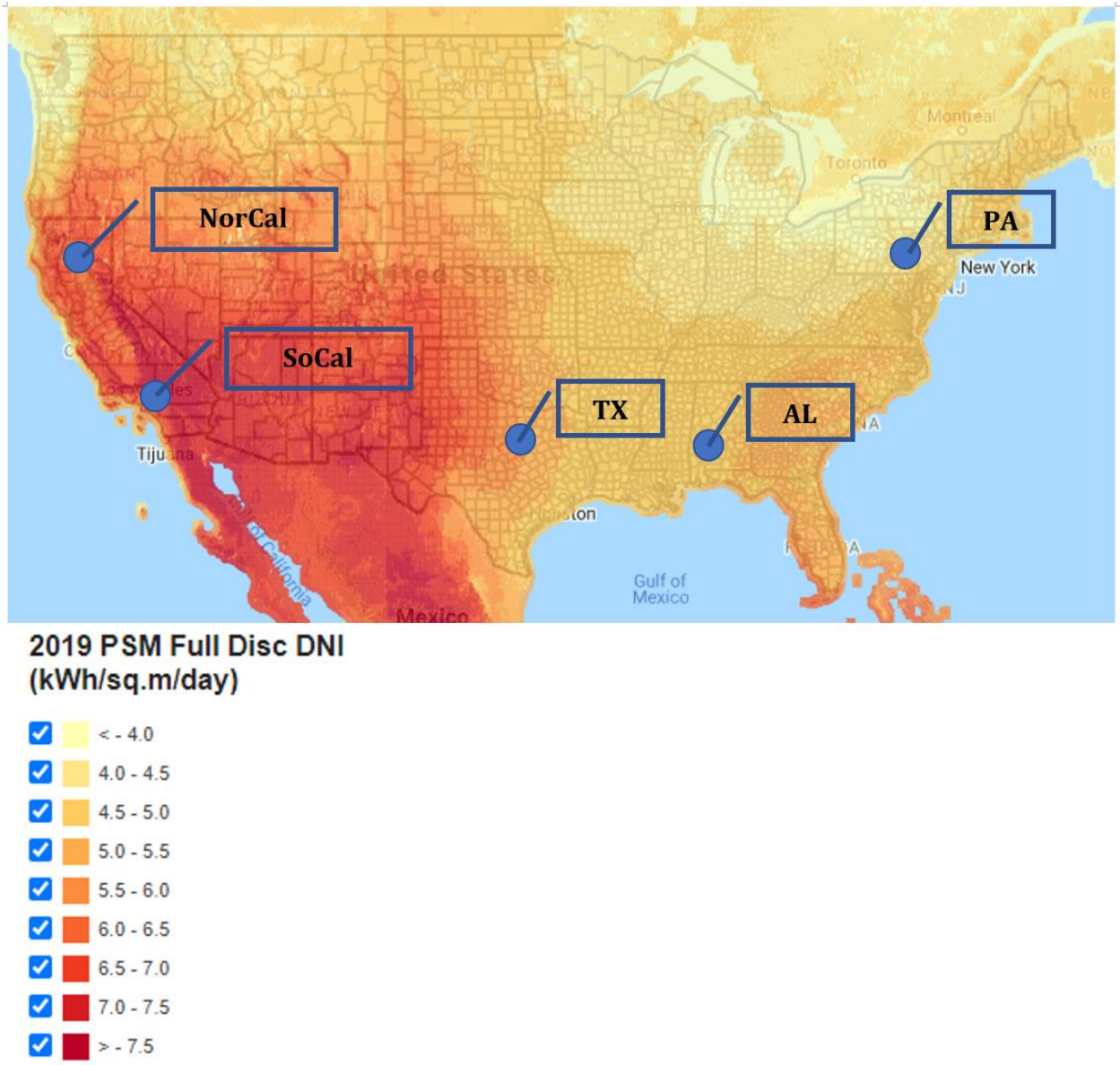

Figure 21: Locations of CSP Integrated Cement Plant [67]

4.5 Design Operating Conditions of CSP-Integrated Cement Plant

Because the reference cement is applied at each location, the operating conditions for all five CSP-integrated plants associated with the reference plant are identical, and the details are listed in Table *4*Table *5*. By applying the same operating conditions, the heat absorbed in the solar calciner, which dictates the performance characteristics such as the solarization rate and CO_2 emissions reduction, can be compared at each location. The solar tower and the heliostat field, however, are designed differently based on the solar multiple and the design point DNI. The solar multiple is set to be 3 with the design point DNI of 950 W/m^2. Since 58MW of thermal power is continuously required to calcinate the design mass flow rate of raw meal, the solar calciner is designed to absorb net thermal power of 175MW at its nominal condition. Because the design point DNI and the solar multiple are identical in all locations, the number of heliostats, the physical configuration of solar tower, and storage capacity are similar. The details are listed in Table 8. The physical parameters and the nominal operating conditions for the cement plant are listed in Table 4.

Table 8: CSP Physical Parameters for CSP Integrated Cement Plant

Plant Location	Number of Heliostats	Single Heliostat Area	Tower Height	Storage Capacity
SoCal	2219	144.4 m^2	104 m^2	880 MWh
NorCal	2309	144.4 m^2	97 m^2	880 MWh
PA	2215	144.4 m^2	104 m^2	880 MWh
AL	2216	144.4 m^2	104 m^2	880 MWh
TX	2221	144.4 m^2	104 m^2	880 MWh

4.6 CSP Integrated Cement Production Dynamics

The diurnal and seasonal dynamics must be resolved to determine the feasibility of CSP integrated cement. Thus, to compare the DNI and heat absorbed in the solar calciner, monthly profiles are evaluated at each location for a typical day in each season. The profiles are averaged for the months of March, June, September, and December with the error bars representing standard deviations which are shown in Figure 22 - Figure 25, respectively. As presented in Figure 22 - Figure 25, the irradiance varies across the locations. The plant located in SoCal has the highest peak (average) irradiance throughout the year whereas the plant located in PA has the lowest peak (average) throughout the year. Besides having the highest peak, the plant located in SoCal also has the longest solar availability. Typically, the plant in SoCal receives the highest amount of solar irradiation followed by the plant in NorCal, then PA or AL or TX, but for the month of December, the plant is TX receives the second-highest amount of solar irradiation. The average DNI profiles are not perfectly

upside parabolic as expected for a clear sunny day. Since the hourly DNI profiles are averaged for a given month, certain hours or days may be cloudy or rainy which induces fluctuations. More cloudy days at each location for a given month generate a wider range of standard deviation. For example, comparing the standard deviations of the SoCal plant to that of the PA plant for the month of June shown in Figure 23, the PA plant has a range of standard deviation more than two times wider than that of the SoCal plant. The profiles with a narrower range of standard deviation resemble a month with fewer cloudy or rainy days in a particular location.

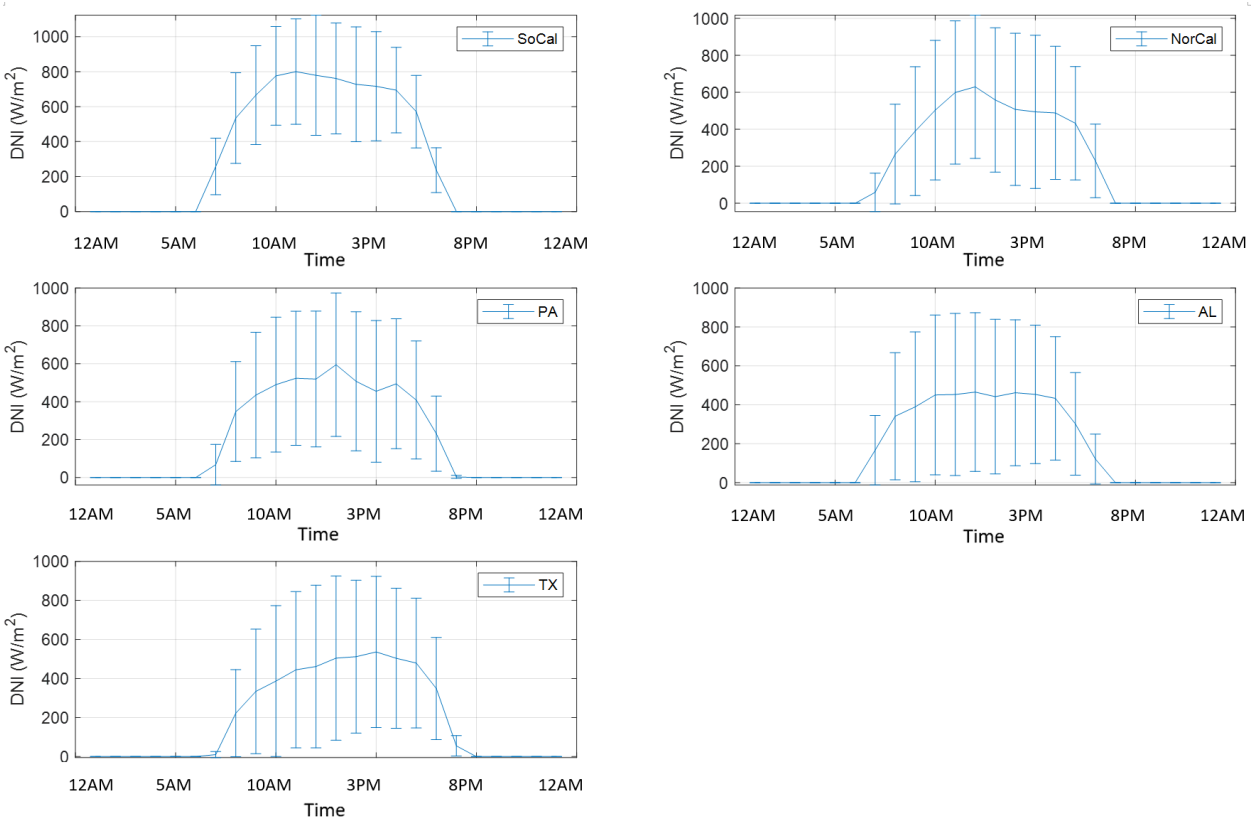

Figure 22: DNI Profile for the Month of March at Each Location, Typifying Spring

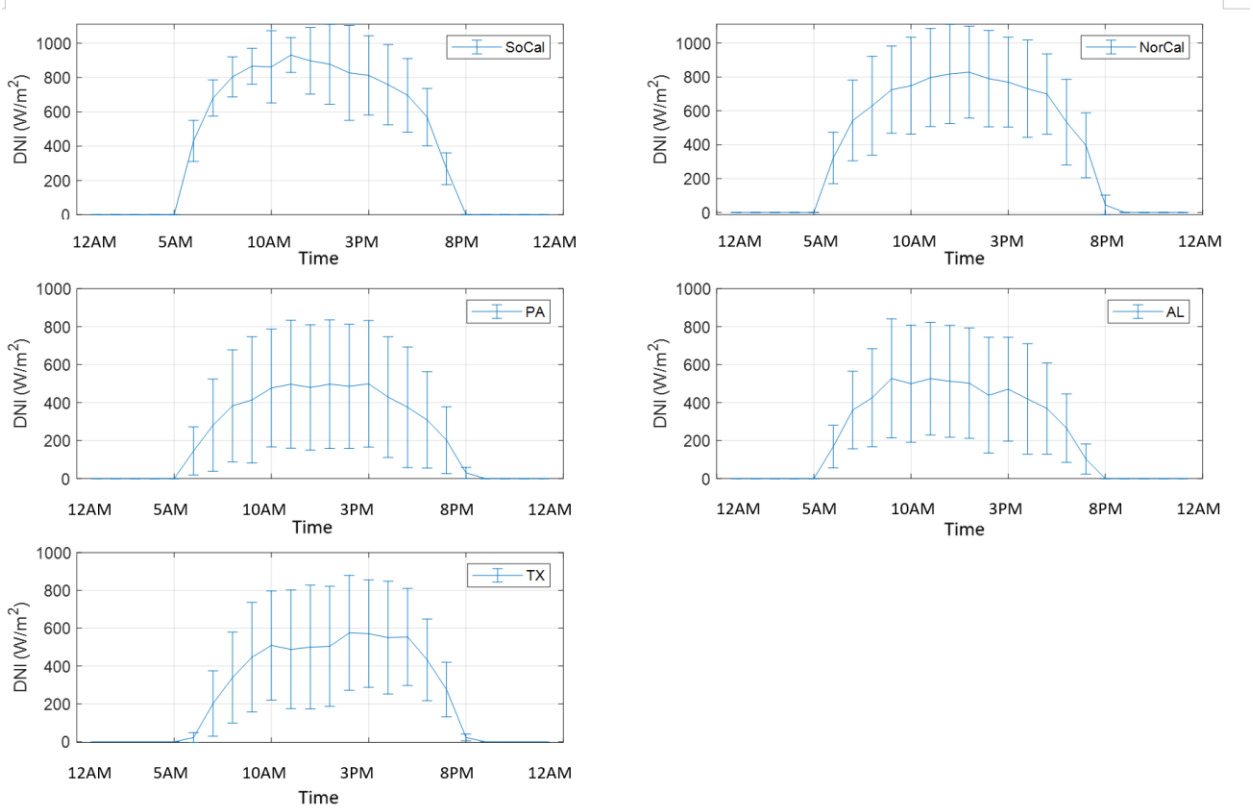

Figure 23: DNI Profile for the Month of June at Each Location, Typifying Summer

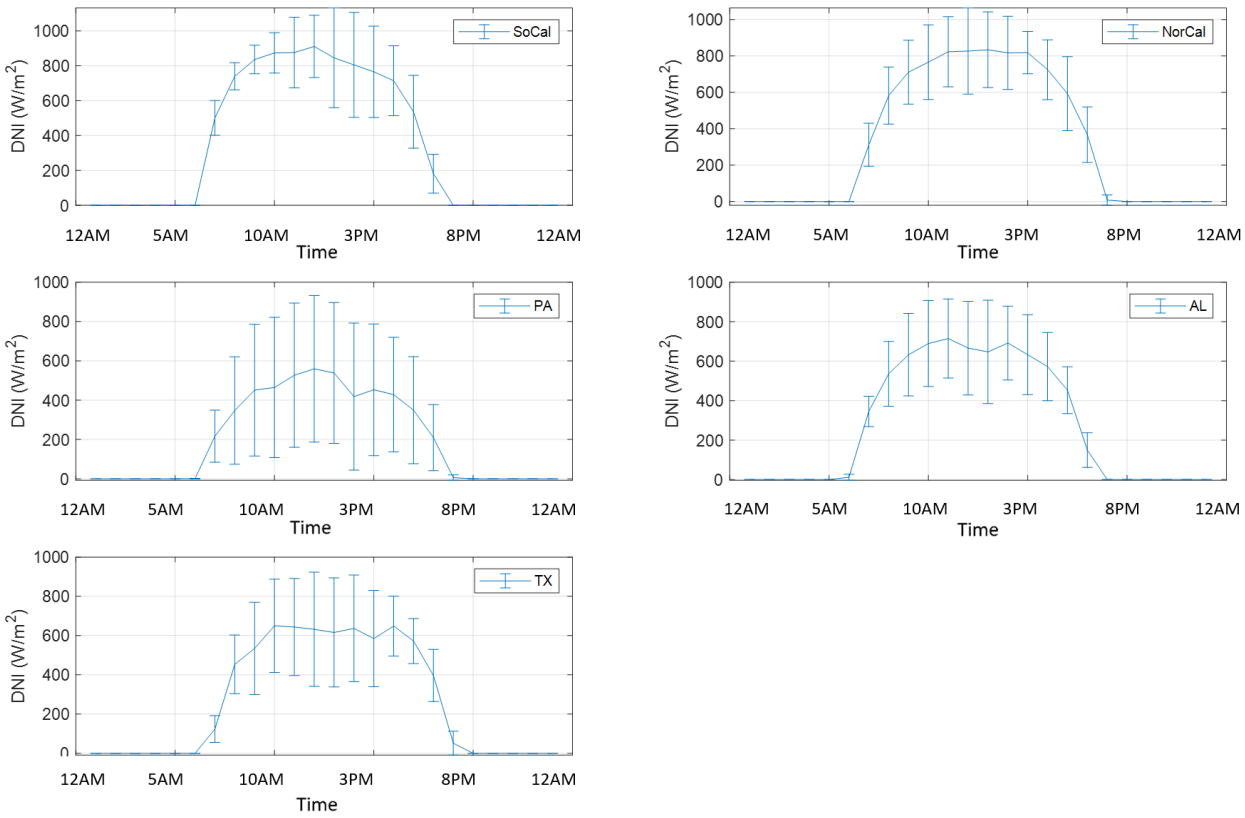

Figure 24: DNI Profile for the Month of September at Each Location, Typifying Fall

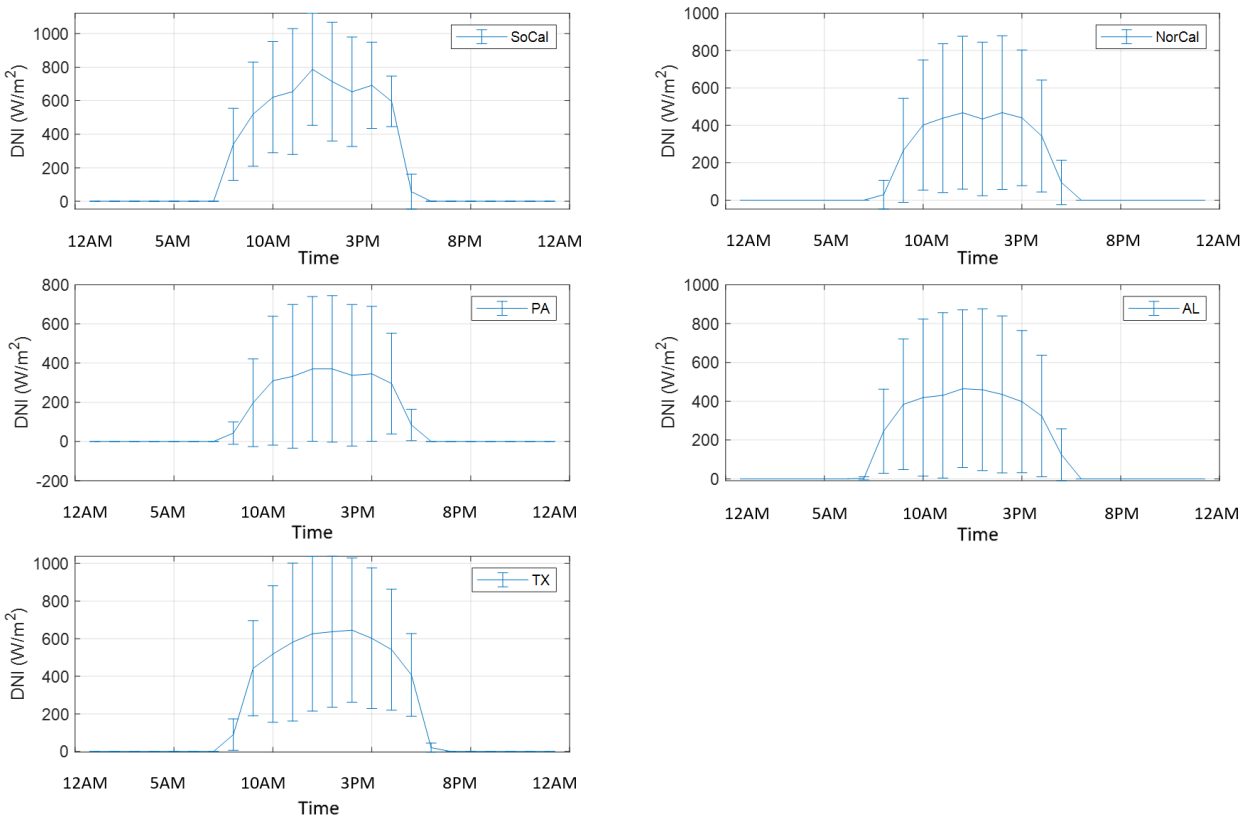

Figure 25: DNI Profile for the Month of December at Each Location, Typifying Winter

The simulated dynamics for the heat absorbed for the months of March – December are shown in Figure 26 – Figure 29, respectively. As expected, the heat absorbed is proportional to the DNI profile. Similarly, the heat absorbed in the calciner is averaged each hour at each location for the month of March, June, September, and December. For the month of June, however, a sudden decrease of absorbed heat occurs from 1 PM to 4 PM unlike any other month for plants located in California. The sudden drop occurs as a result of low heliostat field optical efficiency measured from 1 PM to 4 PM. Such behavior was only observed for the plants in California and only during the summer. Typically, lower field optical efficiencies are achieved due to lower field optical focus fraction, which is the fraction of the heliostat field that is focused. Therefore, it suggests that in SAM when the

heliostat field is generated for the plants in California, the optimization is performed such that cost is prioritized over performance. The amount of calcined clinker is proportional to the heat absorbed in the solar calciner. Therefore, based on Figure 26 -Figure 29, it is evident that the plant in SoCal can produce the highest amount of solar-calcined clinker while the plants in the East are expected to produce less solar-calcined clinker than the other plants investigated.

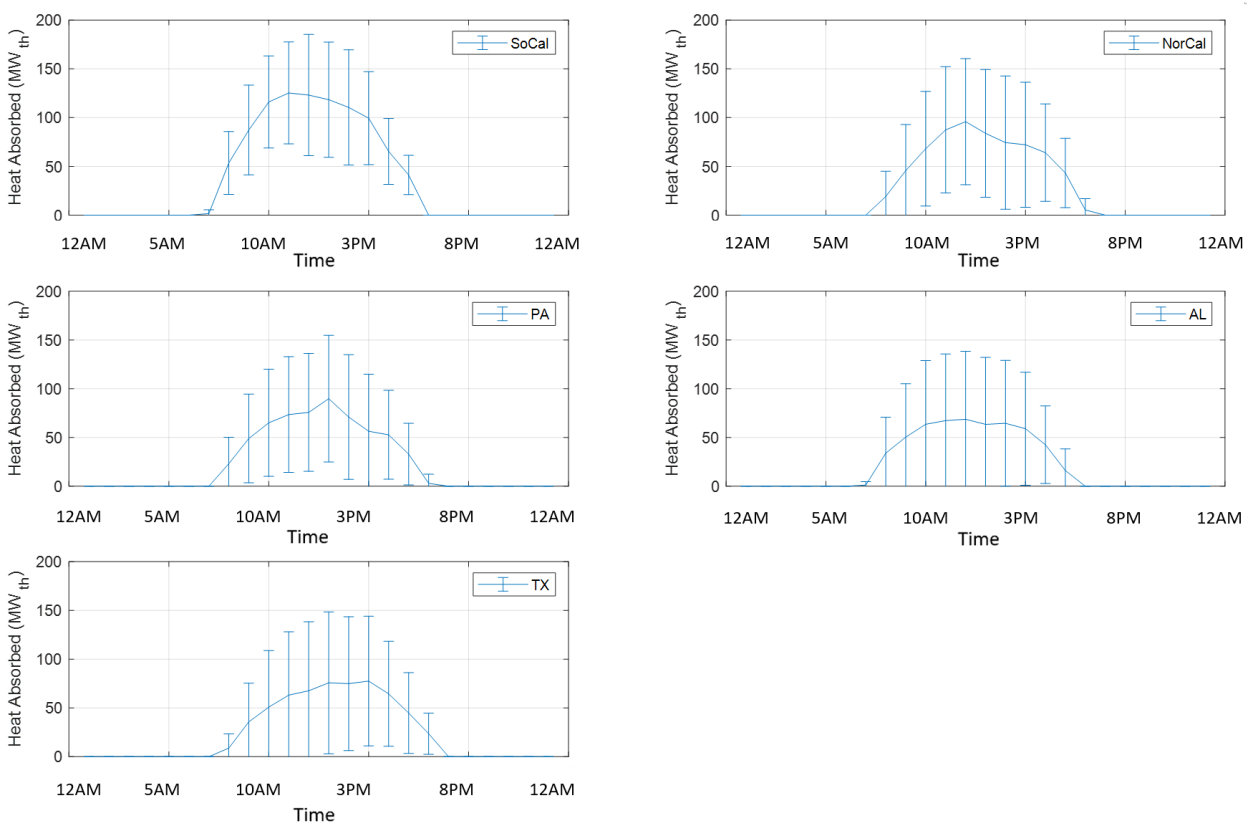

Figure 26: Heat Absorbed in Solar Calciner for the Month of March at Each Location

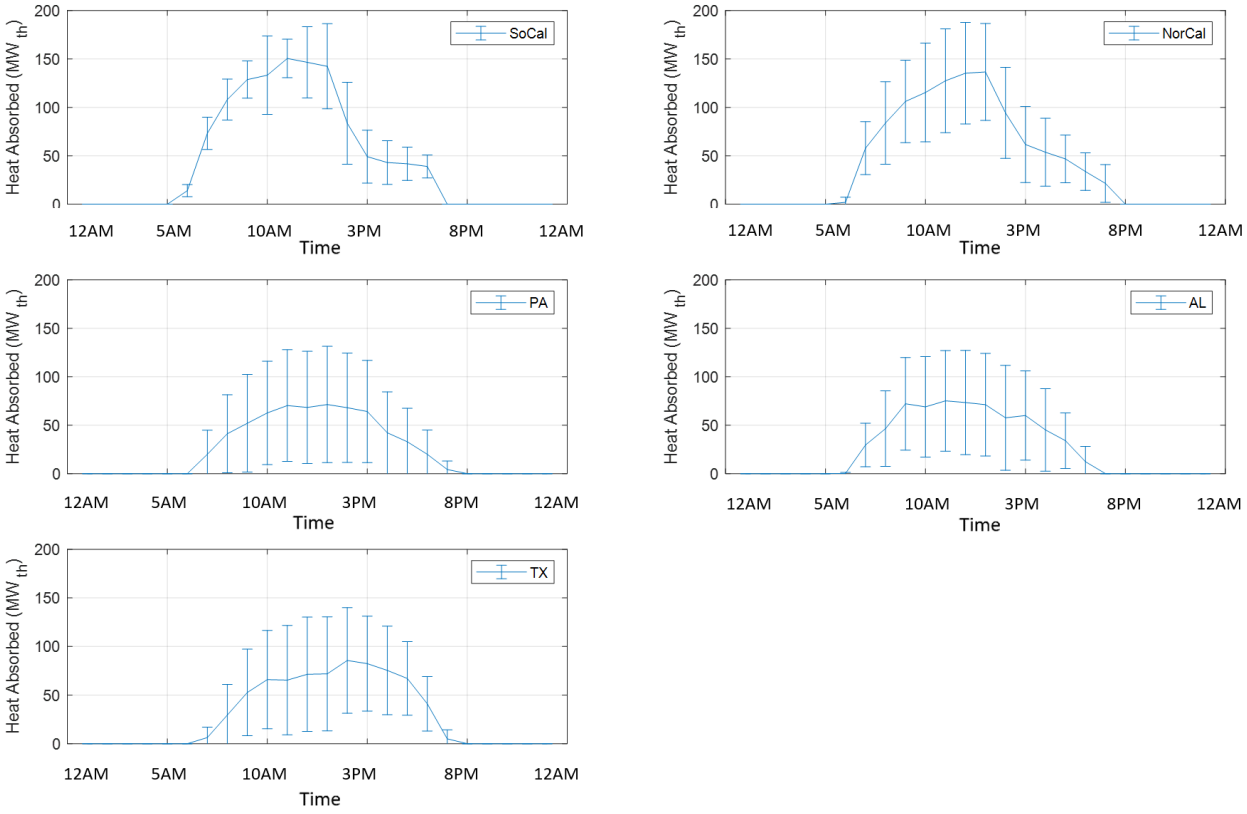

Figure 27: Heat Absorbed in Solar Calciner for the Month of June at Each Location

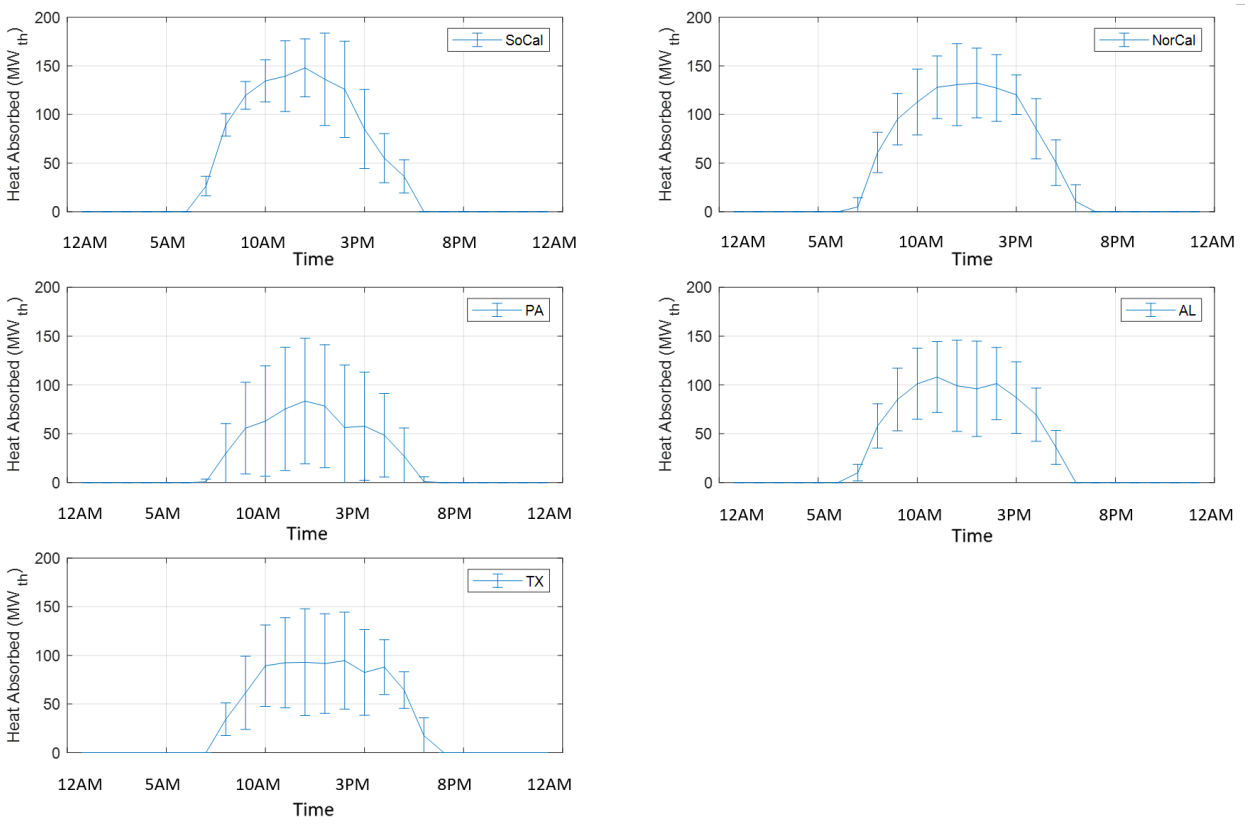

Figure 28: Heat Absorbed in Solar Calciner for the Month of September at Each Location

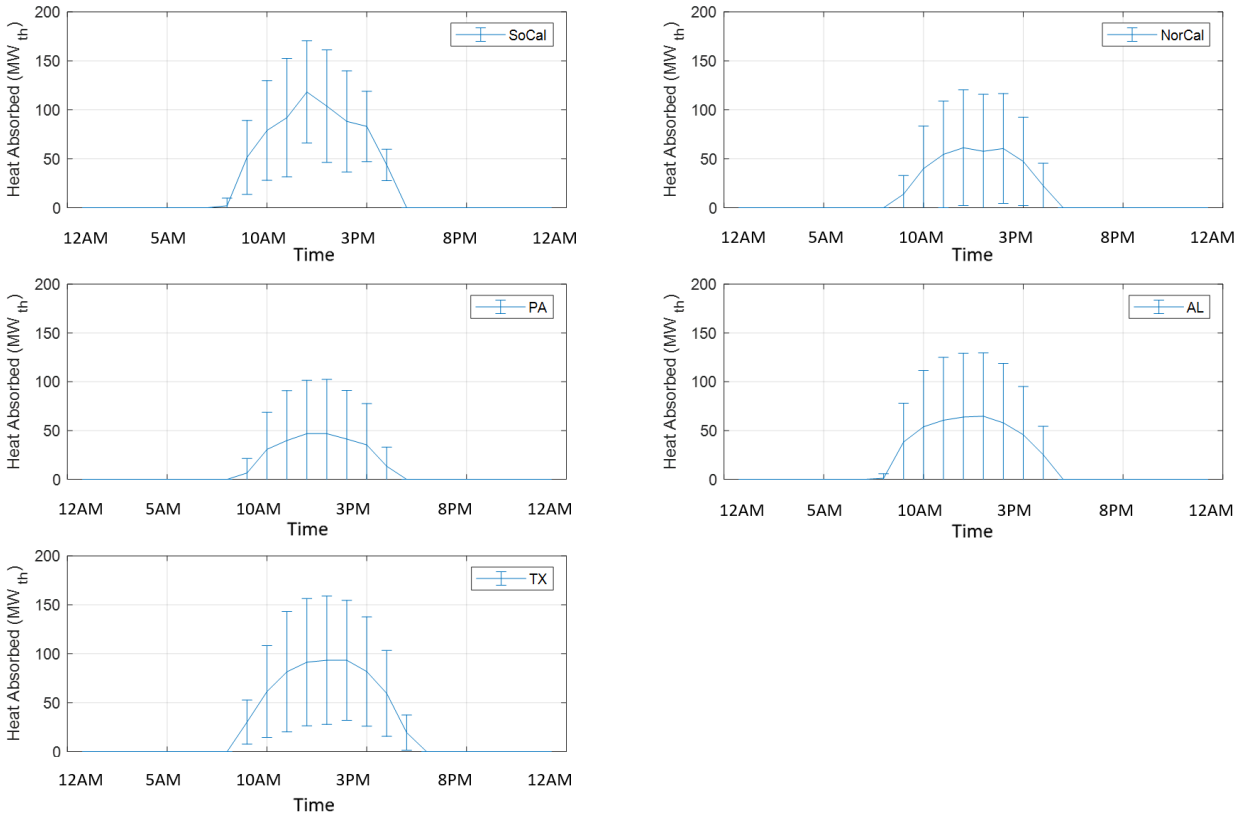

Figure 29: Heat Absorbed in Solar Calciner for the Month of December at Each Location

Figure 30 - Figure 33 show how the solar calciner and thermal storage in the SoCal plant complementarily operate for the first week of March, June, September, and December, respectively. As shown in the figures below, when excess solar thermal energy is garnered in the calciner, the calcined meal goes to both the kiln for sintering and to the storage for it to get sintered in the kiln later when solar is not available. For example, in Figure 26, the first four days resemble clear and sunny days whereas the fifth and sixth days represent cloudy days. As expected, during the first four days, the excess calcined meal goes to the storage until the solar calciner absorbs lower solar thermal power than 58MW which is the required thermal power for continuous operation of the kiln. The flat profile in the bottom figure is the period at which coal-fired calciner is activated to maintain the same amount of

clinker getting sintered in the kiln. The fact that shorter flat profiles are shown during the first four days signifies lower usage of coal-fired calciner which results in lower CO_2 emissions. The thermal power peaks at noon when the DNI reaches its maximum whereas the mass of stored clinker peaks in the afternoon. Although the DNI starts to decrease from noon, the mass of stored clinker peaks a few hours later because the calciner is still able to absorb solar thermal power of more than 58MW for continuous operation of the kiln, and the excess is stored in the storage. Therefore, for a typical sunny day, the mass of stored clinker peaks when the calciner begin to absorb less than 58MW of thermal power in the afternoon.

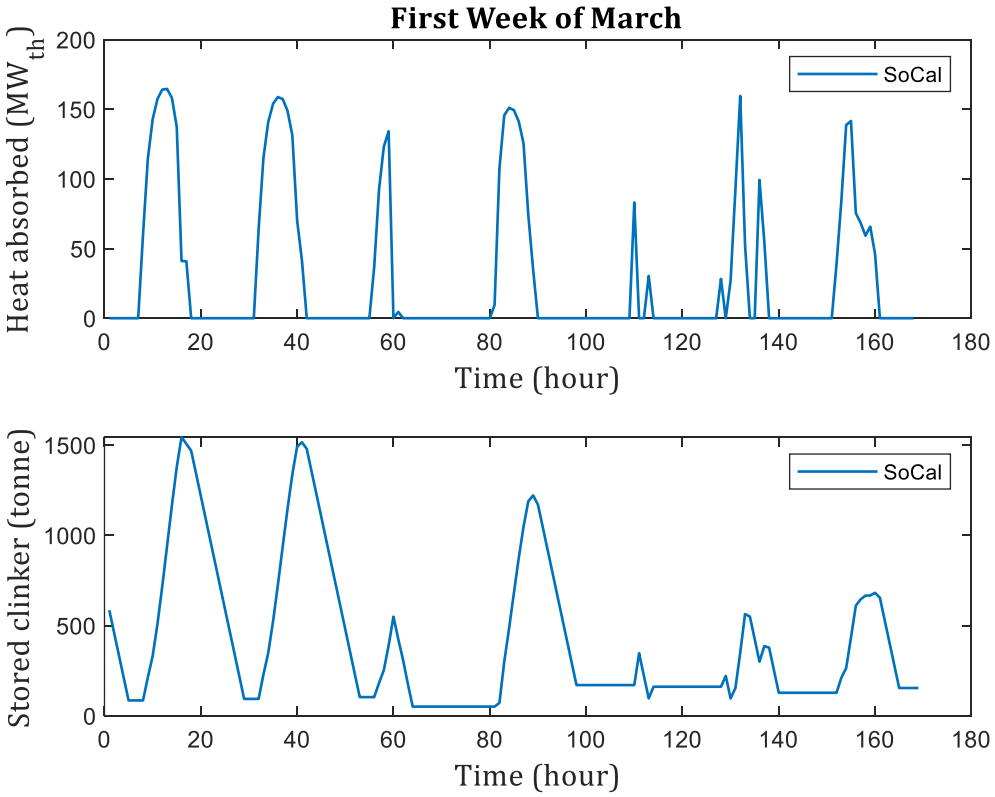

Figure 30: SoCal Plant Thermal Storage Operation for One Week in March

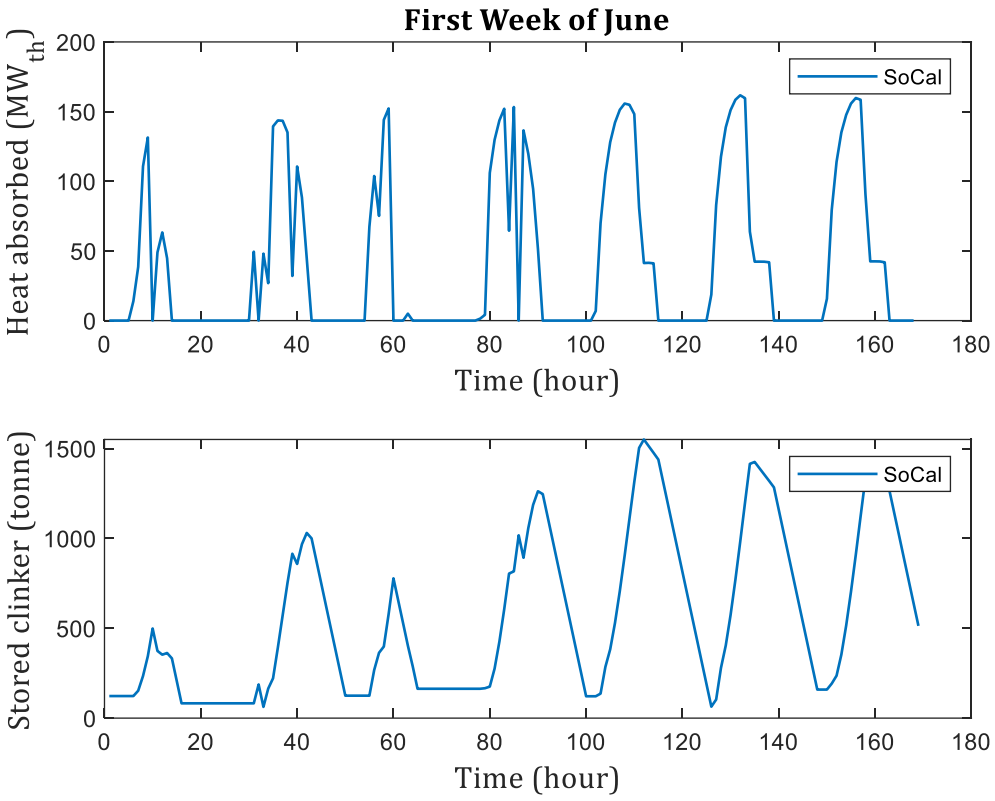

Figure 31: SoCal Plant Thermal Storage Operation for One Week in June

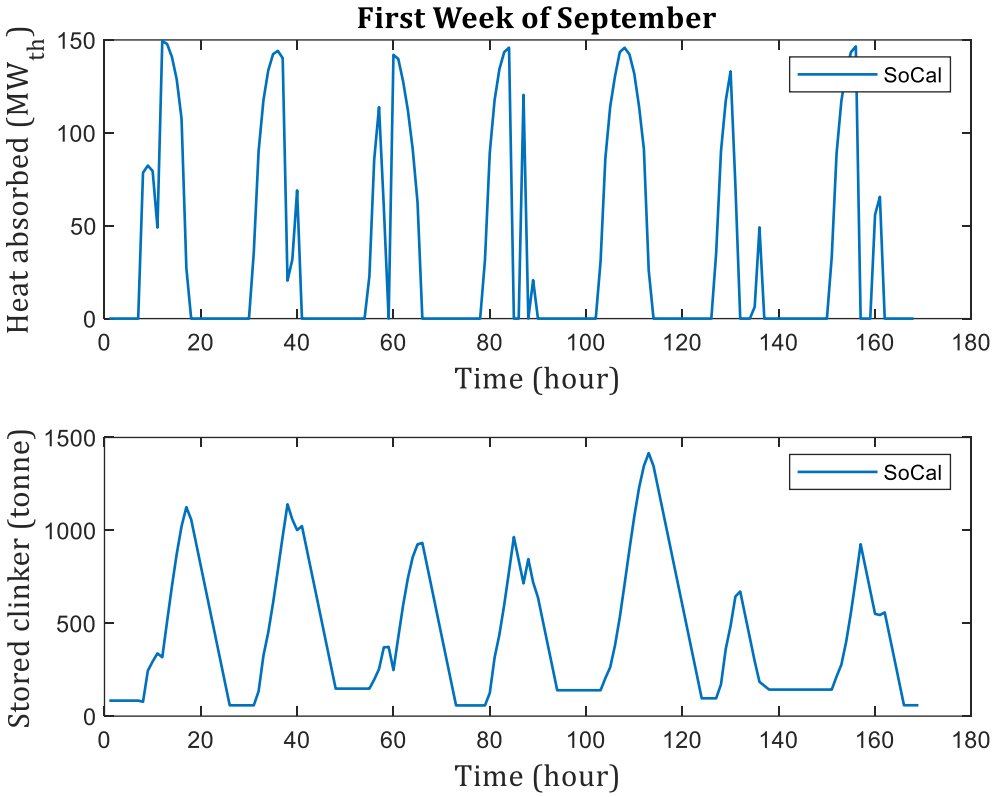

Figure 32: SoCal Plant Thermal Storage Operation for One Week in September

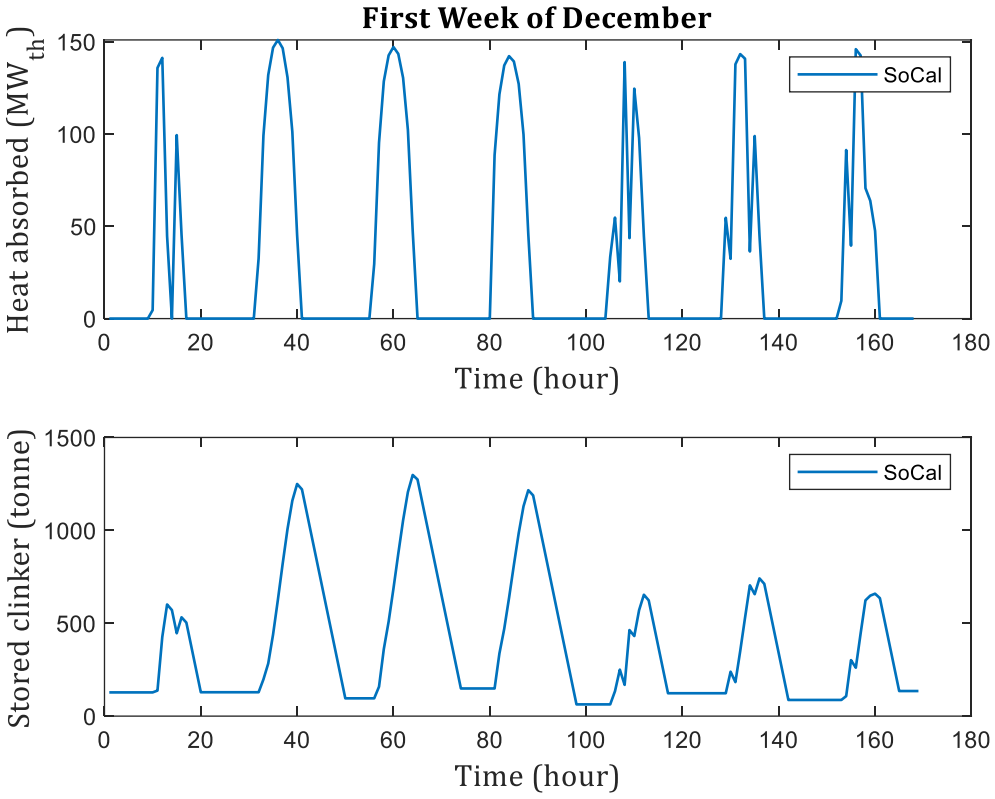

Figure 33: SoCal Plant Thermal Storage Operation for One Week in December

Figure 34 – Figure 37 also show how the thermal storage in the plant in PA complementarily operates for the month of March, June, September, and December, respectively. Noticeably, charging and discharging occurs much less frequently for the PA plant mainly due to lower DNI potential which results in lower solar thermal energy absorbed in the calciner given the same design condition. Because of longer inactive period for the thermal storage, the coal-fired calciner operates more frequently compared to the SoCal plant which ultimately causes more CO_2 emissions. The longer inactive period also has a negative impact on the temperature of the stored clinker. Quarterly/diurnal thermal storage operation profiles for NorCal, TX, and AL plants are attached in Appendix A.

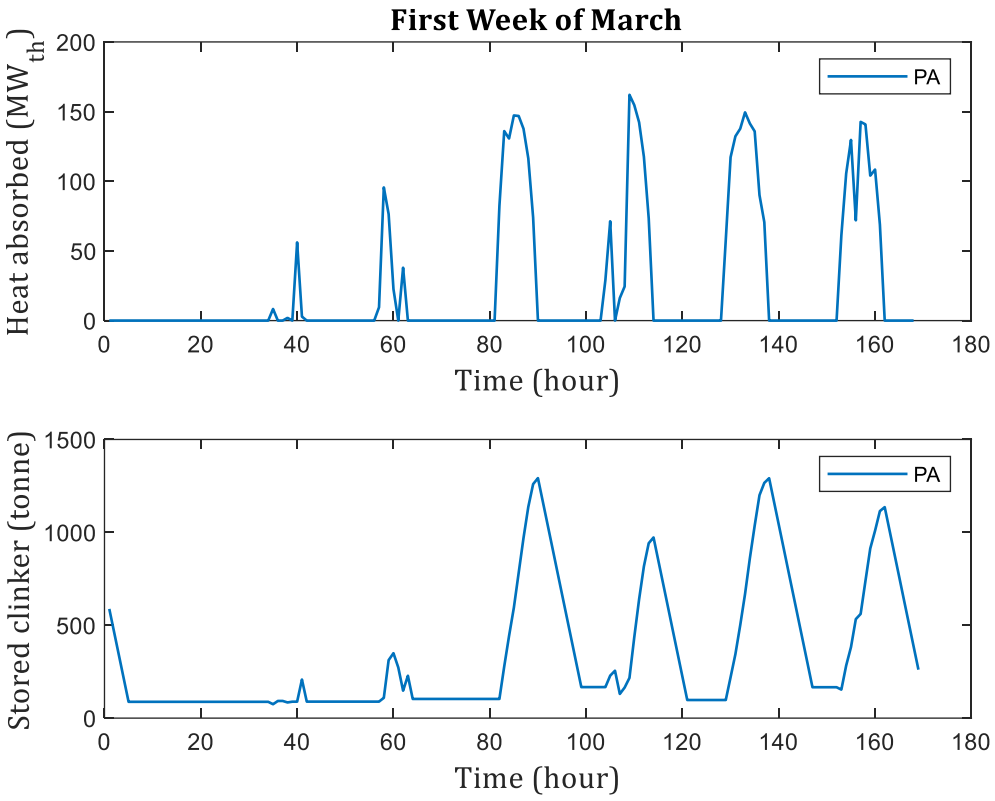

Figure 34: PA Plant Thermal Storage Operation for One Week in March

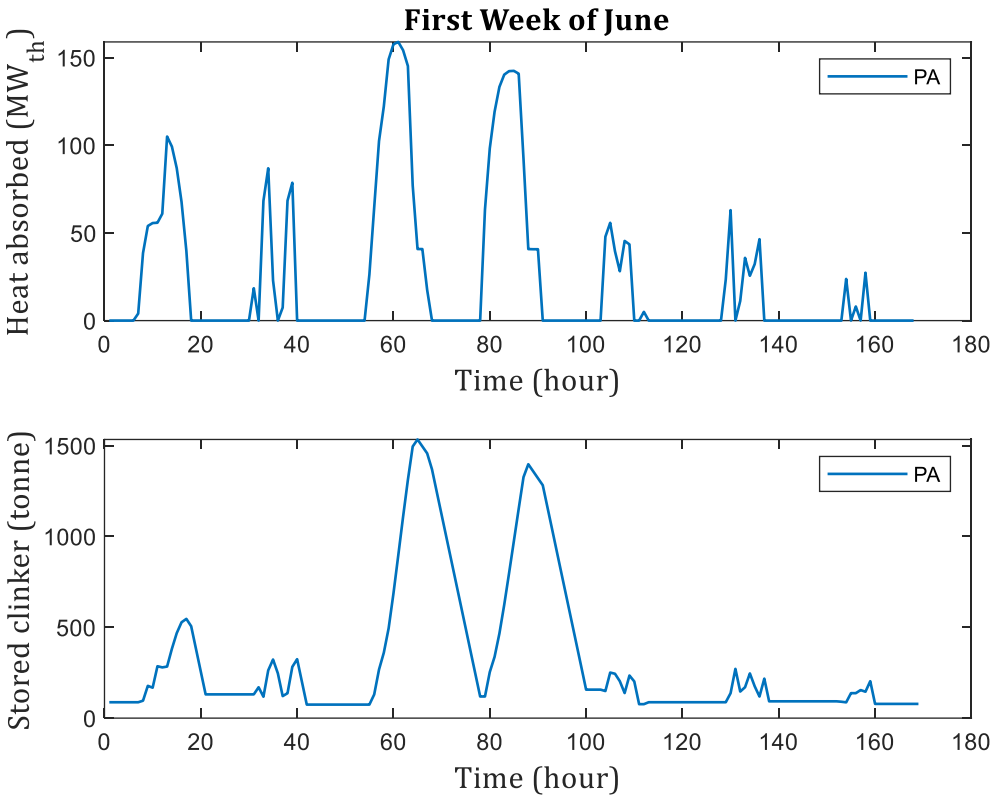

Figure 35: PA Plant Thermal Storage Operation for One Week in June

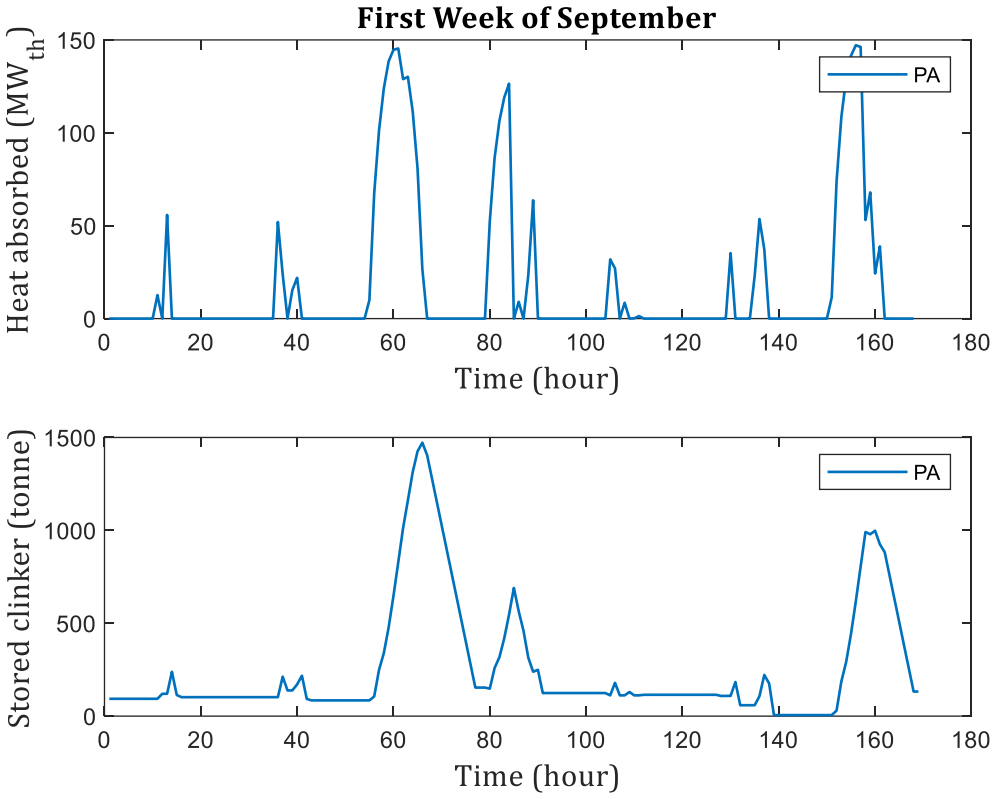

Figure 36: PA Plant Thermal Storage Operation for One Week in September

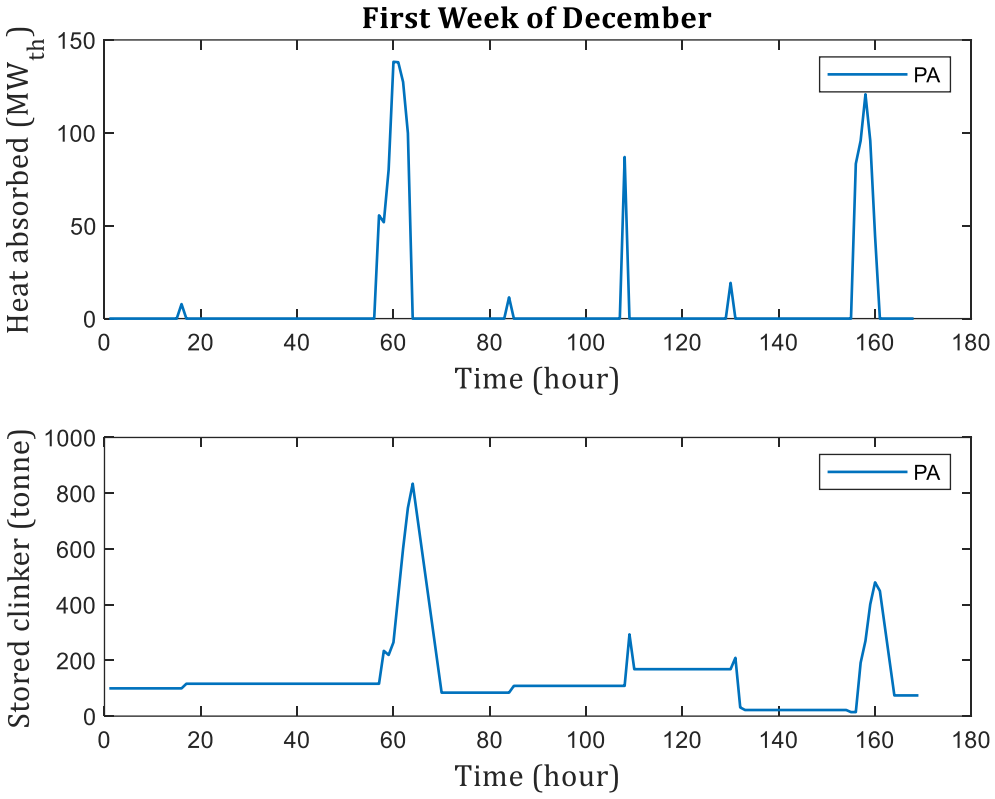

Figure 37: PA Plant Thermal Storage Operation for One Week in December

Annual simulations for the five plants are performed to investigate how the plants operate continuously. The heat absorbed in the solar calciner which is proportional to the production of clinker in the solar calciner, the amount of stored clinker in the storage, and the storage temperature are shown in Figure 38 – Figure 40 for the PA plant. The annual plots for the PA plant are first shown as an example because among the five plants studied, the DNI at the PA plant fluctuates the most due to many more storms and cloudy days. As shown in the figures, although the clinker production fluctuates throughout the operation, the storage successfully stores and dispatches the required amount of clinker for continuous operation of the kiln with coal additionally supplied to a coal-fired calciner

when needed. The temperature of clinker in the storage does not drop substantially because an electrical heater is activated when the temperature drops more than 10 K from the nominal temperature especially while dispatching the stored clinker under low state of charge. Annual heat absorbed in the solar calciner and storage profiles for the integrated plants in AL, and TX are shown in Figure 41 – Figure 46. The annual simulations for the plants in California are shown in Appendix B.

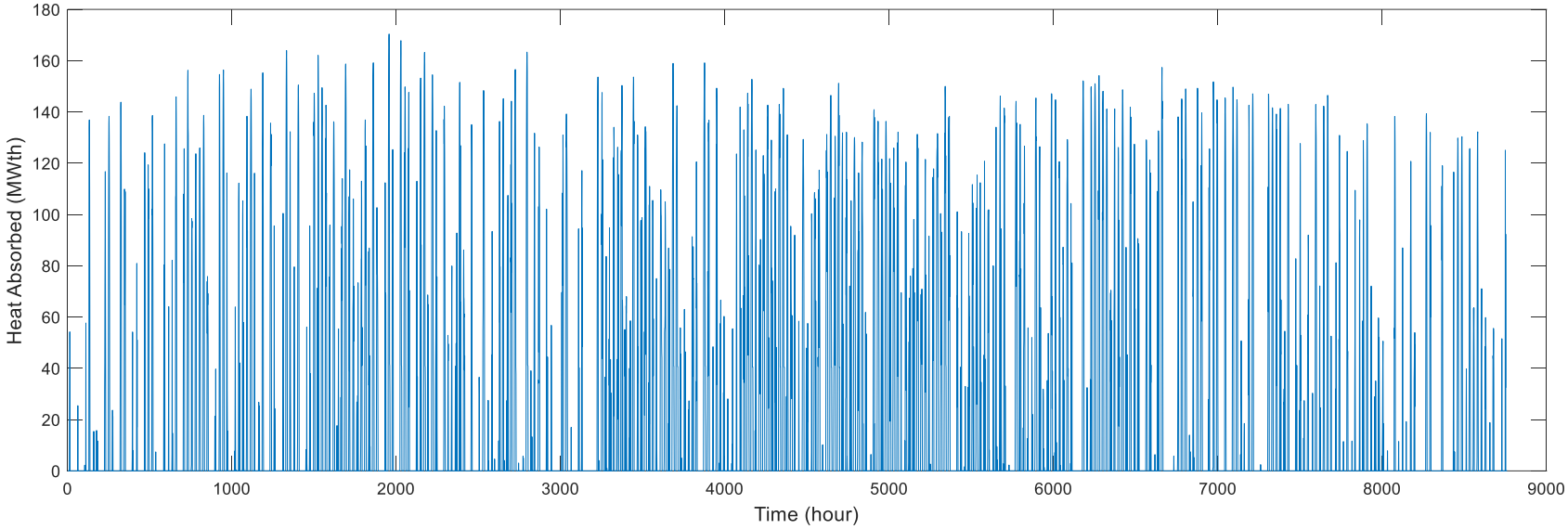

Figure 38: PA Plant Solar Calciner Dynamics for a Complete Annual Simulation

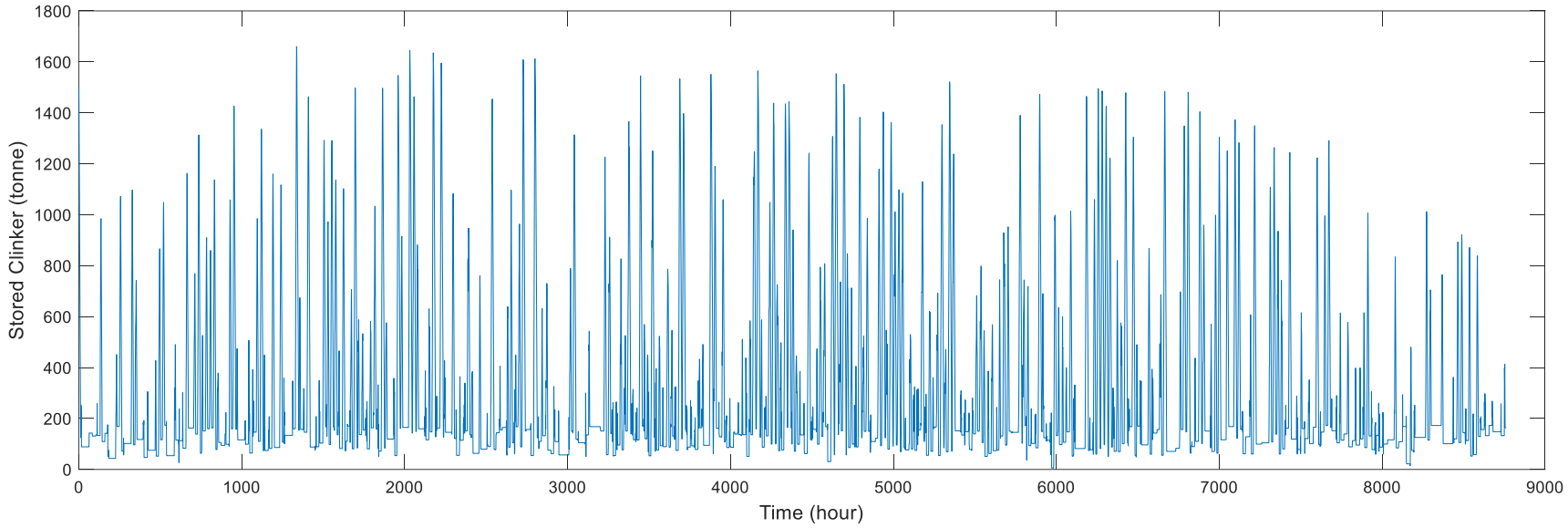

Figure 39: PA Plant Storage Mass Dynamics for a Complete Annual Simulation

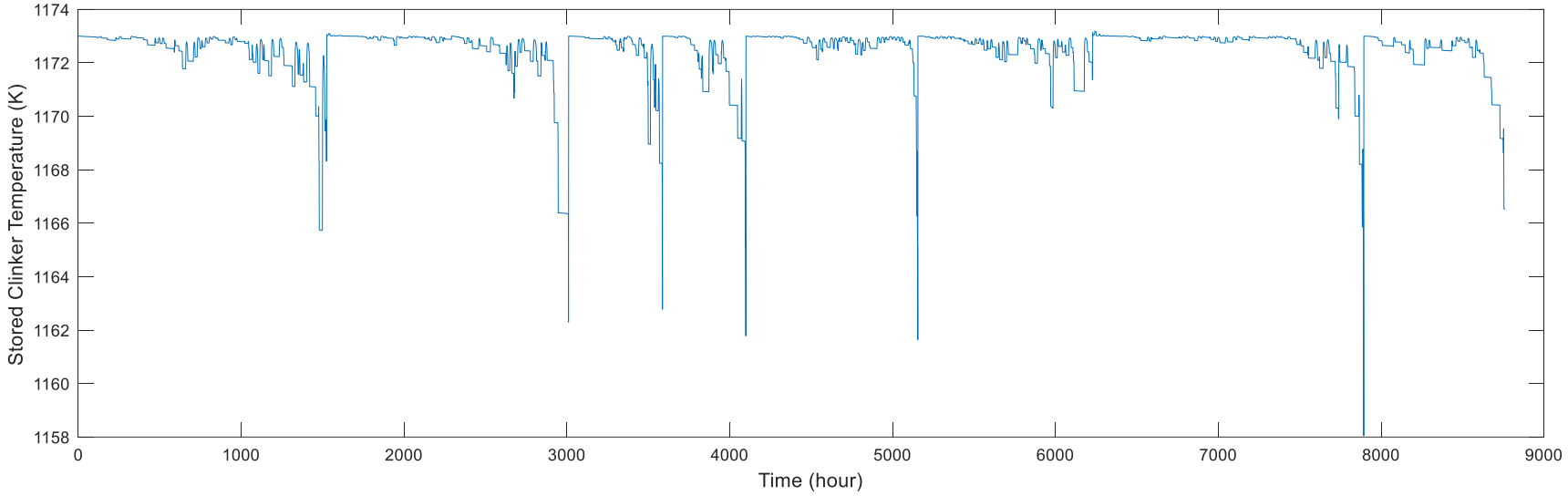

Figure 40: PA Plant Storage Temperature Dynamics for a Complete Annual Simulation

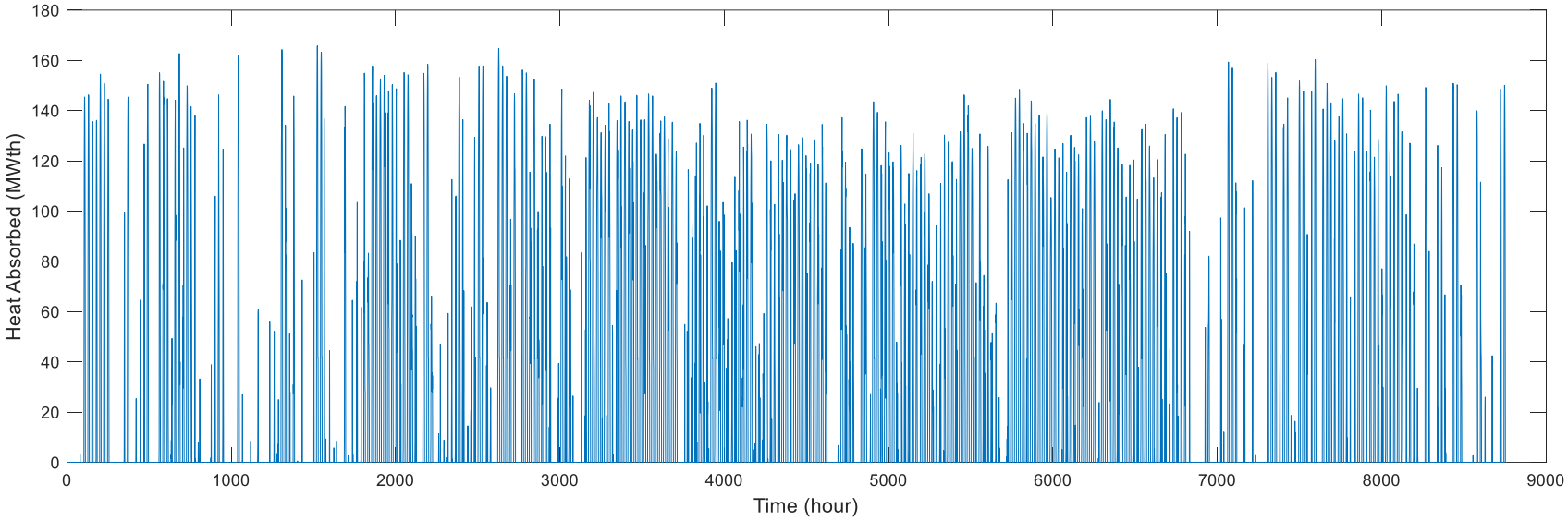

Figure 41: AL Plant Solar Calciner Dynamics for a Complete Annual Simulation

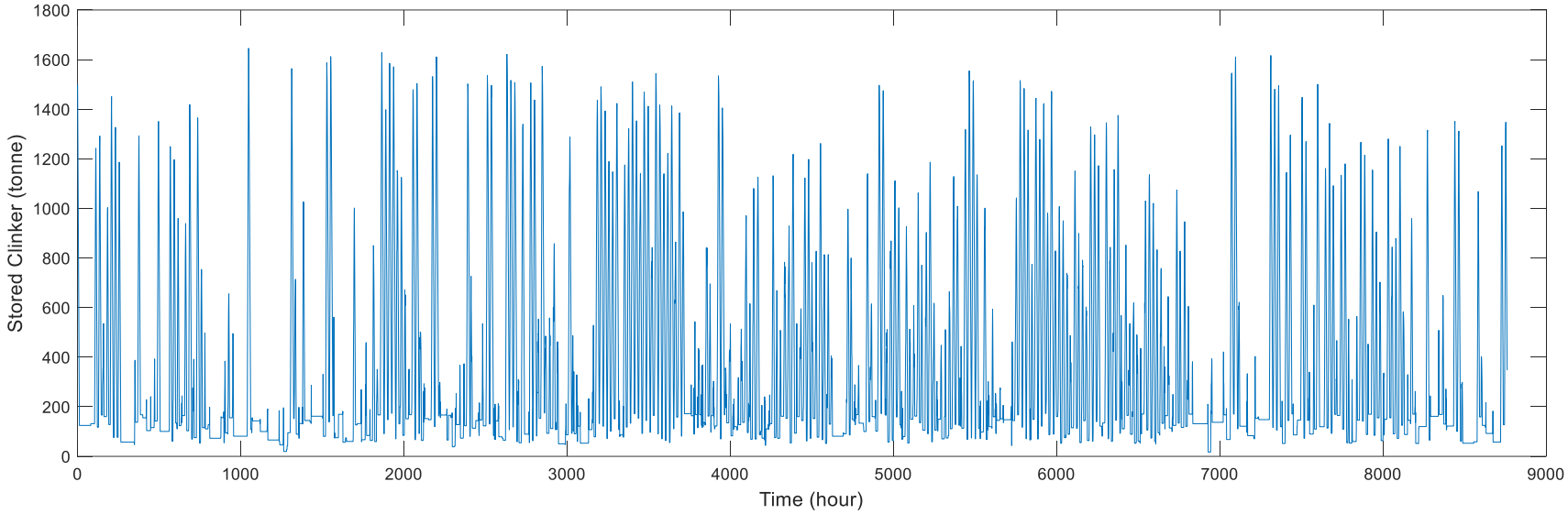

Figure 42:AL Plant Storage Mass Dynamics for a Complete Annual Simulation

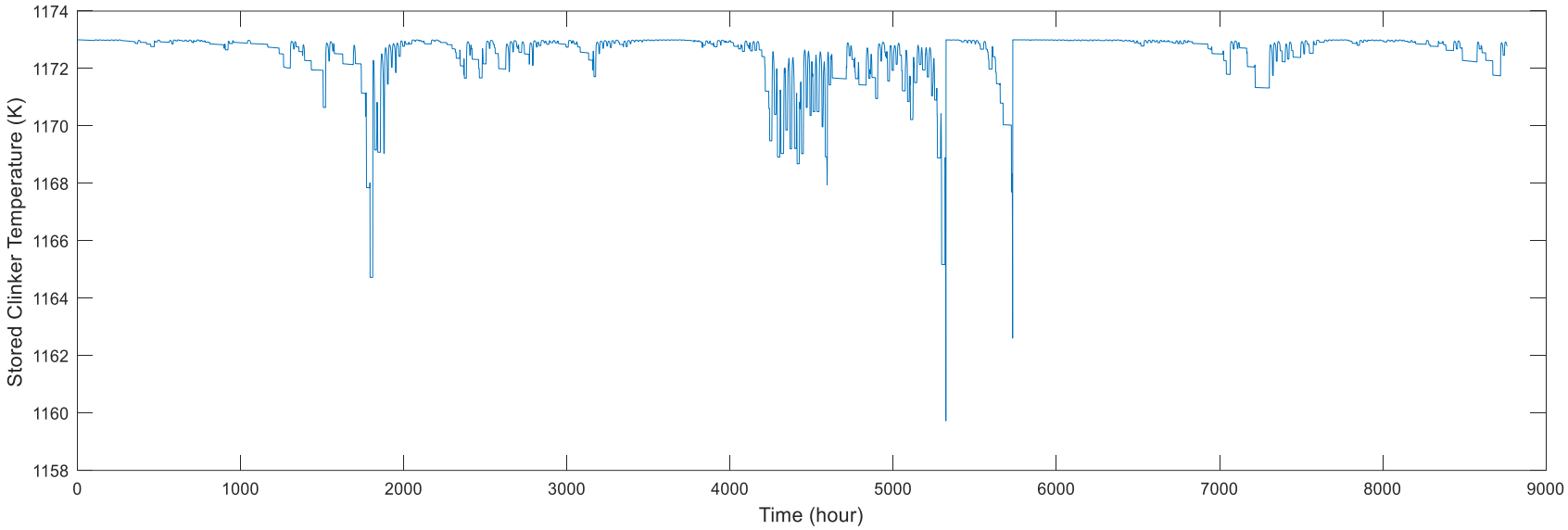

Figure 43: AL Plant Storage Temperature Dynamics for a Complete Annual Simulation

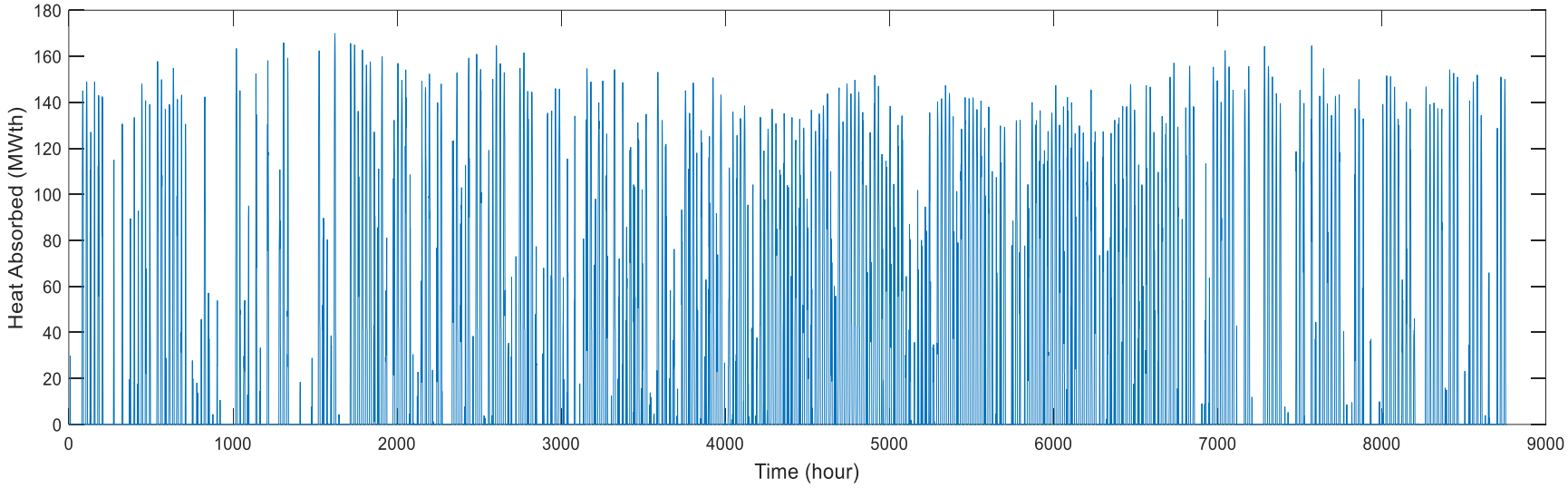

Figure 44:TX Plant Solar Calciner Dynamics for a Complete Annual Simulation

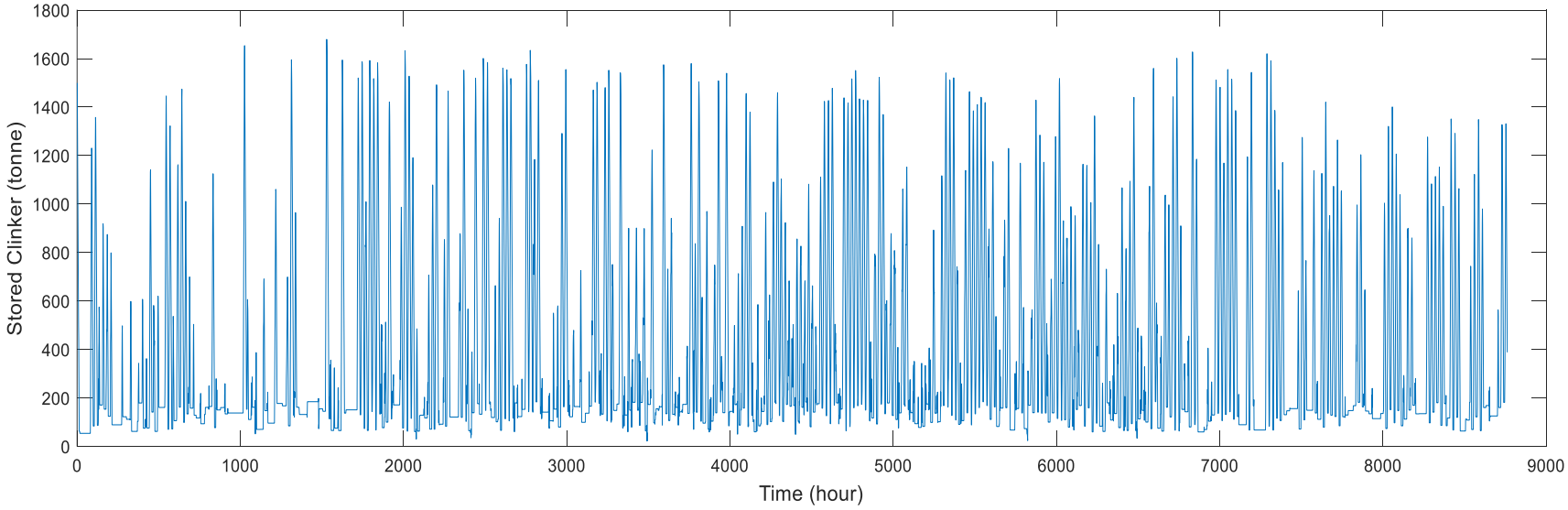

Figure 45:TX Plant Storage Mass Dynamics for a Complete Annual Simulation

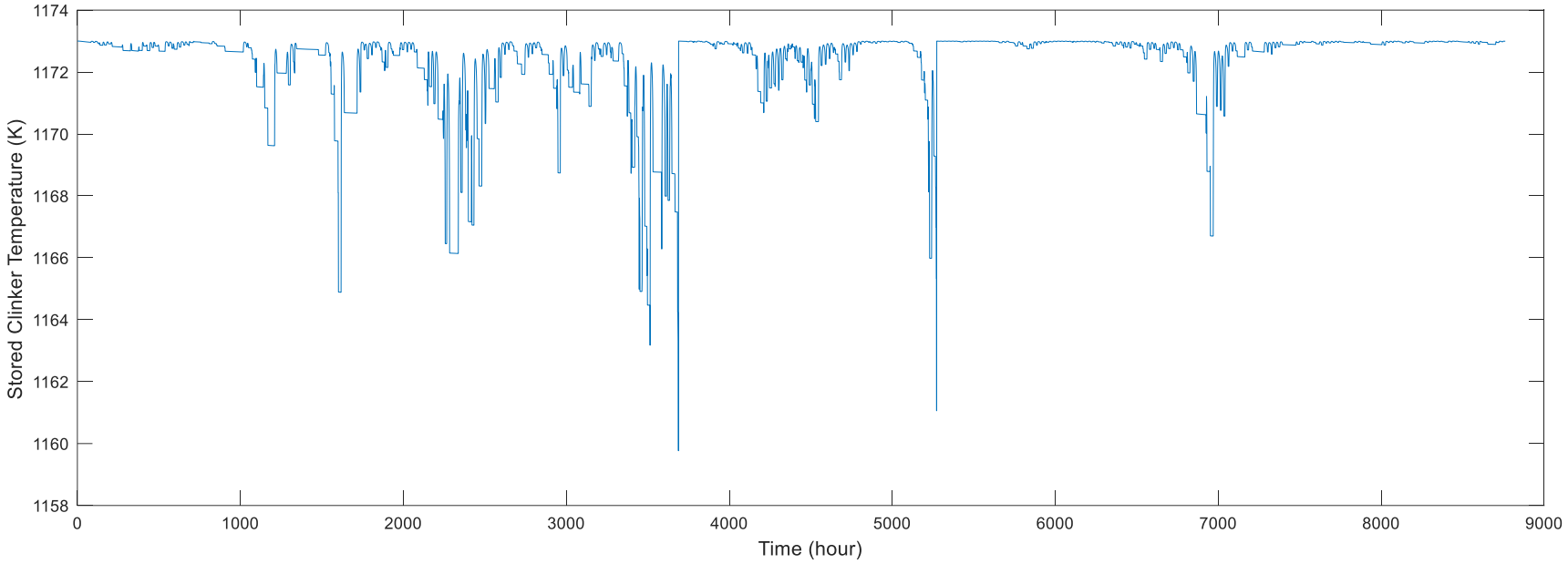

Figure 46: TX Plant Storage Temperature Dynamics for a Complete Annual Simulation

4.7 Performance Characteristics Assessment

To evaluate the performance characteristics of the CSP-integrated cement plants, the percent solarization and percent CO_2 emission reduction are evaluated. Both parameters are closely related to the DNI potential at the site, the capacity of thermal storage and solar calciner, and solar multiple. Since the capacity of thermal storage and solar calciner, and solar multiple are identical for all five plants analyzed, the parameters are proportional to the DNI potential. As shown in Figure 47, the SoCal plant is able to utilize solar thermal energy more than 70% of the operating time which is the maximum percent solarization among the other plants. The lowest solarization is achieved for the PA plant, only able to solarize 40% of the time. The essential difference between the two plants is the difference between the DNI potential. Annually, the SoCal plant receives DNI of 3000 kWh/m^2 while the PA plant receives DNI of1500 kWh/m^2. Although the solarization of the SoCal plant is not strictly half of the PA plant's, analyzing the DNI and solarization of the other plants, it is evident that percent solarization is proportional to the DNI potential given the same storage capacity, solar multiple, and design DNI point.

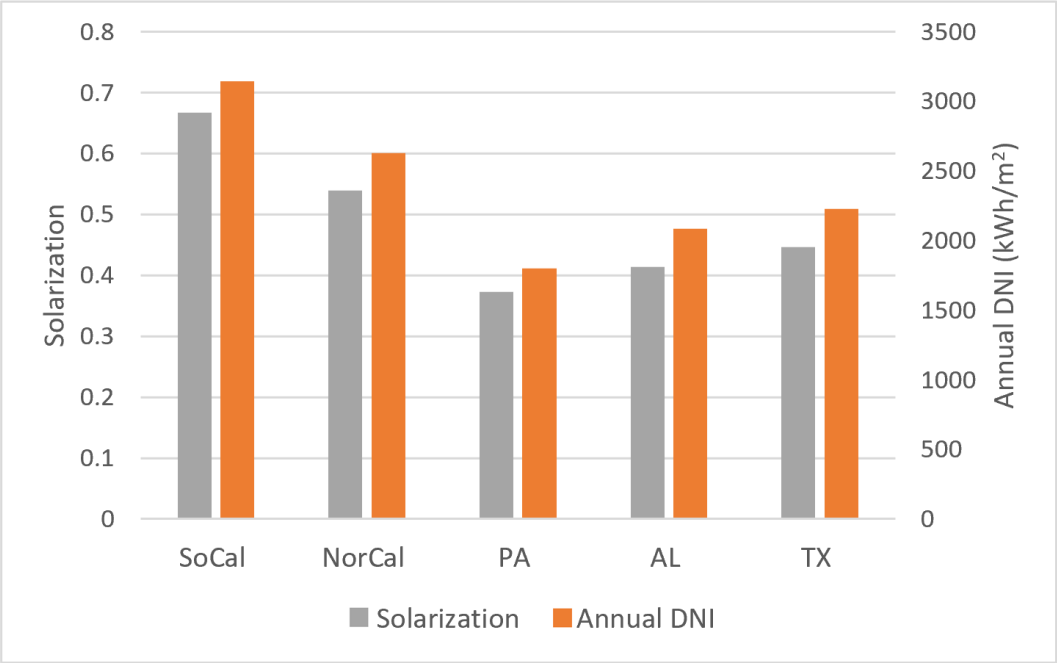

Figure 47: Solarization and Annual DNI

To further evaluate the performance characteristics of the integrated plant, the percent CO_2 emissions reduction at each plant is analyzed. Because CO_2 is emitted from processing of the material and burning of coal, achieving a zero-carbon emission is not possible without carbon capture. Given the maximum percent reduction of carbon emissions for the CSP-integrated cement plant, the percent reduction can be estimated for each plant investigated. Table 9 shows the percent reduction in CO_2 emissions at each plant as well as the amount of coal saved with the CSP integration. The saved amount of coal is calculated based on the CO_2 emissions reduction.

Table 9: CO_2 Emissions Reduction and Saved Amount of Coal

Location	Percent CO_2 emissions reduction (%)	Saved amount of coal (tonnes)
SoCal	15.1	54,400
NorCal	12.6	45,400
PA	8.63	31,100
AL	9.99	36,000
TX	10.7	38,500

As shown in the table above, for the SoCal plant, 15% of the CO_2 emissions can be avoided once a coal-fired cement plant is integrated with a CSP plant. However, much less is avoided for the PA plant due to lower solarization; which is only able to avoid 9% of the total carbon emissions. Again, the percent CO_2 emissions reduction depends ultimately on the DNI potential at each location. In the United States, referring to Figure 21, the West Coast region, including New Mexico and Colorado, seems to be a more ideal region for CSP integration than the East Coast. To achieve similar CO_2 emissions reduction in the East Coast, larger heliostat field must be established which leads to higher capital costs and higher carbon avoided costs. The saved amount of coal which is proportional to the reduction in the emissions is used to re-calculate the operating and maintenance costs where depending on the amount of coal saved, the operating and maintenance costs can be negative.

4.8 Economic Analysis of CSP Integrated Cement Plant

To assess the economics of the integrated cement plant, the costs of CO_2 avoided are estimated for each plant and compared to that of existing carbon capture technologies. The costs of CO_2 avoided are defined based on the costs of clinker and equivalent specific CO_2 emissions with and without carbon capture technology. The costs of clinker are determined by the annualized CAPEX and OPEX. Because the costs of clinker are defined by per ton of clinker produced, the annual production of clinker is also taken into consideration. Since each plant has the same DNI design point, solar multiple, and storage capacity, the CAPEX is similar for all CSP-integrated plants as shown in Figure 48. Because the CAPEX of the five plants is similar, the OPEX and CO_2 emissions are the determining factors for calculating the costs of CO_2 avoided.

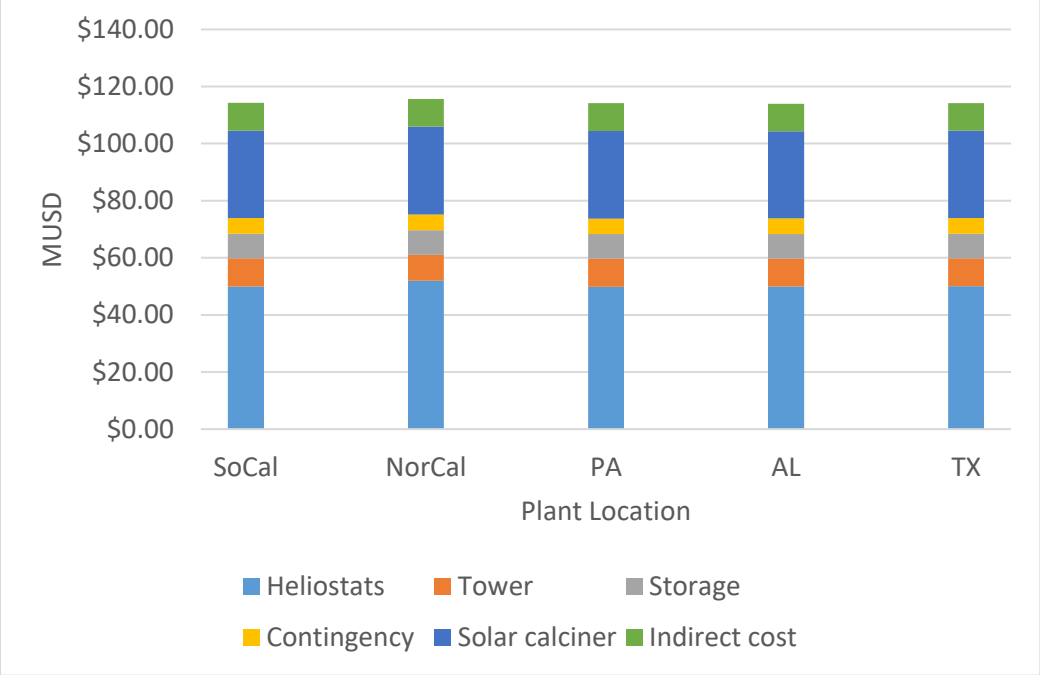

Figure 48: CAPEX Breakdown for Each Plant

The sensitivity of the CO_2 avoided costs to the input parameters is evaluated for the SoCal plant. The results are shown in Figure 50, showing the varied parameters and the changes in the costs. As shown in the figure, the interest rate and heliostat costs have significant impact on the avoided costs. The tower, solar calciner, storage, and contingency costs have small impact on the costs. Therefore, reducing the interest rate and the heliostat costs must be prioritized to further reduce the avoided cost.

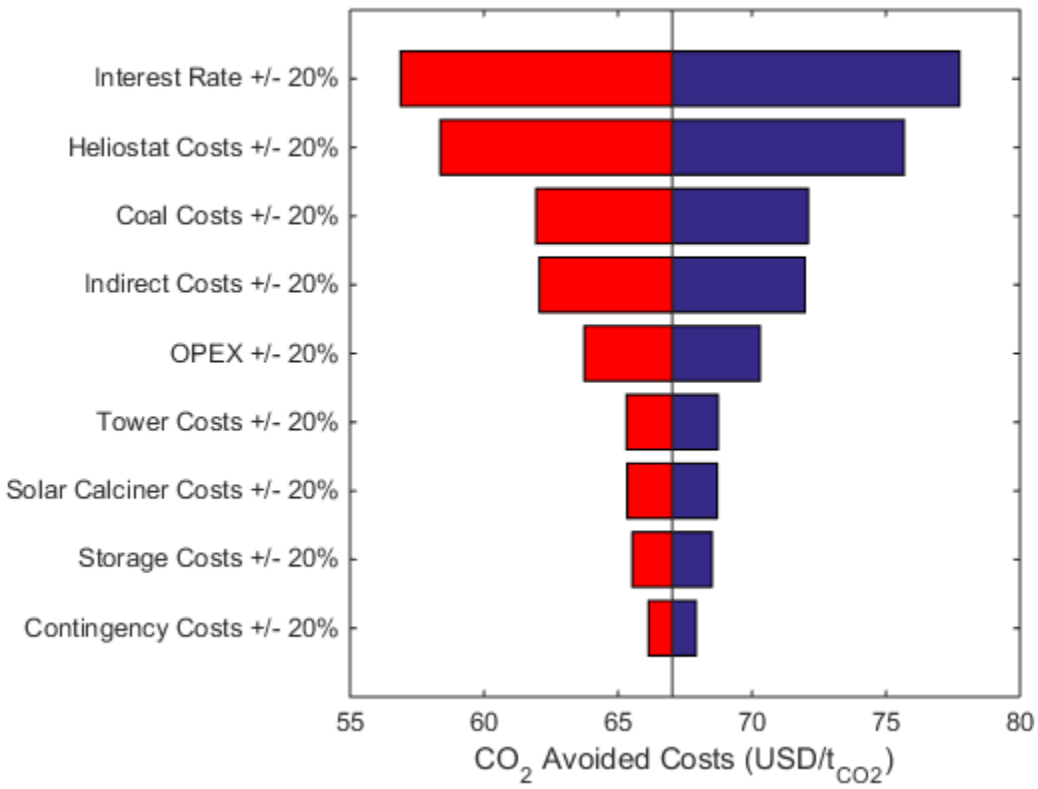

Figure 49: Sensitivity Analysis on the Avoided Cost

The costs of CO_2 avoided for cement plants integrated with existing carbon capture technologies are estimated by Gardarsdottir [54], using the same reference plant [61] as the current work. To properly compare the costs, similar assumptions have been imposed for estimating the cost of CO_2 avoided for each CSP integrated cement plant where

economic life of 25 years and a discount rate of 8% are applied. Figure 50Figure *50*: Costs of CO_2 Avoided for Integrated Cement Plants shows the costs of CO_2 avoided for the cement plant integrated with existing carbon capture technologies as well as the CSP integrated cement plants. The CSP integrated cement plants and carbon capture technologies are represented by the orange and blue bars in the figure, respectively. Noticeably, the SoCal plant with the annual DNI of 2920 kWh/m^2 and the NorCal plant with the annual DNI of 2630 kWh/m^2 can compete with cement plants integrated with existing carbon capture technologies. However, the plants with lower annual DNI have higher costs of CO_2 avoided than that of the plants with carbon capture technologies. Therefore, for CSP integrated cement plants to be as economically competitive as the plants with carbon capture, the plants must have annual DNI of at least 2000 kWh/m^2.

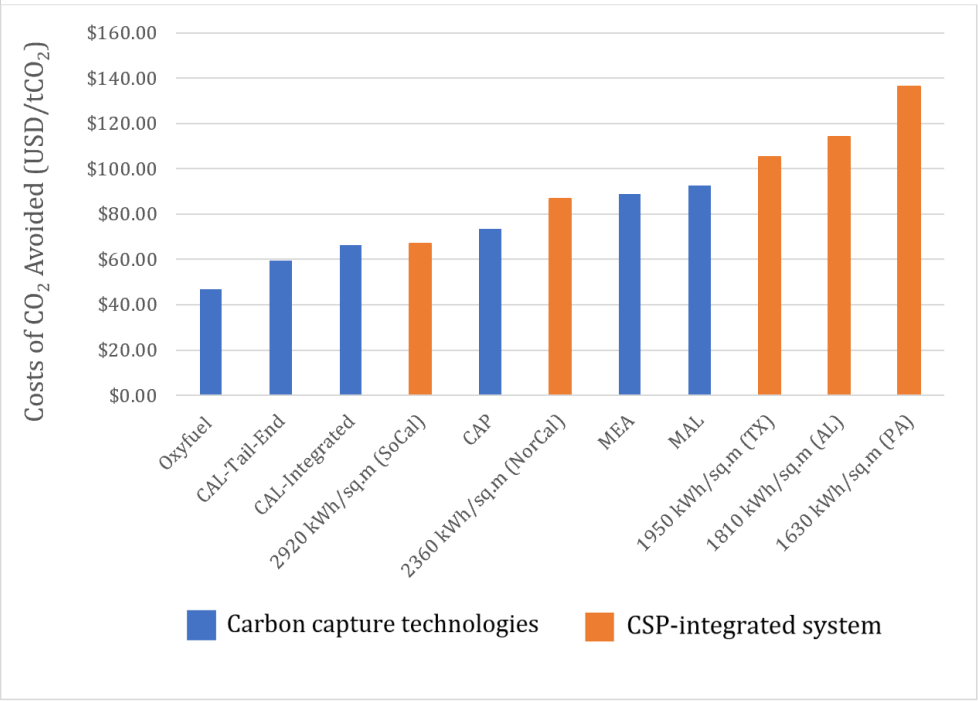

Figure 50: Costs of CO_2 Avoided for Integrated Cement Plants

Based on the costs of CO_2 avoided across the five CSP integrated cement plants, a trendline is generated for a rough estimation of the costs of CO_2 avoided as a function of annual DNI. As shown in Figure 51, as annual DNI decreases, the costs exponentially increase to the point where integration of CSP with cement plants is no longer economically competitive against integrating with other existing carbon capture technologies. The western region of the United States especially the state of California, Arizona, Nevada, and New Mexico is the best place for integrating a conventional cement plant with a CSP plant where the costs of CO_2 avoided range from 70 to 100 USD per ton of CO_2. Since such integration could not fully achieve decarbonization, a combination of CSP and carbon capture and storage is necessary to ultimately reduce the costs of CO_2 avoided and realize complete decarbonization in cement plants.

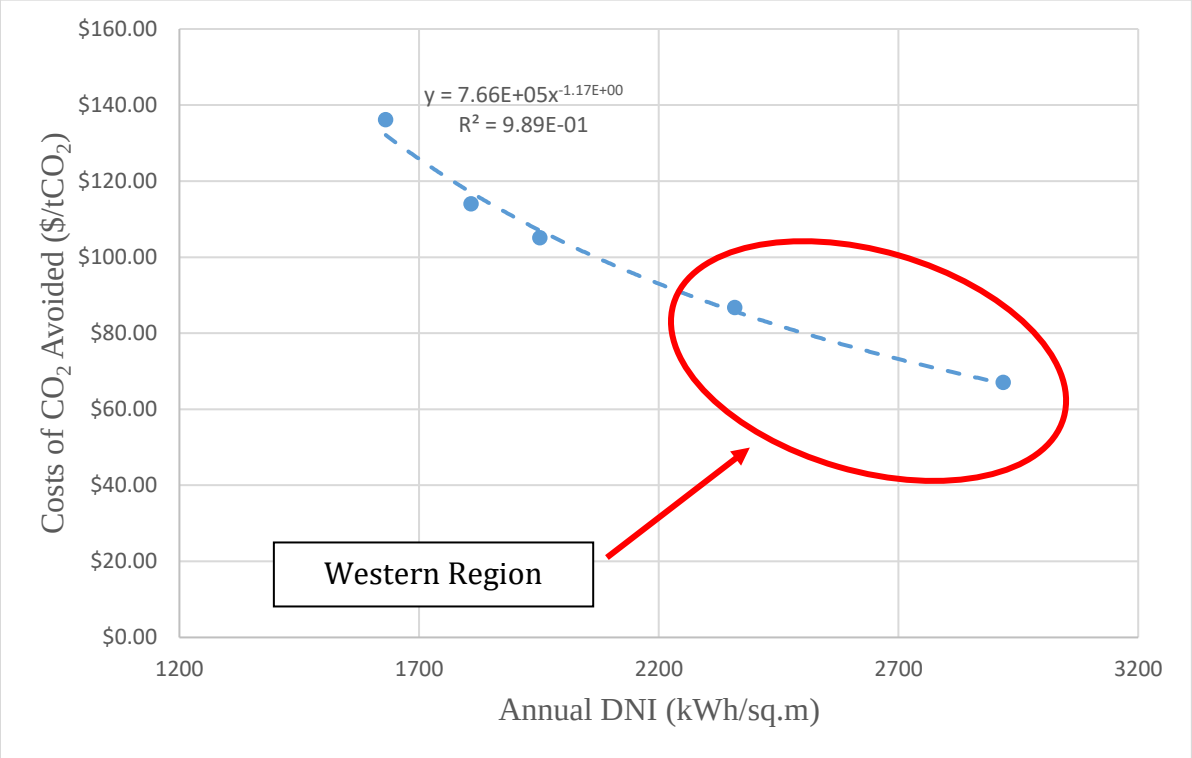

Figure 51: Costs of CO2 Avoided vs. Annual DNI

5 Summary, Conclusions, and Recommendations

5.1 Summary and Conclusions

In the first part of the study, a dynamic model of a solar integrated SOEC system is developed to evaluate its dynamic behavior and performance characteristics, aiming to achieve high hydrogen production efficiency and to minimize the BoP power consumption. The results show that the electrical efficiency of the integrated system is greater than 90% throughout the majority of the operating time. Particularly, the electrical efficiency between 10 AM and 1 PM is nearly 100%. During this period, the stack operates slightly endothermically with the stack efficiency higher than 100%. Such high efficiencies are achieved as a result of the stack operating in endothermic condition while taking thermal energy provided by the CSP plant. With the thermal control strategy used in the analysis, the stack temperature does not fluctuate, suggesting minimal system degradation during daily operation. PI controllers of the integrated system show thermal management success during the highly dynamic daily operation on solar energy.

In the second part of the study, a model of a CSP-integrated cement plant is developed to assess the performance characteristics and viability of such integration. The results show that the percent solarization and percent CO_2 emission reduction are only proportional to the DNI potential given the same capacity of thermal storage and solar calciner, and solar multiple. The SoCal plant can utilize solar thermal energy more than 70% of the operating time which is the maximum percent solarization among the other plants. The lowest solarization is achieved for the PA plant, only able to solarize 40% of the time. Based on the percent solarization, it is found that 15% of the CO_2 emissions can be

avoided once a coal-fired cement plant is integrated with a CSP plant for the SoCal plant. However, much less is avoided for the PA plant due to lower solarization rate, only able to avoid 9% of the total carbon emissions. Economically, the western region of the United States especially the state of California, Arizona, Nevada, and New Mexico is found to be the best region for integrating a conventional cement plant with a CSP plant where the annual DNI exceeds 2000 kWh/m^2. The costs of CO_2 avoided in the region range from 70 to 100 USD per ton of CO_2 which makes such integration as competitive as integration with other carbon capture technologies.

5.2 Recommendations

Future work should include the following:

- Integration of thermal energy storage in CSP-integrated SOEC system
- Dynamics of the SOEC integrated system for a typical week/month.
- Integration of steam turbine to the integrated SOEC system to operate during a high-demand period.
- Develop a control strategy for shutdown, restart, and idle mode for SOEC system operation.

References

[1] M. Francis, “EIA updates its U.S. energy consumption by source and sector chart,” 2019. [Online]. Available: https://www.eia.gov/todayinenergy/detail.php?id=41093.

[2] “Inventory of U.S. Greenhouse Gas Emissions and Sinks,” *United States Environmental Protection Agency*, 2017. [Online]. Available: https://www.epa.gov/ghgemissions/inventory-us-greenhouse-gas-emissions-and-sinks.

[3] J. Brouwer, “On the role of fuel cells and hydrogen in a more sustainable and renewable energy future,” *Curr. Appl. Phys.*, vol. 10, no. 2 SUPPL., pp. S9–S17, 2010.

[4] S. O. F. California and E. L. Material, “Senate Bill No. 100,” no. 100, 2018.

[5] P. Colbertaldo, S. B. Agustin, S. Campanari, and J. Brouwer, “Impact of hydrogen energy storage on California electric power system: Towards 100% renewable electricity,” *Int. J. Hydrogen Energy*, vol. 44, no. 19, pp. 9558–9576, 2019.

[6] A. Blakers, B. Lu, and M. Stocks, “100% renewable electricity in Australia,” *Energy*, 2017.

[7] D. Azhgaliyeva, “Energy storage and renewable energy deployment: Empirical Evidence from OECD countries,” in *Energy Procedia*, 2019.

[8] California Energy Commission, “California Energy Commission – Tracking Progress Energy: Energy Equity Indicators,” no. December 2018, pp. 1–22, 2018.

[9] A. Hormaza-Mejia, L. Zhao, and J. Brouwer, “SOFC MICRO-CHP SYSTEM WITH THERMAL ENERGY STORAGE IN RESIDENTIAL APPLICATIONS,” in *Proceedings of the ASME 2017 15th International Conference on Fuel Cell Science, Engineering and Technology*, 2017.

[10] “California Independent System Operator Grid Status.” [Online]. Available: http://www.caiso.com/TodaysOutlook/Pages/supply.aspx.

[11] “Managing Oversupply.” [Online]. Available: http://www.caiso.com/informed/Pages/ManagingOversupply.aspx.

[12] “Impacts of renewable energy on grid operations.” [Online]. Available: https://www.caiso.com/Documents/CurtailmentFastFacts.pdf.

[13] J. P. Maton, L. Zhao, and J. Brouwer, “Dynamic modeling of compressed gas energy storage to complement renewable wind power intermittency,” *Int. J. Hydrogen Energy*, vol. 38, no. 19, pp. 7867–7880, 2013.

[14] “What the duck curve tells us about managing a green grid,” *California Independent System Operator*, 2016. [Online]. Available: http://www.caiso.com/Documents/FlexibleResourcesHelpRenewables_FastFacts.pdf.

[15] "Managing Oversupply," *California Independent System Operator*, 2021. [Online]. Available: http://www.caiso.com/informed/Pages/ManagingOversupply.aspx.

[16] A. Schreider and R. Bucher, "An auspicious combination: Fast-ramping battery energy storage and high-capacity pumped hydro," *Energy Procedia*, vol. 155, pp. 156–164, 2018.

[17] "Hydrogen production: Natural gas reforming," *Office of Energy Efficiency & Renewable Energy*. [Online]. Available: https://www.energy.gov/eere/fuelcells/hydrogen-production-natural-gas-reforming.

[18] M. Schiller, "Hydrogen Energy Storage: A New Solution To the Renewable Energy Intermittency Problem," 2017. [Online]. Available: https://www.renewableenergyworld.com/2014/07/16/hydrogen-energy-storage-a-new-solution-to-the-renewable-energy-intermittency-problem/#gref.

[19] I. Pecenati, "Modeling and Simulation of High Temperature Electrolysis Coupled with Concentrated Solar Power for Hydrogen Production," Politecnico Di Milano, 2018.

[20] G. Schiller *et al.*, "Solar heat integrated solid oxide steam electrolysis for highly efficient hydrogen production," *J. Power Sources*, vol. 416, pp. 72–78, Mar. 2019.

[21] J. Sanz-Bermejo, V. Gallardo-Natividad, J. González-Aguilar, and M. Romero, "Coupling of a solid-oxide cell unit and a linear fresnel reflector field for grid management," in *Energy Procedia*, 2014, vol. 57, pp. 706–715.

[22] A. Ursúa, L. M. Gandía, and P. Sanchis, "Hydrogen production from water electrolysis: Current status and future trends," in *Proceedings of the IEEE*, 2012, vol. 100, no. 2, pp. 410–426.

[23] M. Lin and S. Haussener, "Techno-economic modeling and optimization of solar-driven high-temperature electrolysis systems," *Sol. Energy*, vol. 155, pp. 1389–1402, 2017.

[24] R. Boudries, "Techno-economic study of hydrogen production using CSP technology," *Int. J. Hydrogen Energy*, vol. 43, no. 6, pp. 3406–3417, Feb. 2018.

[25] M. Seitz, H. Von Storch, A. Nechache, and D. Bauer, "Techno economic design of a solid oxide electrolysis system with solar thermal steam supply and thermal energy storage for the generation of renewable hydrogen," *Int. J. Hydrogen Energy*, vol. 42, no. 42, pp. 26192–26202, 2017.

[26] N. Monnerie, H. Von Storch, A. Houaijia, M. Roeb, and C. Sattler, "Hydrogen production by coupling pressurized high temperature electrolyser with solar tower technology," *Int. J. Hydrogen Energy*, vol. 42, no. 19, pp. 13498–13509, 2016.

[27] M. Romero and A. Steinfeld, "Concentrating solar thermal power and thermochemical fuels," *Energy& Environ. Sci.*, vol. 5, no. 11, pp. 9137–9674, 2012.

[28] L. Mastropasqua, I. Pecenati, A. Giostri, and S. Campanari, "Solar hydrogen

production: Techno-economic analysis of a parabolic dish-supported high-temperature electrolysis system," *Appl. Energy*, vol. 261, p. 114392, Mar. 2020.

[29] A. Houaijia, M. Roeb, N. Monnerie, and C. Sattler, "Solar power tower as heat and electricity source for a solid oxide electrolyzer: A case study," *Int. J. Energy Res.*, vol. 39, no. 8, pp. 1120–1130, Jun. 2015.

[30] T. Ohta, N. Kamiya, M. Yamaguchi, N. Gotoh, T. Otagawa, and S. Asakura, "System efficiency of a water-splitting system synthesized by photochemical and thermoelectric conversion of solar energy," *Int. J. Hydrogen Energy*, vol. 3, no. 2, pp. 203–208, 1978.

[31] W. Dönitz, G. Dietrich, E. Erdle, and R. Streicher, "Electrochemical high temperature technology for hydrogen production or direct electricity generation," *Int. J. Hydrogen Energy*, vol. 13, no. 5, pp. 283–287, 1988.

[32] A. A. Alzahrani and I. Dincer, "Design and analysis of a solar tower based integrated system using high temperature electrolyzer for hydrogen production," *Int. J. Hydrogen Energy*, vol. 41, no. 19, pp. 8042–8056, 2016.

[33] A. Saeedmanesh, P. Colombo, and J. Brouwer, "Dynamic Behavior of a Solid Oxide Steam Electrolyzer System Using Transient Photovoltaic Generated Power for Renewable Hydrogen Production," in *International Mechanical Engineering Congress and Exposition*, 2018, pp. 1–12.

[34] A. Saeedmanesh and J. Brouwer, "Dynamic Modeling of a Solid Oxide Electrolyzer System under Two Different Thermal Control Strategies," in *13th European SOFC & SOE Forum*, 2018.

[35] California Energy Commission, "California Energy Commission-Tracking Progress," 2018.

[36] R. M. Andrew, "Global CO2 emissions from cement production, 1928-2018," *Earth System Science Data*, vol. 11, no. 4. 2019.

[37] A. Hasanbeigi and C. Springer, "Deep Decarbonization Roadmap for the Cement and Concrete Industries in California," 2019.

[38] H. Mikulčić, J. J. Klemeš, M. Vujanović, K. Urbaniec, and N. Duić, "Reducing greenhouse gasses emissions by fostering the deployment of alternative raw materials and energy sources in the cleaner cement manufacturing process," *J. Clean. Prod.*, vol. 136, 2016.

[39] J. Olivier, J. Peters, and G. Janssens-Maenhout, "Trends in global co2 emissions 2013 report," *BASIC Expert. 2011 Equitable access to Sustain. Dev. Contrib. to body Sci. Knowl.*, 2011.

[40] E. Worrell, L. Price, N. Martin, C. Hendriks, and L. O. Meida, "Carbon dioxide emissions from the global cement industry," *Annu. Rev. Energy Environ.*, vol. 26, 2001.

[41] The White House, "Executive Order on Climate-Related Financial Risk," 2021. .

[42] California Nevada Cement Association, "Achieving Carbon Neutrality in the California Cement Industry Key Barriers & Policy Solutions," 2021.

[43] A. C. (Thanos) Bourtsalas, J. Zhang, M. J. Castaldi, and N. J. Themelis, "Use of non-recycled plastics and paper as alternative fuel in cement production," *J. Clean. Prod.*, vol. 181, 2018.

[44] M. Georgiopoulou and G. Lyberatos, "Life cycle assessment of the use of alternative fuels in cement kilns: A case study," *J. Environ. Manage.*, vol. 216, 2018.

[45] J. Li, P. Tharakan, D. Macdonald, and X. Liang, "Technological, economic and financial prospects of carbon dioxide capture in the cement industry," *Energy Policy*, vol. 61, 2013.

[46] T. Hills, N. Florin, and P. S. Fennell, "Decarbonising the cement sector: A bottom-up model for optimising carbon capture application in the UK," *J. Clean. Prod.*, vol. 139, 2016.

[47] C. C. Cormos, A. M. Cormos, and L. Petrescu, "Assessing the CO2 Emissions Reduction from Cement Industry by Carbon Capture Technologies: Conceptual Design, Process Integration and Techno-economic and Environmental Analysis," in *Computer Aided Chemical Engineering*, vol. 40, 2017.

[48] M. Garcia and N. Berghout, "Toward a common method of cost-review for carbon capture technologies in the industrial sector: cement and iron and steel plants," *Int. J. Greenh. Gas Control*, vol. 87, 2019.

[49] A. Meier, N. Gremaud, and A. Steinfeld, "Economic evaluation of the industrial solar production of lime," *Energy Convers. Manag.*, vol. 46, no. 6, 2005.

[50] C. Tregambi *et al.*, "Solar-driven production of lime for ordinary Portland cement formulation," *Sol. Energy*, vol. 173, 2018.

[51] G. Moumin *et al.*, "CO2 emission reduction in the cement industry by using a solar calciner," *Renew. Energy*, vol. 145, 2020.

[52] R. S. González and G. Flamant, "Technical and economic feasibility analysis of using concentrated solar thermal technology in the cement production process: Hybrid approach-a case study," *J. Sol. Energy Eng. Trans. ASME*, vol. 136, no. 2, 2014.

[53] M. Tomatis, H. K. Jeswani, L. Stamford, and A. Azapagic, "Assessing the environmental sustainability of an emerging energy technology: Solar thermal calcination for cement production," *Sci. Total Environ.*, vol. 742, 2020.

[54] S. O. Gardarsdottir *et al.*, "Comparison of technologies for CO 2 capture from cement production—Part 2: Cost analysis," *Energies*, vol. 12, no. 3, 2019.

[55] M. Voldsund *et al.*, "Comparison of Technologies for CO 2 Capture from Cement Production-Part 1: Technical Evaluation," vol. 12, p. 559, 2019.

[56] A. Saeedmanesh, P. Colombo, D. Mclarty, and J. Brouwer, "Dynamic Behavior of a

Solid Oxide Steam Electrolyzer System Using Transient Photovoltaic Generated Power for Renewable Hydrogen Production," *J. Electrochem. Energy Convers. Storage*, vol. 16, no. 4, Nov. 2019.

[57] "System Advisor Model Version 2018.11.11 (SAM 2018.11.11 r4). National Renewable Energy Laboratory. Golden, CO. Accessed Oct 1, 2019." .

[58] X. Xu *et al.*, "Experimental Test of Properties of KCl-MgCl2 Eutectic Molten Salt for Heat Transfer and Thermal Storage Fluid in Concentrated Solar Power Systems," *J. Sol. Energy Eng. Trans. ASME*, vol. 140, no. 5, Oct. 2018.

[59] M. Wagner, "Simulation and Predictive Performance Modeling of Utility-Scale Central Receiver System Power Plants," University of Wisconsin – Madison, 2008.

[60] T. L. Bergman, A. S. Lavine, F. P. Incropera, and D. P. Dewitt, *Fundamentals of Heat and Mass Transfer. 7th Edition*. 2011.

[61] F. Schorcht, I. Kourti, B. M. Scalet, S. Roudier, and L. D. Sancho, *Best Available Techniques (BAT) Reference Document for the Production of Cement, Lime and Magnesium Oxide*. 2013.

[62] R. Anantharaman *et al.*, "CEMCAP framework for comparative techno- economic analysis of CO2 capture from cement plants. Deliverable D3.2 of the HORIZON 2020 project CEMCAP. EC Grant agreement no: 641185," 2015.

[63] R. Anantharaman, C. Fu, S. Roussanaly, and M. Voldsund, "Design and performance of CEMCAP cement plant with MEA post combustion capture. Deliverable D4.2 of the HORIZON 2020 project CEMCAP. EC Grant agreement no: 641185," 2016.

[64] D. STRANIERO, "REGENERATIVE SOLID OXIDE CELLS (RSOCs) FOR ENERGY STORAGE APPLICATIONS," POLITECNICO DI MILANO, 2017.

[65] UNIFRAX, "Product Information Sheet Excelfrax Microporous Insulation," 2018.

[66] "Coal prices and outlook," *U.S. Energy Information Administration*, 2019. [Online]. Available: https://www.eia.gov/energyexplained/coal/prices-and-outlook.php#:~:text=In 2019%2C the national average,was %2438.53 per short ton.

[67] "NSRDB Data Viewer." [Online]. Available: https://maps.nrel.gov/nsrdb-viewer/.

Appendices

Appendix A: Thermal Storage Operating Profiles for NorCal, TX, and AL Plants

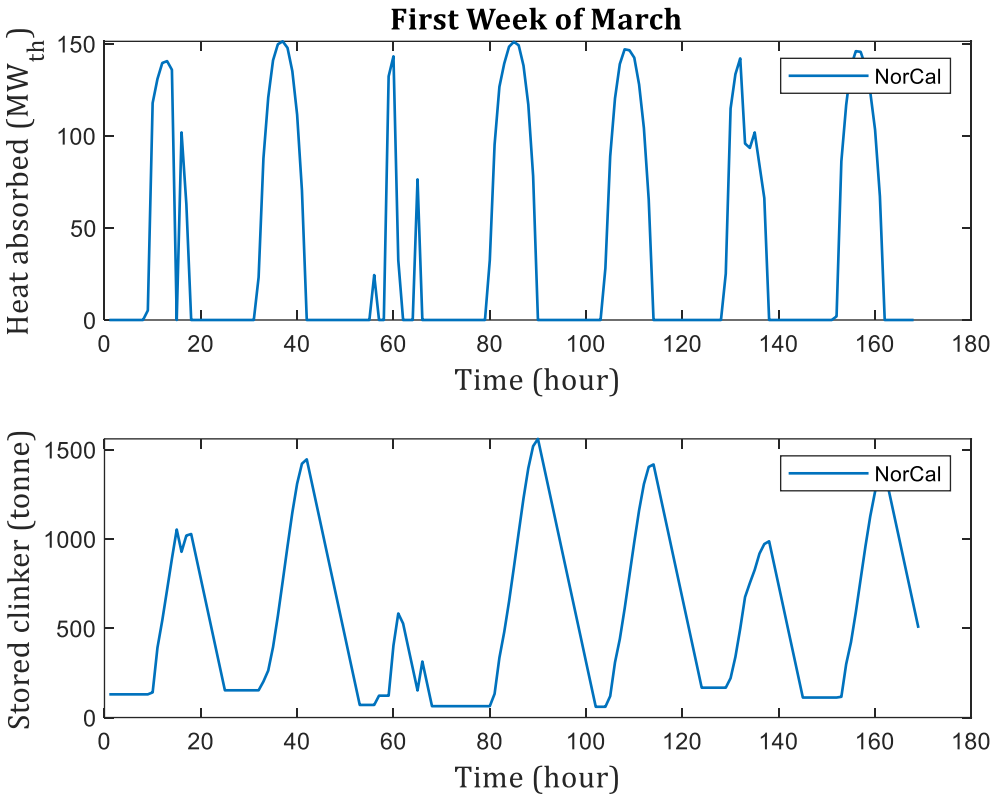

Figure 52: Thermal Operating Profiles for NorCal Plant in March

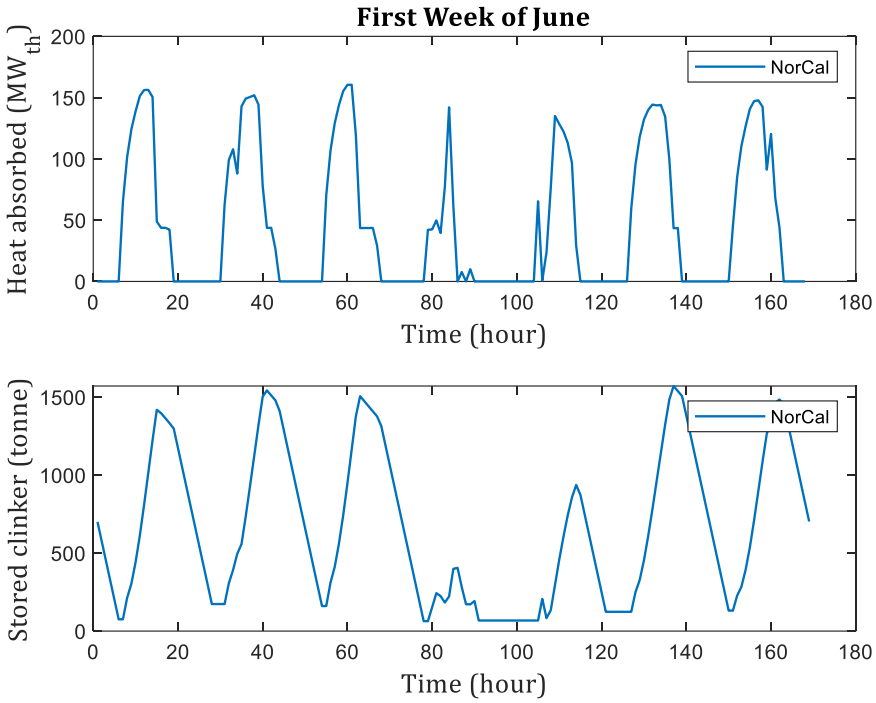

Figure 53: Thermal Operating Profiles for NorCal Plant in June

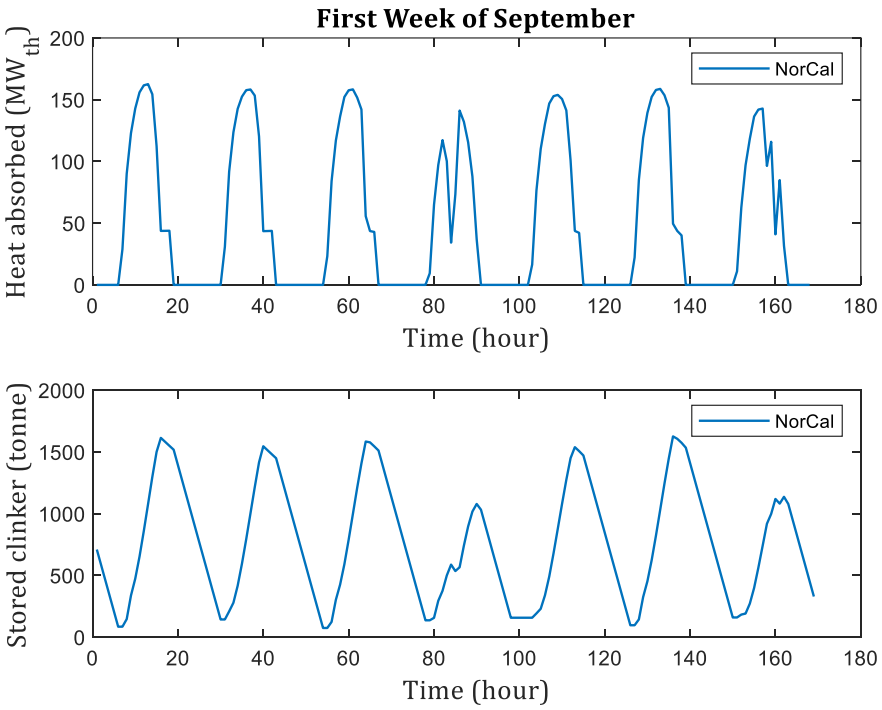

Figure 54: Thermal Operating Profiles for NorCal Plant in September

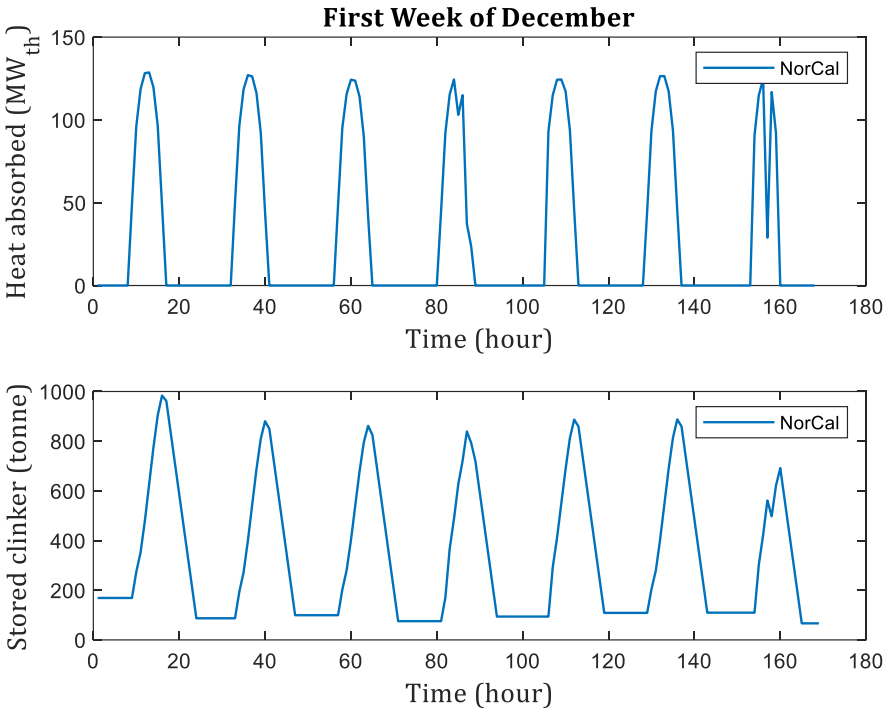

Figure 55:Thermal Operating Profiles for NorCal Plant in December

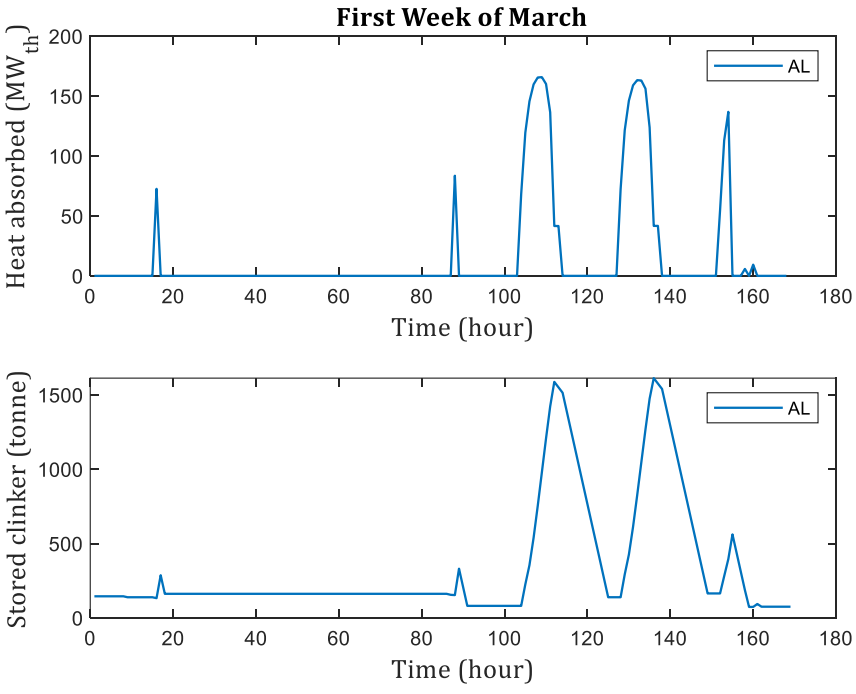

Figure 56: Thermal Operating Profiles for AL Plant in March

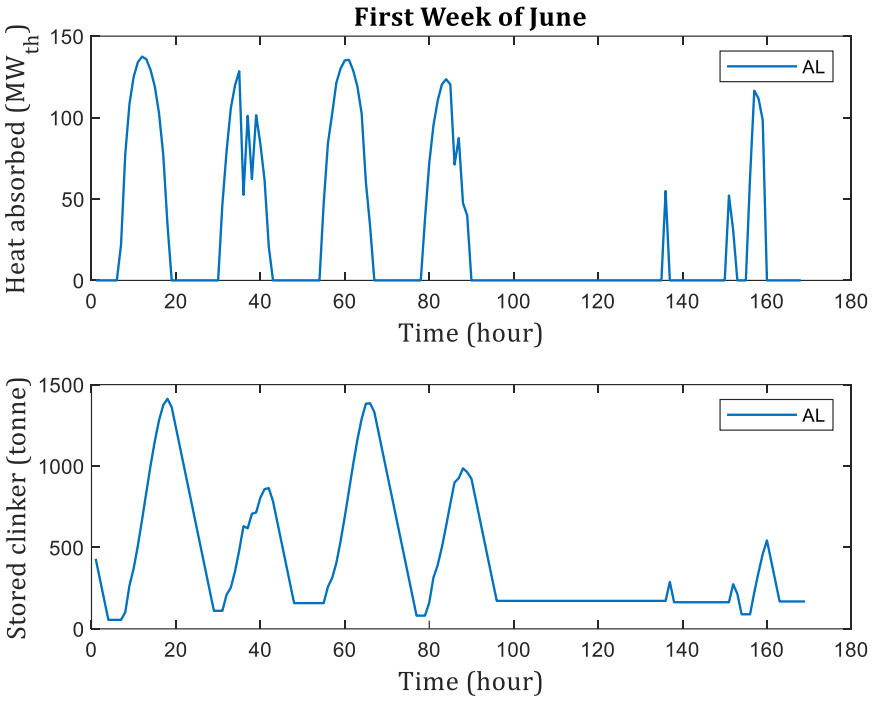

Figure 57: Thermal Operating Profiles for AL Plant in June

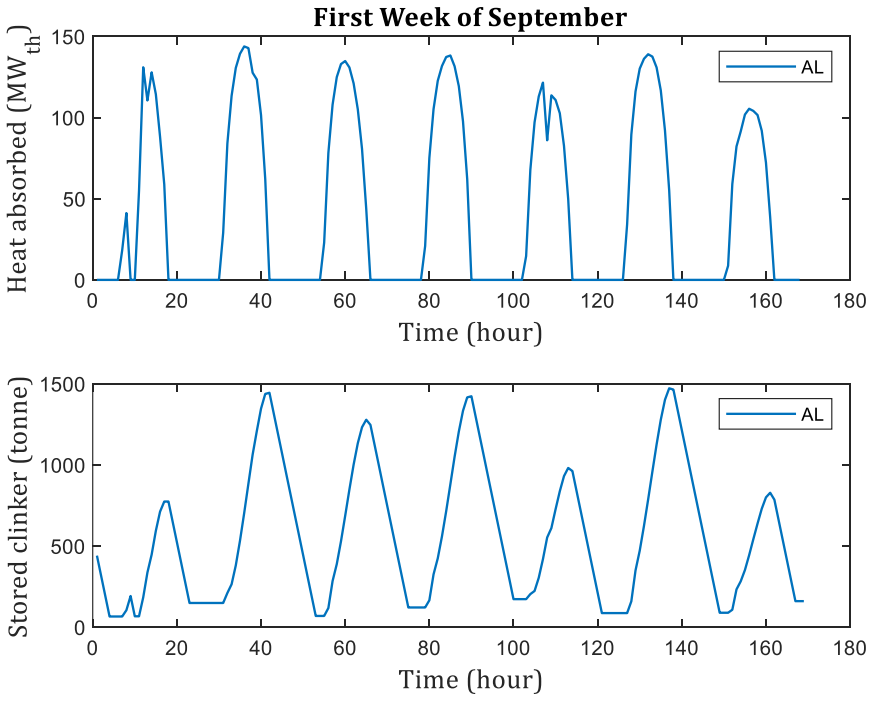

Figure 58: Thermal Operating Profiles for AL Plant in September

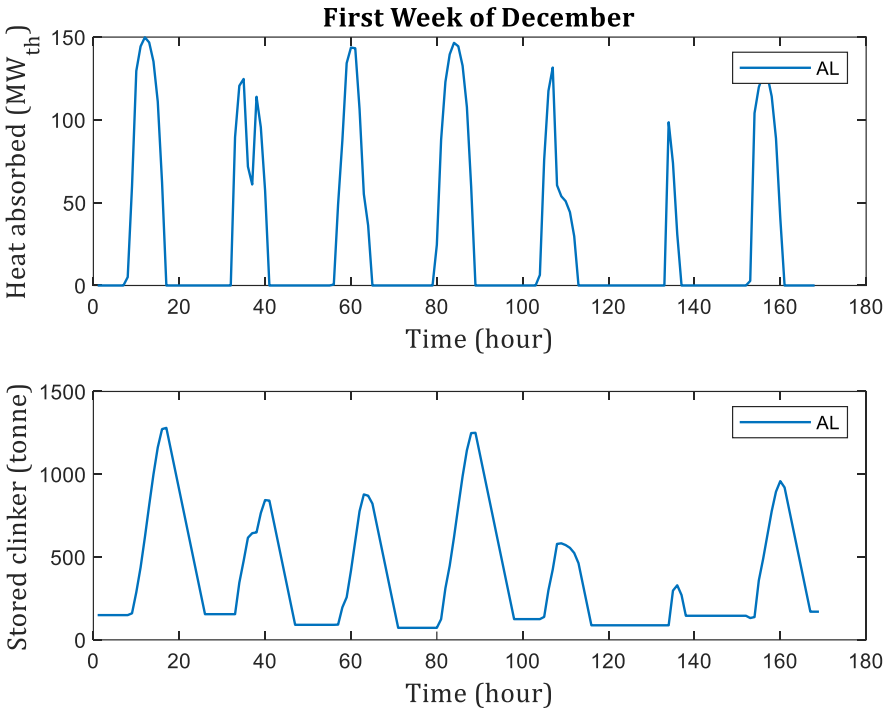

Figure 59: Thermal Operating Profiles for AL Plant in December

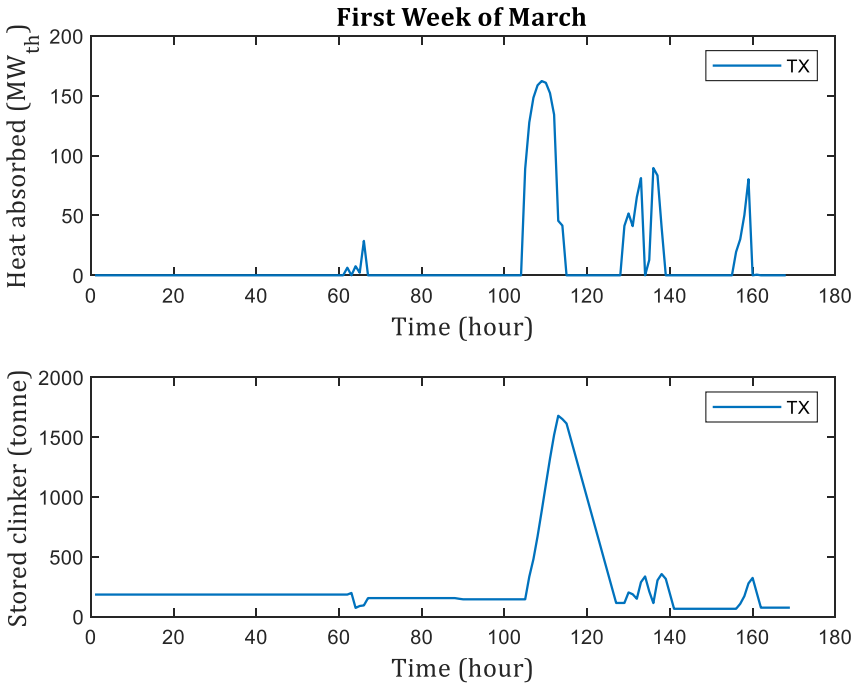

Figure 60: Thermal Operating Profiles for TX Plant in March

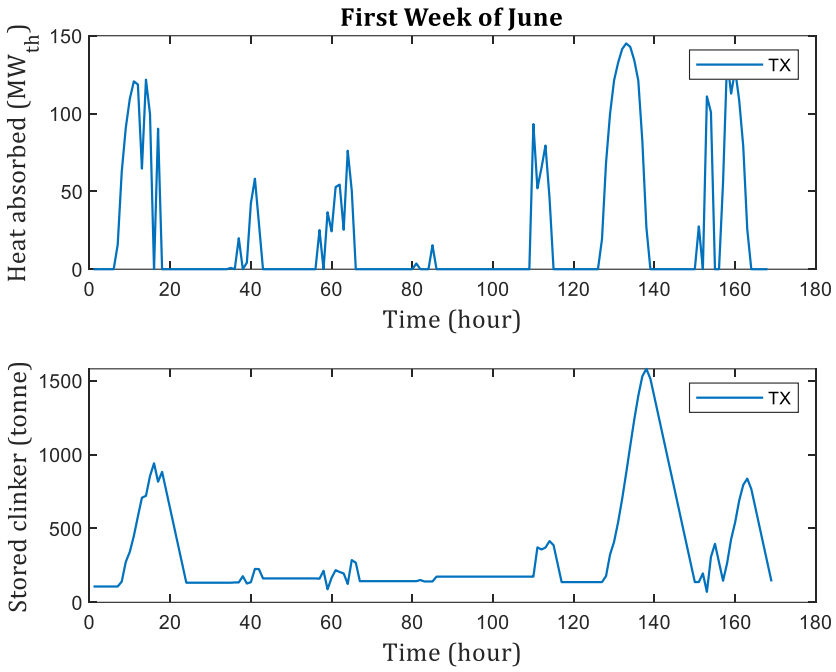

Figure 61: Thermal Operating Profiles for TX Plant in June

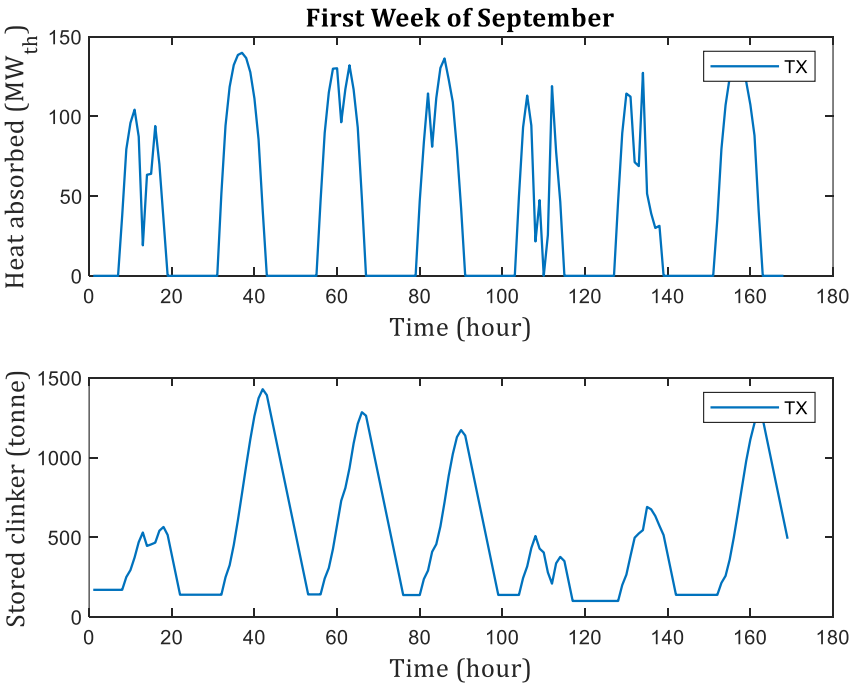

Figure 62: Thermal Operating Profiles for TX Plant in September

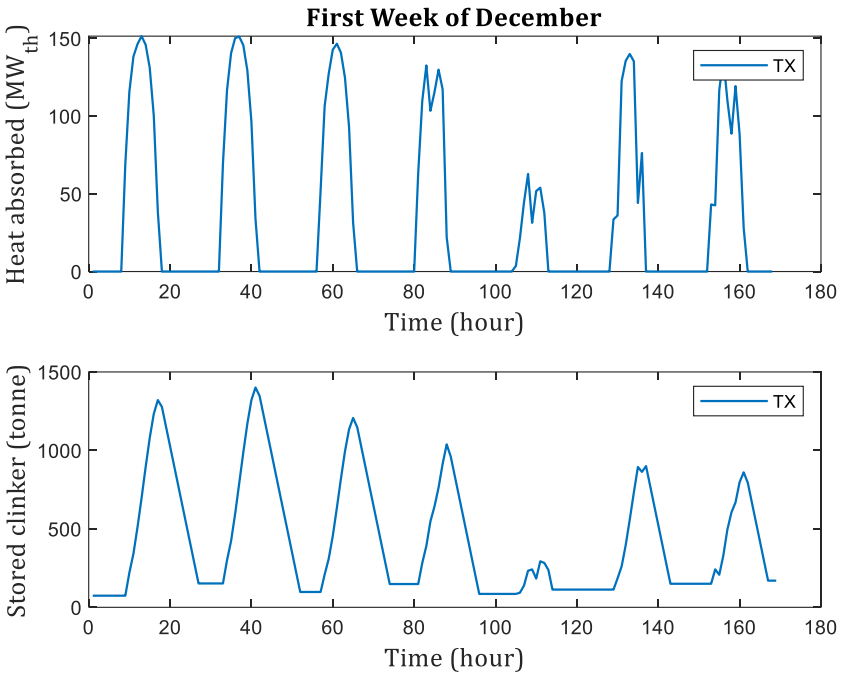

Figure 63: Thermal Operating Profiles for TX Plant in December

Appendix B: Relevant Annual Profiles for SoCal and NorCal Plants

SoCal Plant

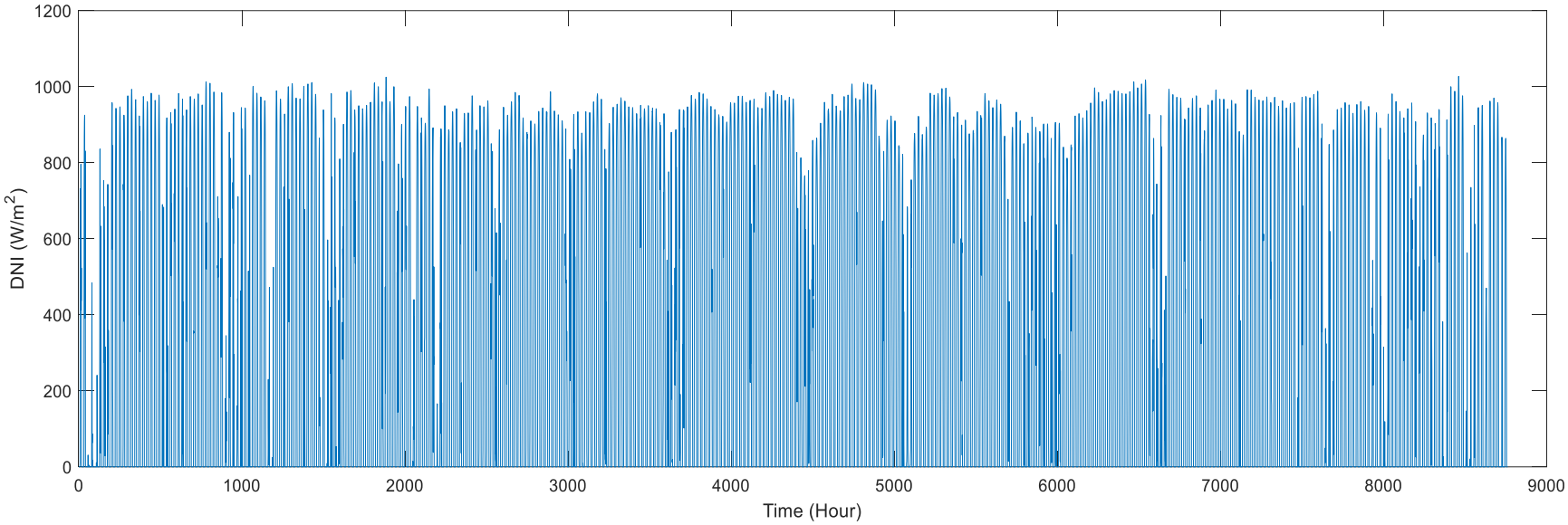

Figure 64: SoCal Plant Annual DNI Profile

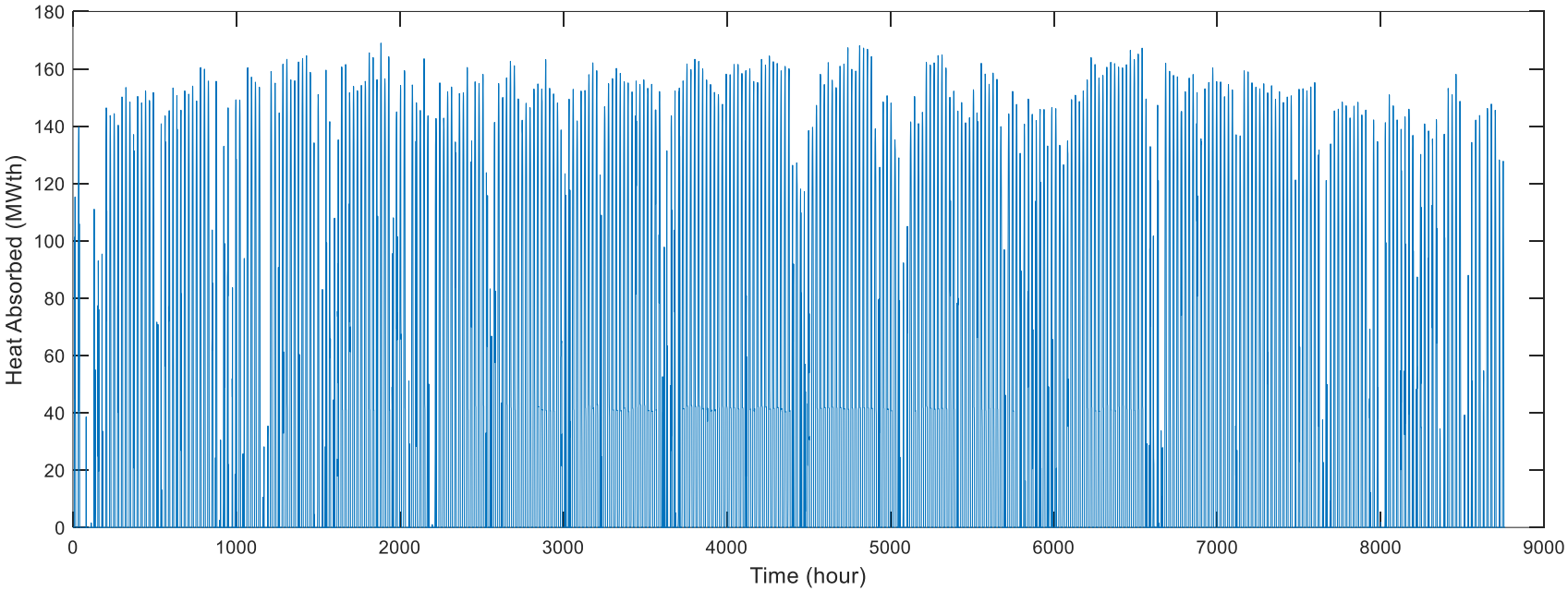

Figure 65:SoCal Plant Solar Calciner Dynamics for a Complete Annual Simulation

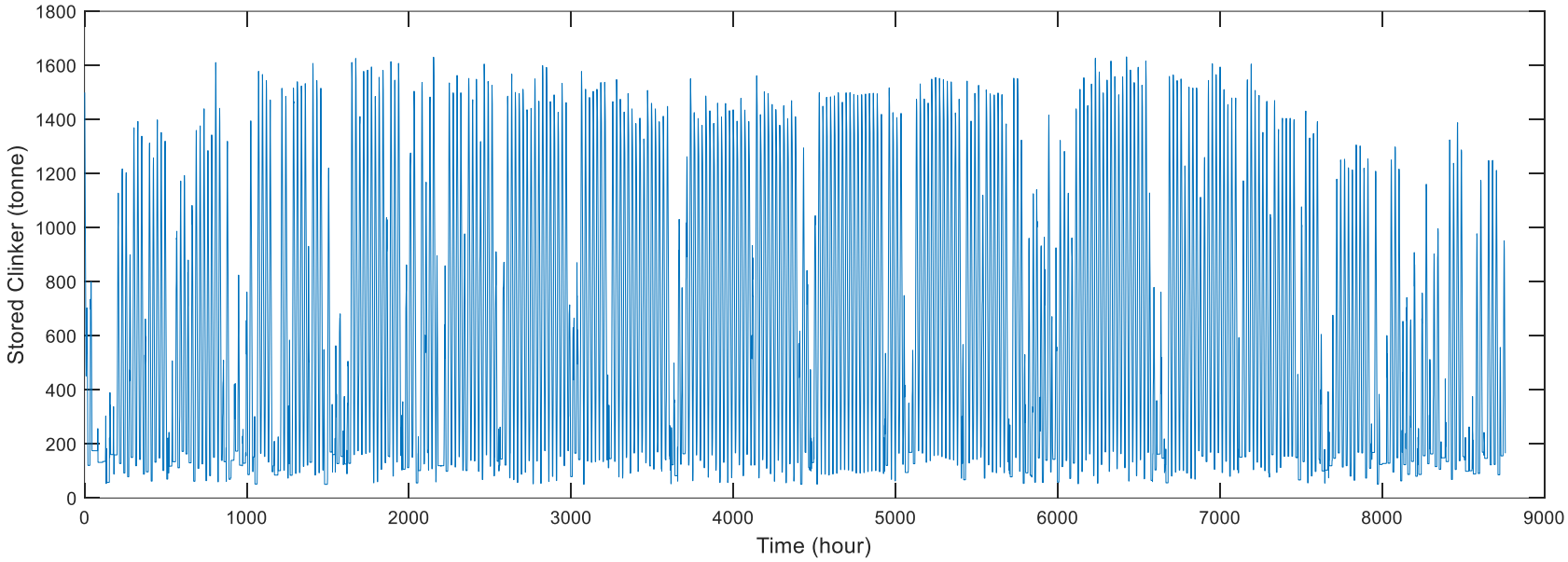

Figure 66: SoCal Plant Storage Mass Dynamics for a Complete Annual Simulation

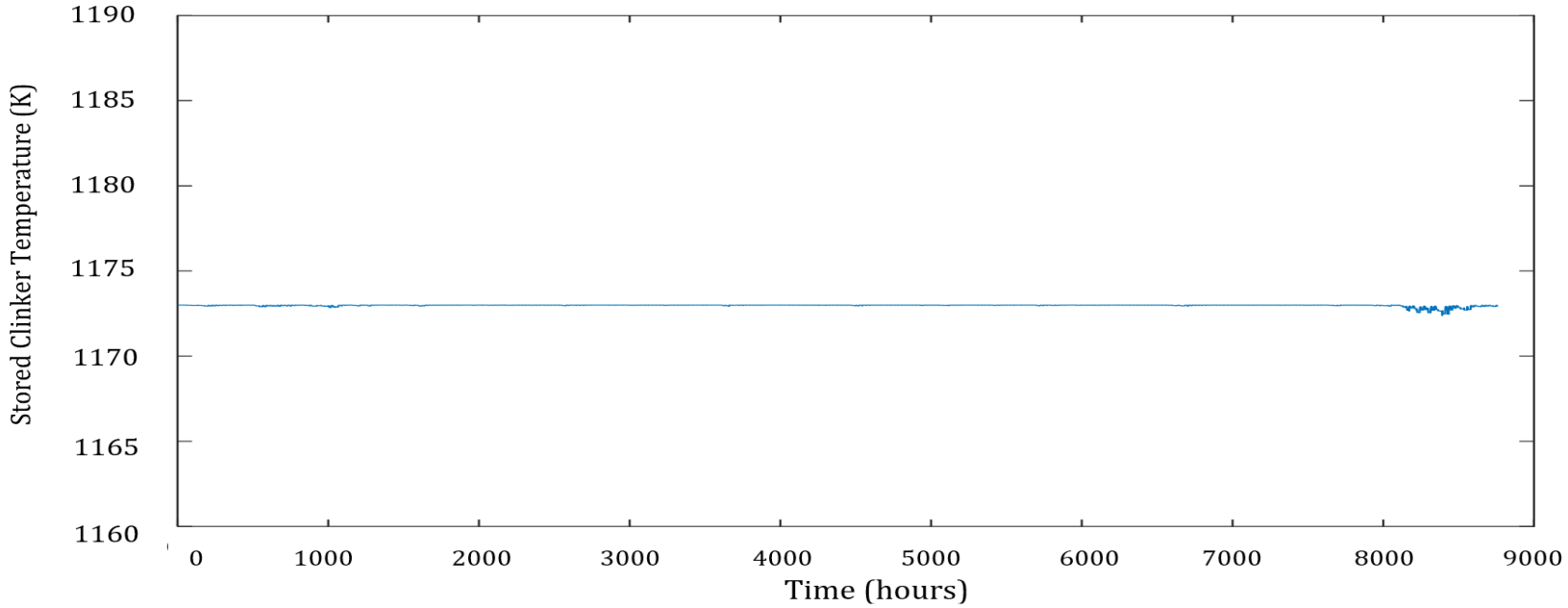

Figure 67: SoCal Plant Storage Temperature Dynamics for a Complete Annual Simulation

NorCal Plant

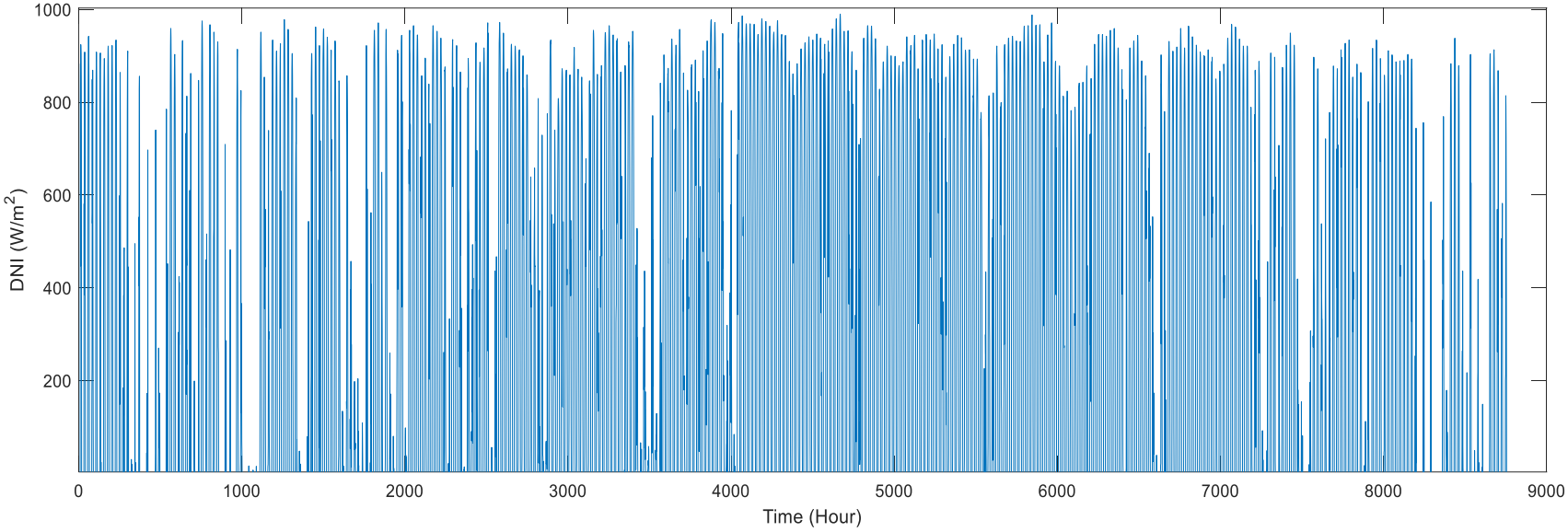

Figure 68: No*r*Cal Plant Annual DNI Profile

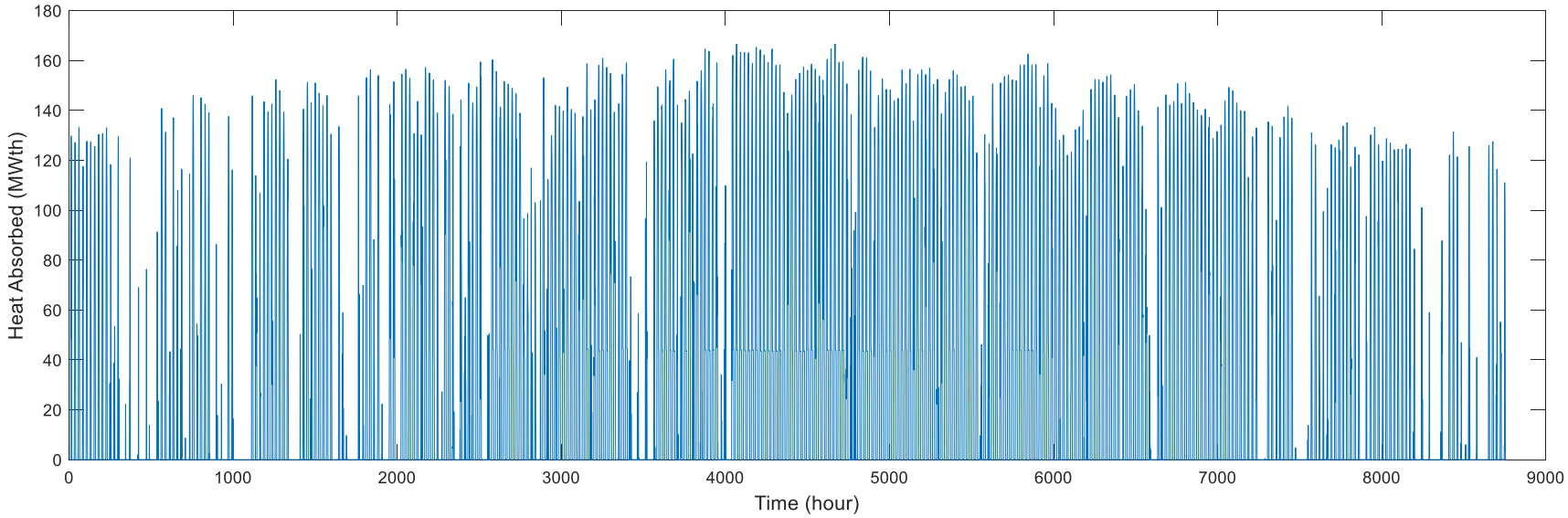

Figure 69: NorCal Plant Solar Calciner Dynamics for a Complete Annual Simulation

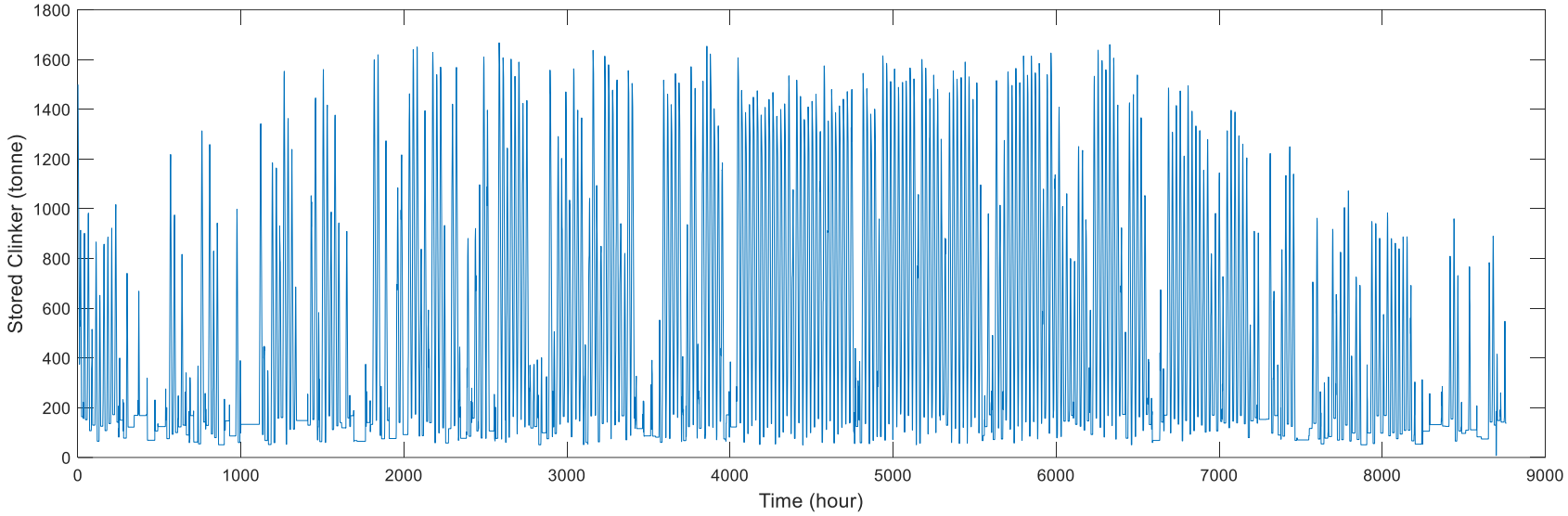

Figure 70: NorCal Plant Storage Mass Dynamics for a Complete Annual Simulation

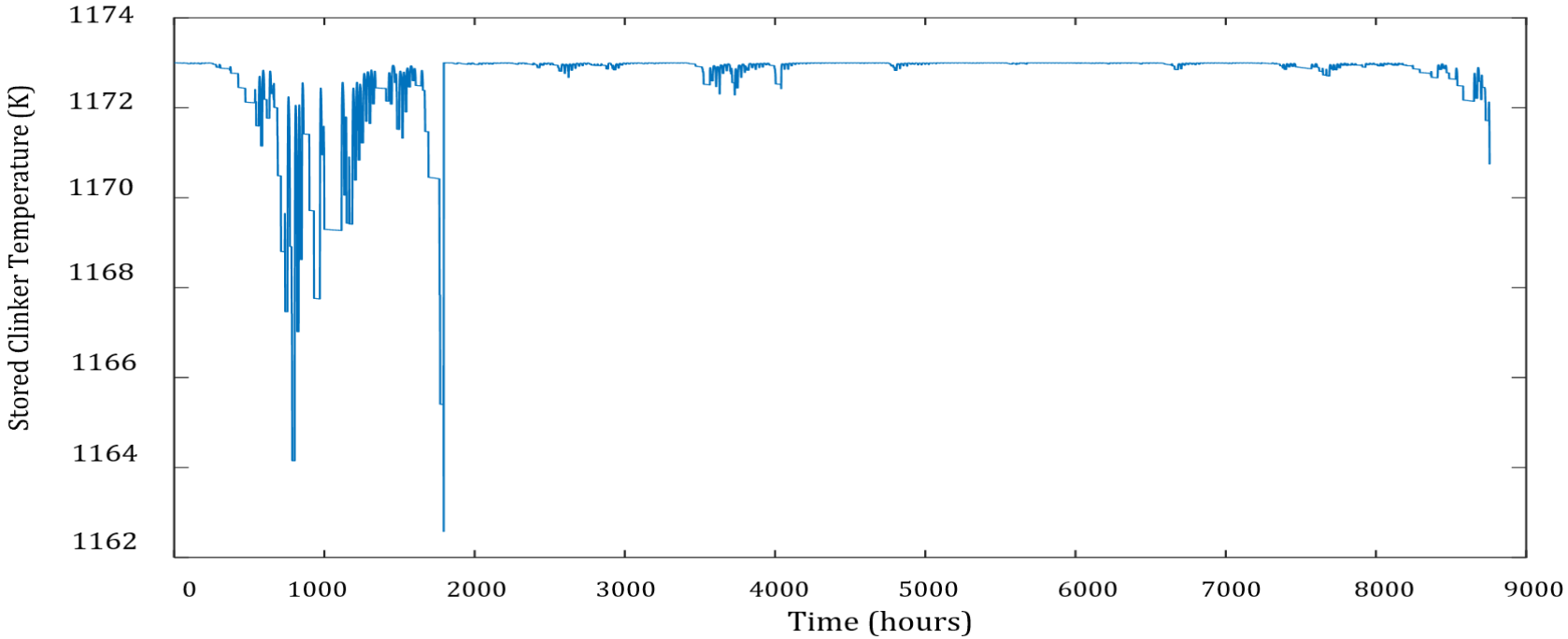

Figure 71: NorCal Plant Storage Temperature Dynamics for a Complete Annual Simulation